All-sky gravitational wave searches for isolated neutron stars: methods and applications to LIGO-Virgo data

Candidate

Martina Di Cesare

ID number 1697089

Thesis Advisor

Prof. Pia Astone

Co-Advisor

Dr. Ornella Juliana Piccinni

Academic Year 2020/2021

Thesis not yet defended

All-sky gravitational wave searches for isolated neutron stars: methods and applications to LIGO-Virgo data

Master's thesis. Sapienza – University of Rome

This thesis has been typeset by LaTeX and the Sapthesis class.

Author's email: dicesare.1697089@studenti.uniroma1.it

"Why should a man climb the Everest? Because it is there."
Everest - Public Service Broadcasting

"Do the scary things first and get scared later."
Lemony Snicket

Abstract

As first purpose of this thesis, a new sensitivity estimation method was developed in order to save computational power in future searches. This method was tested for O2 data thanks to a comparison with the Upper limit computed with software injection and then used on O3 in order to define new sensibility and Upper limit curves. Moreover, the Band Sample Data (BSD) framework was implemented in the Frequency Hough pipeline instead of the four-bands division database called SFDB which has fixed coherence time, i.e. T_{FFT} for each band. Thanks to the tunability of the T_{FFT} in BSD, there were provided proofs of the improvement of the candidates in the pipeline through the Critical ratio value, a random variable that measures the statistical significance of the of the candidate respect to its expected value in presence of the noise alone. This can be considered as a starting point to for an improved the sensibility of the LIGO-Virgo detectors.

Contents

Introduction

The *first* detection of gravitational waves (GWs) made by the two LIGOs on 14th September 2015 and recorded as GW150914[1] was a breakthrough in the astrophysical field. It proved that an Einstein's prediction was correct once again. There are other several reasons why a detection of GW is important: first, it is a new window of information transport from the one carried by electromagnetic waves; second, by comparing the arrival times of light and GW the Einstein's prediction about the speed of GW being equal of light speed can be checked[2]; finally, the detection gives information about the polarization of the GW signal (which are two for the General Relativity, but other theories state the existence of six different polarization [37]).

GW150914 was a coalescence of a binary system composed by two black holes (BH-BH) with very similar values of mass ($36^{+5}_{-4}M_\odot$ and $29^{+4}_{-4}M_\odot$, [1]), but there are plenty of other possible sources that the astrophysicists are looking to detect.

In Chapter 1 I will discuss about the GWs solution starting from *Einstein's field equations* - Section 1.1 - and different typologies of GWs generators - Section 1.2-, focusing on the periodic neutron star (NS) source in a particular research field called *All-sky* - Section 1.3.

Of course, to detect a signal it's fundamental the data analysis procedure. In the present work I used the hierarchical data analysis pipeline known as *Frequency Hough* (FH) that will be described in the first part of Chapter 2 while Section 2.2 is about the new framework *Band Sampled Data* (BSD).

Chapter 3 contains the first half of my work whose core is a new procedure that makes use of a parameter called *Critical ratio* (CR). This function will be applied to O2 data with the aim to prove the validity of the new sensitivity estimation method, and then to O3 data to compute and define the new Upper limit (UL) and sensitivity curves.

Chapter 4 is the second half of my thesis and it focuses on the implementation of the BSD database instead of the original four-bands splitting (SFDB) as initial step of the FH pipeline. This new algorithm will be used at first to make a comparison between Hough maps computed in different Doppler correction cases. Moreover, thanks to some hardware injections (HIs) and the flexibility of the BSD, I have been able to prove and provide the relation between T_{FFT} and CR for the two Doppler corrections. This has made possible to conclude that the lower is the pulsar

---

[1]This name has the following meaning: GW stands for **G**ravitational **W**ave, the numbers are the year/month/day of the event.

[2]Thanks to the event GW170817 - a coalescence of two neutron stars and the first multi-messenger detection - the resulting constrain on the fractional speed difference is $-3 \cdot 10^{-15} \leq \frac{\Delta\nu}{\nu_{EM}} \leq +7 \cdot 10^{-16}$ where $\Delta\nu = \nu_{GW} - \nu_{EM}$ as reported in [4].

frequency respect to the SFDB four intervals, the better CR improvement will be.

Chapter 1

Gravitational waves

Gravitation waves (GWs) were first postulated in 1916 by Albert Einstein and are one of the most interesting predictions of General Relativity (GR). Thanks to Russell Alan Hulse and Joseph Hooton Taylor they were *indirectly* observed in a binary system called *PSR B1913+16*[1] through its changing periastron period. In Fig. 1.1 are reported the GR prediction (solid curve) and the data acquired (black dots) by Arecibo, a radio telescope.
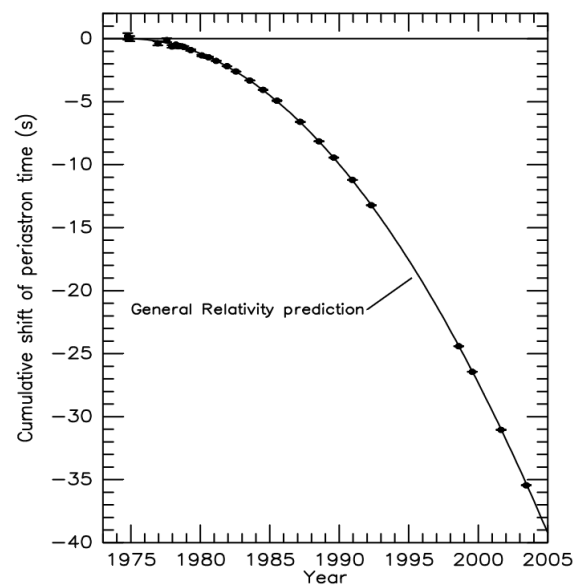
Figure 1.1. The horizontal axis represents the time (in years) while the vertical axis the variation of periastron (in seconds). The solid curve describes the period variation of the pulsar according to General Relativity prediction, the black dots are the data acquired during the years and the straight horizontal line is the zero periastron variation. This indirect observation was worth the Nobel Prize in 1993 for R. A. Hulse and J. H. Taylor [38].

---

[1]The system is composed by a pulsar (i.e. a rotating neutron star that emits strong and fast electromagnetic impulses) and a neutron star.

An (unsuccessful) attempt to measure GW *directly* was made by Joseph Weber in the mid-1960s with the so-called *Weber bars.* Weber designed these heavy metallic bars that were seismically isolated and to which a set of piezoelectric strain transducer were bounded in order to detect bar vibration if excited by a GW. The main problem was that these bars were not sensitive enough.

After the bars, gravitational wave detectors with laser beams were constructed and they can be summarized as a Michelson interferometer. These devices are L shaped[2] and several kilometers long. The source beam is divided by a Beam Splitter (BS), then at the end of each arm a mirror reflects the laser and the two beams are reunited in the BS, in the end the composed laser is analyzed. A GW passing will cause a variation of the length of the two arms: when one contracts, the other expands and viceversa producing a phase variation of the two laser beams. Of course, actual detectors such as LIGO (one in Livingston and the other in Hanford both in USA) and Virgo (Cascina, Italy) are far more complicated than this simple configuration because several practical issues have to be taken into account as is shown in Fig 1.2.
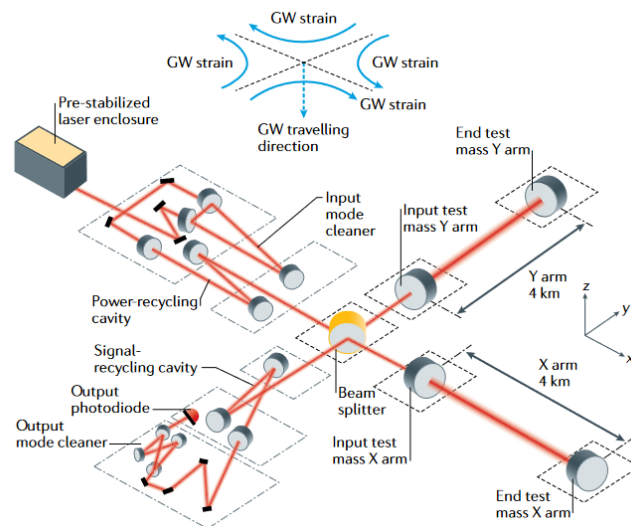
Figure 1.2. A representation of LIGO that shows the optical configuration and the additional elements with respect to Michelson's configuration [13].

After having briefly outlined the GW history, in this following first chapter I will discuss the mechanism that originates the metric perturbation of the spacetime, i.e. the gravitational waves, (1.1) along with a more detailed discussion of its different sources (1.2) and the variety of searches that are used to study the sky in order to find a GW signal (1.3).

---

[2]Different configurations are possible: the Einstein telescope, of the third generation detectors, is LISA - that will be the first space laser GW detector and that is planned to be triangle-shaped.

1.1   Generation mechanism of gravitational waves

General Relativity is currently the framework that can explain gravitational phenomena on macroscopic scales. It's a classical (i.e. non-quantum) theory of the gravitational field whose degree of freedom are described by the rank-2 metric tensor $g_{\mu\nu}$ which is symmetric, covariant and has ten independent components. GR reduces to Newton's formulation in the case of weak (gravitational) field and it includes a local stress-energy-momentum conservation ($T^{\mu\nu}{}_{,\nu} = 0$). In addition to all of that, GR has passed several test: gravitational lensing of the light, precession of Mercury perihelion and gravitational redshift.

According to Newton, the changes in gravitational field are *instantaneous* i.e. they propagate with infinite speed; this would cause a problem in the principle of causality because there isn't any information that can travel faster than light. In Einstein's theory the information propagates with *finite* speed and with the speed of light [20]. This traveling information about gravitational field changes is a gravitational wave. The equations of interest are the *Einstein's field equations* summarized as

$$R_{\mu\nu} - \frac{1}{2}g_{\mu\nu}R = \frac{8\pi G}{c^4}T_{\mu\nu} \tag{1.1}$$

or

$$G_{\mu\nu} = \frac{8\pi G}{c^4}T_{\mu\nu} \tag{1.2}$$

where

$$G_{\mu\nu} = R_{\mu\nu} - \frac{1}{2}g_{\mu\nu}R$$

is the *Einstein tensor*.

The elements of Eq. 1.1 are now going to be stress out one by one and from left to right. They are the Ricci tensor$R_{\mu\nu}$, the curvature scalar R and the stress-energy tensor $T_{\mu\nu}$.

To understand the left side of the equation, the affine connections - or *Christoffel symbols* - have to be introduced. Given a vector field $\vec{V} = V^\mu \vec{e}_{(\mu)}$, the derivative of the basis vector $\vec{e}_{(\mu)}$ (that takes the α index) is

$$\frac{\partial \vec{e}_{(\alpha)}}{\partial x^\beta} = \Gamma^\mu_{\alpha\beta}\vec{e}_{(\mu)}$$

where α indicates which basis vector we are differentiating while β indicates the coordinate with respect to which the differentiation is performed.

$\Gamma^\mu_{\alpha\beta}$ represents the Christoffel symbol that is the variation of the vectors due to the spacetime curvature. The explicit form is [3]

$$\Gamma^\sigma_{\alpha\beta} = \frac{1}{2}g^{\sigma\mu}(g_{\mu\alpha,\beta} + g_{\mu\beta,\alpha} - g_{\alpha\beta,\mu}) \tag{1.3}$$

$\boldsymbol{R_{\mu\nu}}$, **Ricci tensor**. The Ricci tensor is a contraction of the Riemann tensor $R_{\alpha\beta\mu\nu}$[4] i.e. $R_{\mu\nu} = g^{\alpha\beta}R_{\alpha\mu\beta\nu}$ which is linear in the second derivatives of $g_{\mu\nu}$ and non linear

---

[3]This is the result of some calculations performed in [16].

[4]$R_{\alpha\beta\mu\nu} = g_{\alpha\lambda}R^\lambda_{\beta\mu\nu}$. The Riemann tensor gives information about spacetime curvature: if $R^\lambda_{\beta\mu\nu} = 0$ in any reference frame $\rightarrow$ flat spacetime; if $R^\lambda_{\beta\mu\nu}$ has at least one component that is not null $\rightarrow$ curved spacetime. For this reason, Riemann tensor is also called *curvature tensor*. [16]

in the first derivatives; the dependence on the metric tensor can be pointed out by writing down the full Riemann's tensor form

$$R^\lambda_{\beta\mu\nu} = \frac{1}{2}g^{\alpha\sigma}(g_{\sigma\nu,\beta\mu} - g_{\sigma\mu,\beta\nu} + g_{\beta\mu,\sigma\nu} - g_{\beta\nu,\sigma\mu})$$

which clearly recalls the Eq 1.3, so rearranging the index it can be written as

$$R^\alpha_{\mu\beta\nu} = -(\Gamma^\alpha_{\mu\beta,\nu} - \Gamma^\alpha_{\mu\nu,\beta} + \Gamma^\alpha_{\nu\eta}\Gamma^\eta_{\mu\beta} - \Gamma^\alpha_{\beta\eta}\Gamma^\eta_{\mu\nu})$$

R, Curvature scalar. The curvature scalar R is a contraction of Ricci tensor $R_{\mu\nu}$, i.e. $R = g^{\mu\nu}R_{\mu\nu}$. The curvature scalar is a real number that express the amount by which the volume of a small geodesic ball in a Riemannian manifold deviates from that of the standard ball in Euclidean space. It has a similar role of Gaussian curvature (K) that is used to express the curvature of a two-dimensional surface (in 2D space $R = 2K$).

$T_{\mu\nu}$, Stress-energy tensor. Given a system of n non-interacting particles located at some points $\xi_n(t)$, each with energy-momentum $p_n^\alpha = (p_n^0, p_n^i)$ (where $p^0 = mc\gamma = \frac{E}{c}$ is the time-component and $p^i = m\gamma v^i$ are the space-components), the stress-energy tensor is defined as

$$T^{\alpha\beta} = c^2\sum_n p_n^\alpha \frac{d\xi_n^\beta}{dt}\delta^3(\boldsymbol{\xi} - \boldsymbol{\xi}_n(t)) \tag{1.4}$$

where the **bold** represents a three-dimensional vector like $\boldsymbol{a} = (a_1, a_2, a_3)$. This form summarizes the three quantities

- **Density of energy** ($\alpha = 0$, $\beta = 0$)

$$T^{00} \equiv \sum_n cp_n^0(t)\delta^3(\boldsymbol{\xi} - \boldsymbol{\xi}_n(t)) = \sum_n E_n\delta^3(\boldsymbol{\xi} - \boldsymbol{\xi}_n(t))$$

- **Density of momentum** ($\alpha = 0$, $\beta = i$)

$$T^{0i} \equiv \sum_n cp_n^i(t)\delta^3(\boldsymbol{\xi} - \boldsymbol{\xi}_n(t))$$

- **Current of momentum** ($\alpha = k$, $\beta = i$)

$$T^{ki} \equiv \sum_n p_n^k(t)\frac{d\xi_n^i}{dt}\delta^3(\boldsymbol{\xi} - \boldsymbol{\xi}_n(t))$$

An alternative way of writing Eq 1.4 is

$$T^{\alpha\beta} = c\sum_n \int p_n^\alpha \frac{d\xi_n^\beta}{d\tau_n}\delta^4(\vec{\xi} - \vec{\xi}_n(\tau_n))d\tau_n \tag{1.5}$$

where the $\rightarrow$ stands for a four-dimensional vector like $\vec{v} = (v_0, v_1, v_2, v_3)$. This brings to the generic expression[5]

$$T^{\alpha\beta} = c\sum_n \int \frac{1}{\sqrt{-g}}p_n^\alpha \frac{dx_n^\beta}{d\tau_n}\delta^4(\vec{x} - \vec{x}_n(\tau_n))d\tau_n \tag{1.6}$$

---

[5]The term $\frac{1}{\sqrt{-g}}$ comes from the transformation of the delta $\delta^4(\vec{\xi} - \vec{\xi}_n) = \frac{\delta^4(\vec{\xi}-\vec{\xi}_n)}{\sqrt{-g}}$ and g is the determinant of the metric tensor.

which describes the non-interacting cloud of particles both in flat and curved spacetime: in flat spacetime and in a locally inertial frame $\sqrt{-g} = 1$ that is the Eq. 1.4 indeed.

$T^{\alpha\beta}$ has several proprieties, for example: it is symmetric and this can be seen by substituting $p_n^\beta = \frac{E_n}{c^2} \frac{d\xi_n^\beta(t)}{dt}$ in Eq. 1.4 obtaining $p_n^\alpha p_n^\beta$; in *flat* spacetime it satisfies the conservation law $T^{\alpha\beta}{}_{,\beta} = 0$: in an enclosed volume V the **energy** conserves ($\int_V T^{00} dV = constant$) and the **momentum** ($\int_V T^{i0} dV = constant$) as well.

An interesting case is the one of the *perfect fluid* that corresponds to the study of a *neutron star* (the focus of this work). Here, the stress-energy tensor assumes the expression

$$T^{\mu\nu} = \begin{pmatrix} \epsilon & 0 & 0 & 0 \\ 0 & p & 0 & 0 \\ 0 & 0 & p & 0 \\ 0 & 0 & 0 & p \end{pmatrix}$$

that it also can be written as

$$T^{\mu\nu} = (\epsilon + p)u^\mu u^\nu + p\eta^{\mu\nu}$$

$u^\alpha = (1, 0, 0, 0)$ is the four velocity associated to the fluid element in the LICF system (*Locally inertial comoving frame*). Since in a LICF $g^{\mu\nu} \equiv \eta^{\mu\nu}$, it becomes

$$T^{\mu\nu} = (\epsilon + p)u^\mu u^\nu + pg^{\mu\nu}$$

By analyzing the components, it can be seen that

- $T^{00} = \epsilon$ is the *density energy*;

- $T^{0i} = 0$ because a perfect fluid has no heat exchange;

- $T^{ki} = \delta^{ki} p$. A perfect fluid hasn't tangential stress, so the force that is exerted on the surface orthogonal to the axis x^k is must be parallel to axis x^k. The pressure is, by definition, the ratio of the force orthogonal to the surface and the surface itself or simply the force per unit surface.

$\frac{G}{c^4}$. Last but non least, the constant $\frac{G}{c^4} = 8 \cdot 10^{-50} \frac{s^2}{g \cdot cm}$: it is the reason why gravitational waves are extremely weak.

Now that all the elements of Eq. 1.1 have been discussed, it's time to introduce the *perturbative approach*. With another approach, the *exact* approach, there have been extracted solutions only in cases with particular symmetry as plane, spherical or cylindrical symmetry; a famous example is the Schwarszchild solution that implies static (*timelike* Killing vector) and spherical symmetry (three *spacelike* Killing vectors). Instead, the perturbative approach, as the name suggests, consists of a first-order perturbation of the zero-order metric

$$g_{\mu\nu} = \eta_{\mu\nu} + h_{\mu\nu} \tag{1.7}$$

where the order zero is represented by $\eta_{\mu\nu} = diag(-1, 1, 1, 1)$ that is the Minkowsky metric (flat spacetime) while $h_{\mu\nu}$ is the metric perturbation that needs to satisfy the condition

$$|h_{\mu\nu}| \ll |\eta_{\mu\nu}| = 1 \tag{1.8}$$

called **weak field**.

Eq. 1.1 will be affected by this new perturbed form of the metric tensor $g_{\mu\nu}$. For the stress-energy tensor $T_{\mu\nu}$ it is

$$T_{\mu\nu} = T^0_{\mu\nu} + \delta T_{\mu\nu}$$

By performing all the calculation ([16]) and by taking only the *first* order perturbation i.e. the elements in $h_{\mu\nu}$ whilst discarding the terms in $O(h^2)$, the solution is

$$\Box_F h_{\mu\nu} - \left[\frac{\partial^2}{\partial x^\lambda \partial x\mu} h^\lambda_\nu + \frac{\partial^2}{\partial x^\lambda \partial x\nu} h^\lambda_\mu - \frac{\partial^2}{\partial x^\mu \partial x\nu} h^\lambda_\lambda \right] = -\frac{16\pi G}{c^4} \left(\delta T_{\mu\nu} - \frac{1}{2} \eta_{\mu\nu} \delta T \right) \tag{1.9}$$

where $\Box_F = (-\frac{1}{c^2} \frac{\partial^2}{\partial t^2} + \nabla^2)$ is the d'Alambertian in flat spacetime.

In order to simplify Eq. 1.9, it is convenient to choose a coordinate system in which the *harmonic gauge* condition is satisfied

$$g^{\mu\nu} \Gamma^\lambda_{\mu\nu} = 0$$

that leads to

$$\frac{\partial}{\partial x^\mu} h^\mu_\nu = \frac{1}{2} \frac{\partial}{\partial x^\nu} h^\mu_\mu \tag{1.10}$$

Using this the terms in square brackets in Eq. 1.9 vanish.

If the present reference frame *doesn't* satisfy the gauge condition, one can make the following infinitesimal coordinate transformation

$$x'^\mu = x^\mu + \epsilon^\mu(x)$$

where, starting from the reference frame of coordinates x^μ one arrives in another of coordinates x'^μ; ϵ^μ is an arbitrary vector such that $\frac{\partial \epsilon^\mu}{\partial x^\mu}$ is the same order of $h_{\mu\nu}$. In this new frame, the gauge condition is satisfied if it is provided that

$$\Box_F \epsilon_\rho = \frac{\partial h^\beta{}_\rho}{\partial x^\beta} - \frac{1}{2} \frac{\partial h^\beta{}_\beta}{\partial x^\rho} \tag{1.11}$$

As last step, it is useful to introduce the tensor

$$\bar{h}_{\mu\nu} \equiv h_{\mu\nu} - \frac{1}{2} \eta_{\mu\nu} h$$

So Eq 1.9 and Eq. 1.10 which are

$$\begin{cases} \Box_F h_{\mu\nu} = -\frac{16\pi G}{c^4} \left(\delta T_{\mu\nu} - \frac{1}{2} \eta_{\mu\nu} \delta T \right) \\ \frac{\partial}{\partial x^\mu} h^\mu_\nu = \frac{1}{2} \frac{\partial}{\partial x^\nu} h^\mu_\mu \end{cases} \tag{1.12}$$

become

$$\begin{cases} \Box_F \bar{h}_{\mu\nu} = -\dfrac{16\pi G}{c^4}\delta T_{\mu\nu} \\ \dfrac{\partial}{\partial x^\mu}\bar{h}^\mu_\nu = 0 \end{cases} \tag{1.13}$$

and outside the source where $\delta T_{\mu\nu} = 0$

$$\begin{cases} \Box_F \bar{h}_{\mu\nu} = 0 \\ \dfrac{\partial}{\partial x^\mu}\bar{h}^\mu_\nu = 0 \end{cases} \tag{1.14}$$

The perturbation of the metric has ten independent components, but not all of them have a physical meaning. In order to understand which, the *TT gauge* (Transverse[6] and Traceless) is needed. This is given by the condition

$$\Box_F \epsilon^\mu = 0$$

that comes from the infinitesimal coordinates transformation written above where in both the reference frames the gauge condition is satisfied. From the four function of ϵ^μ ($\mu = 0, 1, 2, 3$) one can choose four quantities to put equal to zero.
For a travelling gravitational wave in z direction, one can take

$$\bar{h}^t_x = \bar{h}^t_y = \bar{h}^t_z = \bar{h}^y_y + \bar{h}^z_z = 0 \tag{1.15}$$

From the gauge condition it follows that

$$\bar{h}^t_t = \bar{h}^x_t \qquad\qquad\qquad \bar{h}^t_y = \bar{h}^x_y \tag{1.16}$$
$$\bar{h}^t_x = \bar{h}^x_x \qquad\qquad\qquad \bar{h}^t_z = \bar{h}^x_z \tag{1.17}$$

So, given Eq. 1.15 it is also

$$\bar{h}^x_x = \bar{h}^x_y = \bar{h}^x_z = \bar{h}^t_t = 0$$

The remaining *non-vanishing* components are $\bar{\boldsymbol{h}}^z_y$ and $\bar{\boldsymbol{h}}^y_y - \bar{\boldsymbol{h}}^z_z$. It's true then that

$$h_{\mu\nu} = \begin{pmatrix} 0 & 0 & 0 & 0 \\ 0 & 0 & 0 & 0 \\ 0 & 0 & h_{yy} & h_{yz} \\ 0 & 0 & h_{yz} & -h_{yy} \end{pmatrix}$$

In conclusion, there are two physical degree of freedom which corresponds to the two polarization states, h_+ (two equal indices) and $h_\times$.

$$h_{\mu\nu} = \begin{pmatrix} 0 & 0 & 0 & 0 \\ 0 & 0 & 0 & 0 \\ 0 & 0 & h_+ & h_\times \\ 0 & 0 & h_\times & -h_+ \end{pmatrix}$$

---

[6]As the name suggests, Transverse indicates that the components of $h_{\mu\nu}$ different from zero are on the plane orthogonal to the direction of propagation, i.e. *transverse.*

After this example, it's now time to introduce a more *complete* resolution of Einstein's field equations. Starting from Eq. 1.13 [7] which lays on **weak field** approximation, i.e. Eq. 1.8, the goal is the solution in the *quadrupole* formalism. The second approximation that needs to be made is the **slow motion** one. Given a region (with radius ϵ) in which the source of GW is confined

$$|x^i| < \epsilon$$

(where $T_{\mu\nu} \neq 0$) it's required that said region is smaller than the wavelength of the emitted radiation $\lambda_{GW} = \frac{2\pi c}{\omega}$ that implies

$$\frac{2\pi c}{\omega} \gg \epsilon \qquad \rightarrow \qquad \epsilon\omega \ll c \qquad \rightarrow \qquad v_{source} \ll c \qquad (1.18)$$

which is the **slow motion** approximation. After several calculation that can be found in [16], thanks to Eq. 1.18 one arrives to the solution

$$\bar{h}_{\mu\nu}(t,r) = \frac{4G}{c^4} \frac{1}{r} \int_V T_{\mu\nu}(t - \frac{r}{c}, x^i) d^3x \qquad (1.19)$$

This is the perturbation of the metric $\bar{h}_{\mu\nu}$ at distance r (from the origin of the reference system which is centered in the source) at time t generated by the source of volume V at time $t - \frac{r}{c}$.
By defining

$$q^{kn}(t) = \frac{1}{c^2} \int_V T^{00}(t, x^i) x^k x^n d^3x$$

that is called *quadrupole moment tensor* and from the *Tensor Virial Theorem*

$$\frac{1}{c^2} \frac{\partial^2}{\partial t^2} \int_V T^{00} x^k x^n d^3x = 2 \int_V T^{kn} d^3x \qquad (1.20)$$

which gives

$$\int_V T^{kn}(t, x^i) d^3x = \frac{1}{2} \frac{d^2}{dt^2} q^{kn}(t)$$

it's possible to express the solution above in the *quadrupole* approximation.
The solution of Einstein's field equations in **weak field** and **slow motion** approximation in the *quadrupole* form is

$$\begin{cases} \bar{h}^{\mu 0} = 0 & \mu = 0, ..., 3 \\ \bar{h}^{ik}(t,r) = \frac{2G}{c^4} \frac{1}{r} \cdot [\frac{d^2}{dt^2} q^{ik}(t - \frac{r}{c})] & i, k = 1, 2, 3 \end{cases} \qquad (1.21)$$

It's worth to notice and to discuss the presence of *quadrupole* instead of a *dipole* moment. A system of accelerated charged N particles with charge q has a dipole moment different from zero

$$\vec{d}_{EM} = \sum_{i=1}^N q_i \vec{r}_i$$

---

[7]From now and on, $\delta T_\mu \rightarrow T_{\mu\nu}$.

that will emit dipole radiation; for an isolated system of *masses* the dipole moment will be

$$\vec{d}_G = \sum_{i=1}^{N} m_i \vec{r}_i$$

which satisfies the conservation law of the total momentum of an isolated system

$$\frac{d}{dt}\vec{d}_G = \vec{0}$$

and for this reason the dipole contribution in gravitational case, i.e. for GW, is not present. The next term in the expansion is the *quadrupole* moment that *can be* different from zero depending on the source: for instance, a spherical (or axisymmetric) and stationary distribution of matter would not generate a GW signal because the quadrupole moment would be constant, i.e. the first (and so the second) time derivative is zero.

With the aim of showing its physical degrees of freedom, the solution in Eq. 1.21 has to be projected into the *TT gauge* with the *transverse-traceless* operator $\mathcal{P}_{ikmn}$[8]

$$\mathcal{P}_{ikmn} \equiv \mathcal{P}_{im}\mathcal{P}_{kn} - \frac{1}{2}\mathcal{P}_{ik}\mathcal{P}_{mn}$$

where

$$\mathcal{P}_{ik} \equiv \delta_{ik} - n_i n_k$$

Applying it to the tensor $h_{\mu\nu}$ and so to the system of Eq. 1.21

$$h_{ik}^{\mathbf{TT}} = \mathcal{P}_{ikmn}h_{mn} = \mathcal{P}_{ikmn}\bar{h}_{mn}$$

the components of the perturbed metric in the *TT* gauge are

$$\begin{cases} \bar{h}_{\mu 0}^{\mathbf{TT}} = 0 & \mu = 0,...,3 \\ \bar{h}_{ik}^{\mathbf{TT}}(t,r) = \frac{2G}{c^4}\frac{1}{r} \cdot [\frac{d^2}{dt^2}q^{ik}(t - \frac{r}{c})] & i,k = 1,2,3 \end{cases} \tag{1.22}$$

It is useful to define and to use the *reduced quadrupole moment* Q_{ik}

$$Q_{ik} \equiv q_{ik} - \frac{1}{3}\delta_{ik}q_m^m \tag{1.23}$$

that only differs from the quadrupole moment for a constant, i.e. the trace, that cancels in the time derivative; it is also the term which is directly observable and present in the expansion of the newtonian potential[9]. In the *TT gauge* it becomes

$$Q_{ik}^{\mathbf{TT}} = \mathcal{P}_{ikmn}q_{mn} = \mathcal{P}_{ikmn}Q_{mn}$$

At the end of these numerous steps, one finally gets the components that was looking for

$$\begin{cases} h_{\mu 0}^{\mathbf{TT}} = 0 & \mu = 0,...,3 \\ h_{ik}^{\mathbf{TT}}(t,r) = \frac{2G}{c^4 r} \cdot [\frac{d^2}{dt^2}Q_{ik}^{\mathbf{TT}}(t - \frac{r}{c})] \end{cases} \tag{1.24}$$

---

[8]The application of the TT operator $\mathcal{P}_{ikmn}$ is equivalent to the coordinate transformation together with $\Box_F \epsilon^\mu = 0$ condition.

[9]The expansion is $\phi \sim -\frac{M}{r} + \frac{d_j n^j}{r^2} + \frac{3Q_{jk}n^j n^k}{2r^3} + ...$

Another *fundamental* part of the GWs phenomenon is that it carries *energy* taken from the source. This is an important aspect because there are circumstances in which the GWs waves cannot be detected, but their effect (given by the energy loss) can be observed. The *pseudo-tensor* $t^{\mu\nu}$ is useful to the purpose of evaluating the significance of this energy loss. *Pseudo-tensor* means that it acts like a tensor only under a linear coordinate transformation; this happens because it is formed by the *Christoffel symbols* which have this characteristic.

Given a source and an observer who wants to detect the incoming wave along the direction identified by the versor $\mathbf{n} = \frac{r}{|r|}$ (where r is the vector distance between source and observer and $|r|$ the absolute value) the energy per unit time which flows across a unit surface orthogonal to the direction r is

$$
\begin{aligned}
t^{0r} = \frac{dE_{GW}}{dtdS} &= \frac{c^3}{16\pi G} \left[\left(\frac{dh_+^{\boldsymbol{TT}}(t,r)}{dt} \right)^2 + \left(\frac{dh_\times^{\boldsymbol{TT}}(t,r)}{dt} \right)^2 \right] \\
&= \frac{c^3}{32\pi G} \left[\sum_{ik} \left(\frac{dh_{ik}^{\boldsymbol{TT}}(t,r)}{dt} \right)^2 \right]
\end{aligned}
\tag{1.25}
$$

By the fact that in GR the energy of gravitational field can't be defined locally, to find the GW-flux it is requested the average over several wavelenght expressed by $< \cdots >$. By integrating Eq. 1.24 respect to $dS = r^2 d\Omega$, the gravitational luminosity, i.e. the energy carried by the GW per unit time, is

$$
\begin{aligned}
L_{GW} &= \int \frac{dE_{GW}}{dtdS} dS \\
&= \frac{G}{2c^5} \frac{1}{4\pi} \int d\Omega < \sum_{ik} \left(\mathcal{P}_{ikmn} \dddot{Q}_{mn}(t - \frac{r}{c}) \right)^2 > \\
&= \frac{G}{5c^5} < \sum_{k,n=1}^{3} \dddot{Q}_{kn}(t - \frac{r}{c}) \dddot{Q}_{kn}(t - \frac{r}{c}) >
\end{aligned}
\tag{1.26}
$$

This was the formula derived by Albert Einstein in 1918 and published in the paper *Über Gravitationswellen*.

The solutions expressed by Eq. 1.24 and Eq. 1.26 can be applied to a system in which the hypothesis of **weak field** and **slow motion** are verified; when it is not sufficient to describe the system anymore, the *Post-Newtonian* (PN) expansion - that lays on the same hypothesis - is needed for more accuracy. In fact, for a generic metric theory, the PN involves the expansion of the metric and the stress-energy tensor in terms of the parameter $\epsilon \sim \sqrt{\frac{GM}{c^2R}} \sim \frac{v}{c} \sim \frac{p}{\rho}$.

For $g_{\mu\nu}$ the *first* order post-Newtonian expansion involves the potentials

$$
\begin{aligned}
&g_{00}[O(4)] : U^2, \phi_W, \phi_1, \phi_2, \phi_3, \phi_4, \mathcal{A}, \mathcal{B} \\
&g_{jk}[O(2)] : U\delta_{jk}, \chi_{,jk} \\
&g_{0j}[O(3)] : V_j, W_j
\end{aligned}
$$

with U as the Newtonian potential. Then one makes use of parameters in front of the PN metric; the expansion is called *Parameterized Post-Newtonian* (PPN)

and includes 10 parameters: $\alpha_1, \alpha_2, \alpha_3, \beta, \gamma, \xi, \zeta_1, \zeta_2, \zeta_3, \zeta_4$. For *General Relativity* $\beta = \gamma = 1$ where the others are zero. In this particular case

$$g_{00} = -1 + 2U - 2U^2 + 4\phi_1 + 4\phi_2, +2\phi_3 + 6\phi_4$$
$$g_{jk} = (1 + 2U)\delta_{jk}$$
$$g_{0j} = -\frac{7}{2}V_j - \frac{1}{2}W_j$$

The first order PN expansion for $T_{\mu\nu}$ regarding a perfect fluid is

$$T^{00} \rightarrow \rho O(2)$$
$$T^{0j} \rightarrow \rho O(3)$$
$$T^{jk} \rightarrow \rho O(4)$$

being

$$T^{\mu\nu} = (\rho + \rho\Pi + p)u^\mu u^\nu + pg^{\mu\nu}$$

with Π as specific energy density. Further details on $g_{\mu\nu}$ generic explicit form and other metric theories can be found in [39].

1.2 Variety of astrophysical sources

The GW events that have been detected so far are binary coalescing systems composed by BH-BH, NS-BH or NS-NS. They are only a fraction of the possible GW sources that are divided in four main categories.

Burst sources
In this class are included for example supernovae explosions, and so on. Gravitational waves that come from supernova explosion are suppose to radiate below a few kHz and to be generated from instabilities present in the collapse and just after it.

Compact binary coalescence (CBC) This category embraces stars that are falling into massive black holes (MBH) or the binary system discussed above. The binary coalescing compact system is the most known and it has the peculiar waveform called *chirp* which identifies the final stage of the coalescence; the event lasts few minutes in which strong quasi-periodic GWs are radiated. The event rate of NS-NS is estimated to be about 110-3848 $\frac{1}{Gpc^3\ year}$ [3]; for massive black hole binaries (MBH) the event rate is once per year within 3 Gpc. The event rate of burst waves radiated from stars spiraling into MBHs is not well known yet.

Periodic sources
Periodic gravitational waves are radiated by binary stars (far from the coalescence) and from *rotating neutron stars* which are called *pulsars*.

Stochastic sources
Some good examples of stochastic sources are the GWs background originated during the *Big Bang* and the *phase transitions* in the early Universe. The former involves

GWs emitted in the so-called dark age that is an epoch prior to the Big Bang Nucleosynthesis (BBN) and in particularly it refers to a rapidly varying gravitational field during the inflation that can produce a *stochastic background* by the amplification of quantum, vacuum fluctuations. Nowadays, this GW background would be in the frequency range of $10^{-16} - 10^{10}$ Hz which is covered by the detectors. The latter occurs at the end of the inflation when symmetry breaking phase transitions create the cosmic strings which produce GW with their oscillation [14].

1.2.1 Spinning and isolated neutron stars

A Neutron star (NS) is the final fate of a $2M_\odot < M < 20 - 30M_\odot$ star after supernova explosion that can emit GWs if deformities occur. The principal GWs generation mechanisms for a single spinning NS are its elliptical deformities respect to the ideal spherical shape: they can be generated through strong magnetic fields in the core or elastic strains in the crust. Such deformities are called *mountains*. The former mountains (magnetic mountains) can arise in both isolated and accreting NS; the latter (thermal mountains) are sustained by elastic strain in the crust and can only be found in accreting NS because the temperature gradients are generated by asymmetries in the release of the mass done by its companion.

If one considers an ellipsoid with uniform density ρ, the quadrupole moment and inertia tensor

$$q_{ij} = \int_V \rho x_i x_j d^3 x \qquad i = 1, 2, 3 \tag{1.27}$$

$$I_{ij} = \int_V \rho(r^2 \delta_{ij} - x_i x_j) d^3 x \tag{1.28}$$

which together give $q_{ij} = -I_{ij} + \delta_{ij} q$, can then compute the Q_{ij} in terms of the inertia tensor

$$Q_{ij} = -(I_{ij} - \frac{1}{3}\delta_{ij} I) \tag{1.29}$$

and substitute in the quadrupole approximation of Eq. 1.24 to study the form of the perturbed metric.

For a non rotating ellipsoid of mass M and with semiaxes a, b and c, I_{ij} is

$$I_{ij} = \frac{M}{5} \begin{pmatrix} b^2 + c^2 & 0 & 0 \\ 0 & c^2 + a^2 & 0 \\ 0 & 0 & a^2 + b^2 \end{pmatrix} = \begin{pmatrix} I_1 & 0 & 0 \\ 0 & I_2 & 0 \\ 0 & 0 & I_3 \end{pmatrix}$$

where the principal moments of inertia are on the diagonal. For a rigidly-rotating ellipsoid around one of its principal axes, with angular velocity $\Omega = (0, 0, \Omega)$, a second coordinate system is taken. In this co-rotating frame I'_{ij} has the aforementioned expression while in the inertial frame (from which one sees that the ellipsoid is rotating) knowing that $\varphi = \Omega t$, I_{ij} is

$$I_{ij} = \begin{pmatrix} I_1 cos^2\varphi + I_2 sin^2\varphi & -sin\varphi cos\varphi(I_2 - I_1) & 0 \\ -sin\varphi cos\varphi(I_2 - I_1) & I_1 sin^2\varphi + I_2 cos^2\varphi & 0 \\ 0 & 0 & I_3 \end{pmatrix}$$
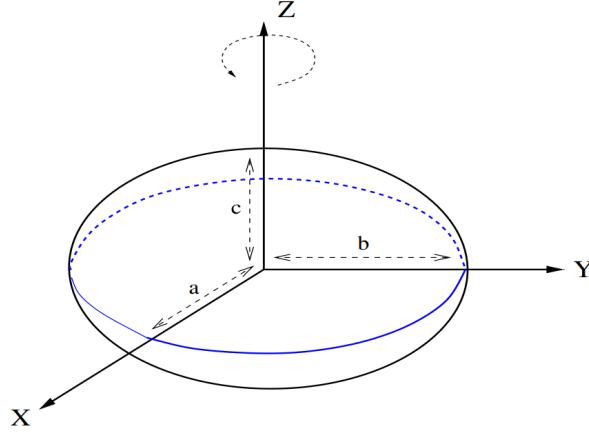
Figure 1.3. The ellipsoid and its semiaxes. The rotation is taken respect to z axes and it's represented by the anti-clockwise arrow [16].

hence

$$Q_{ij} = \frac{I_2 - I_1}{2} \begin{pmatrix} cos2\varphi & sin2\varphi & 0 \\ sin2\varphi & -cos2\varphi & 0 \\ 0 & 0 & 0 \end{pmatrix} + constant$$

By looking at the argument of sine and cosine, one can see that the GW emission frequency is **twice** the rotational one, like in the case of binary coalescence, i.e. $f_{GW} = 2f_{rot}$. The multiplying quantity $\frac{I_2 - I_1}{2}$ expresses the absence of GW emission if $a = b$ because $I_2 = I_1$, therefore for this ellipsoid it is important to deviate from symmetry along the x and y axis. In order to quantify the difference between the semi-axes a and b, it's useful to introduce the *ellipticity ϵ*

$$\epsilon \equiv \frac{a - b}{(a + b)/2} \tag{1.30}$$

and to rewrite the reduced quadrupole moment as

$$Q_{ij} = \frac{\epsilon I_3}{2} \begin{pmatrix} cos2\varphi & sin2\varphi & 0 \\ sin2\varphi & -cos2\varphi & 0 \\ 0 & 0 & 0 \end{pmatrix} + constant$$

that can finally be put in the quadrupole solution giving the amplitude h_0

$$h_0 = \frac{4G\Omega^2}{c^4 r} I_3 \epsilon \tag{1.31}$$

whose normalization is

$$h_0 = 4.21 \cdot 10^{-24} \left[\frac{\text{ms}}{T}\right]^2 \left[\frac{\text{Kpc}}{r}\right] \left[\frac{I_3}{10^{38}\text{kg m}^2}\right] \left[\frac{\epsilon}{10^{-6}}\right] \tag{1.32}$$

If it is assumed that the energy loss is completely due to GW emission (*spin down limit*), an upper limit of the ellipticity ϵ_{sd} can be obtained

$$\epsilon \leq \epsilon_{sd} = \sqrt{\frac{5c^5|\dot{f}|}{512\pi^4 G f^5 I_3}}$$

For the *Crab nebula* pulsar [5] $h_0^{sd} < 1.4 \cdot 10^{-25}$ since no signal has been detected from this source.

Another possible generation mechanism is the case in which the star is freely preceding respect one of its principal axis. Here, the previous condition $a \neq b$ is not demanded, hence $I_1 = I_2$ is now assumed for simplicity. For a small *wobble angle* θ that is the angle of the precession, in the inertial system it is

$$Q_{ij} = (I_1 - I_3)\theta \begin{pmatrix} 0 & 0 & -sin\varphi \\ 0 & 0 & cos\varphi \\ -sin\varphi & cos\varphi & 0 \end{pmatrix} + constant + O(\theta^2)$$

this time, the GW emission frequency **corresponds to** the rotational one, i.e. $f_{GW} = f_{rot}$ and the amplitude of the metric perturbation is [16]

$$h_0 = \frac{2G\Omega^2}{c^4 r}(I_1 - I_3)\theta \tag{1.33}$$

where the deformation depends now - among the other parameters - to the difference $(I_1 - I_3)$ (x/y axis and z axis) and to the wobble angle θ.

Returning to the case of Fig. 1.3, the expression of the ellipticity ϵ - that depends on the mechanism that is taken into account - can be derived. For what concern the magnetic fields, many studies have been made with the aim to understand their actual structure and role on quadrupolar deformation. What is known from some models - because there isn't any direct information about their internal shape - is that purely toroidal or poloidal magnetic fields are *unstable* on dynamical timescales (*Alvén timescale*); so, in order to be a reliable and durable source of deformities, the structure has to be *"mixed"* as the so-called *twisted-torus*: the poloidal magnetic field goes throughout the star, from the inside to the outside while the toroidal field is confined in a torus-shaped region inside the star as reported in Fig. 1.4.

The deformations due to this configuration can be estimated as [23]

$$\epsilon_B \sim 4.5 \cdot 10^{-7} \left(\frac{B_p}{10^{14}\text{G}}\right)^2 \left(1 - \frac{0.389}{\Lambda}\right) \tag{1.34}$$

where B_p is the poloidal component of the surface magnetic field, Λ is the ratio between poloidal-to-total component ($\Lambda = 0$ purely toroidal, $\Lambda = 1$ purely poloidal) - or equivalently [17]

$$\epsilon_B \sim 10^{-5} B_p^2 \left(1 - 0.64 \frac{< B_{tor}^2 >}{< B_{pol}^2 >}\right) \tag{1.35}$$

Eq. 1.34 is particularly pessimistic for GW because only a few stars such as the magnetars have a high magnetic field of order $B_p \sim 10^{14}$G. The model discussed above doesn't consider the existence of superconducting matter: for a non-superconducting NS $\epsilon_B \sim B^2$ as previously written, but $\epsilon_B \sim B$ if there is a superconducting phase. A first superconducting model is the two-fluid one where in the outer core neutrons form a superfluid and the protons can be either a normal fluid or superconductor, but exotic states of matter allow even higher ellipticities: the exotic proprieties of
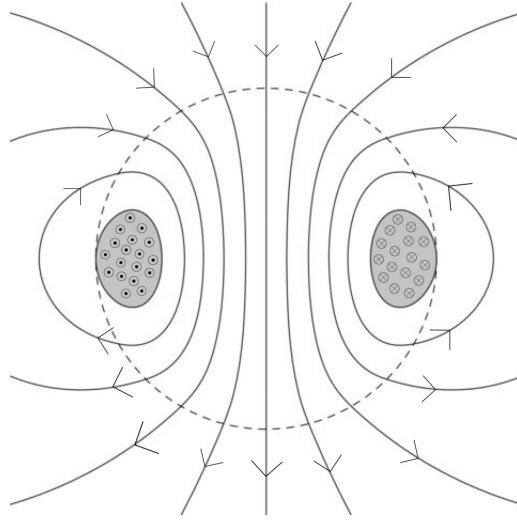
Figure 1.4. The dashed line represents the star surface while the solid ones the poloidal components of the magnetic field and the donut-shaped region in dark grey is the toroidal magnetic field, adapted from [6].

the color-superconducting phase of quarks could accommodate this demand (Fig. 1.5). Two of the quark composition possibilities are: the *color-flavor-locked* (CFL) phase and the *two-flavor superconducting* (2SC) state for which the ϵ are

$$\epsilon^{CFL} \sim 1.2 \cdot 10^{-5} \frac{<B>}{10^{14}\text{G}} \qquad\qquad \epsilon^{2SC} \sim 4.0 \cdot 10^{-6} \frac{<B>}{10^{14}\text{G}} \qquad (1.36)$$

with $<B>$ as the average magnetic field in the core.

 A last consideration on the role of magnetic field can be made about the situation in which the rotational axis and the magnetic dipole moment of the NS are misaligned. This leads the star to a precession characterized by the angle χ between the two axes and an emission frequency $f_{GW} = f_{rot}$. The resulting strain amplitude of a GWs is [34]

$$h_0 = 6.48 \cdot 10^{-30} \frac{\beta}{sin^2\chi} \left(\frac{R}{10\text{ km}}\right)^2 \left(\frac{1\text{ kpc}}{d}\right) \left(\frac{1\text{ ms}}{P}\right) \left(\frac{\dot{P}}{10^{-13}}\right)$$

β is the magnetic distortion factor and quantifies the distortion in the star due to the magnetic structure. This coefficient is linked to the ellipticity through the relation $\epsilon = \beta\mathcal{M}^2/\mathcal{M}_0^2$ where $\mathcal{M}$ is the magnetic dipole moment and $\mathcal{M}_0$ has the dimension of a dipole moment in order to have β dimensionless. The strain h_0 grows if $\chi \to 0$ or for large β. It is clear that χ can't be too small due to its position in the equation above.

The second typology of mountains, *thermal mountains*, can be found in Low-mass X-ray Binaries (LMXBs) which are binary systems composed by a star in its main sequence - the donor - and a NS/BH - the accretor. The mass on the accretor is buried and compressed until nuclear reactions occur; these reactions heat the crust and generate a temperature gradient: since the mass release is asymmetric, the heating and so the gradient will be too. Thanks to the temperature gradient,
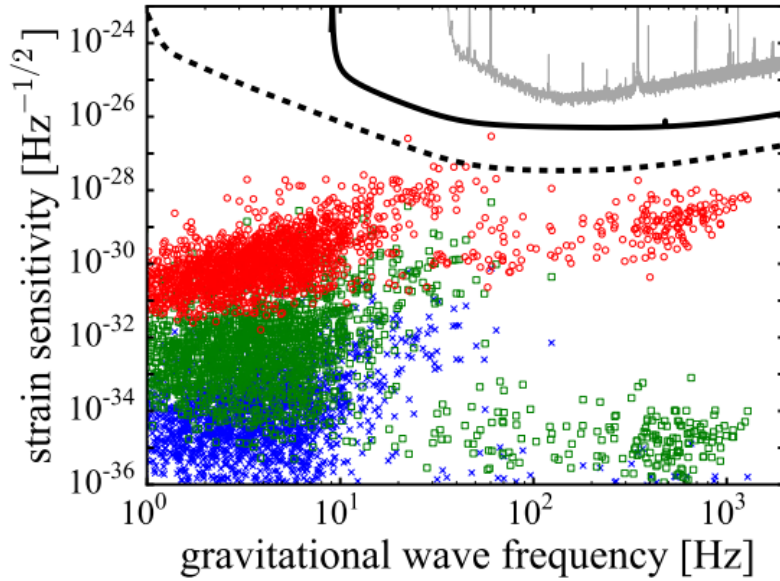
Figure 1.5. The blue crosses and the green squares are for normal (i.e. non superconducting) NS matter where the former is for pure poloidal magnetic field and the latter for an almost pure toroidal one ($\Lambda = 0.01$); the red circles represent the superconducting CFL model provided $< B >= 10B_p$. Black dashed curve is the projected strain sensitivity for Einstein Telescope (ET) whilst the solid one is for aLIGO and the grey one is the strain sensitivity for the initial S5 run with two years of coherent integration [23].

quadrupolar deformations arise and are sustained by elastic strain of the crust - for this reason they are included in the class of elastic mountains. The ellipticity associated to this phenomenon is

$$\epsilon_{th} \sim 10^{-10} R_6^4 \left(\frac{\delta T_q}{10^5 \text{K}}\right) \left(\frac{Q}{30 \text{MeV}}\right)^3 \qquad (1.37)$$

Q is the threshold energy of electron capture by nuclei (one of the reactions that occur in the crust); δT_q is the quadrupolar thermal gradient which is a fraction of the total thermal gradient δT and, in the most optimistic scenario, $\delta T_q \lesssim 0.1\delta T \lesssim 10^5 K$; R_6 is the stellar radius. If ϵ_{th} is substituted in the amplitude formula h_0 according to the expression in [17], the output value is $h_0 \sim 10^{-27} - 10^{-28}$ which is too weak to be detected by aLIGO/Virgo but potentially not for ET if $\delta T_q/\delta T$ is not smaller than ~ 0.1. By the fact that these thermal mountains belong to the elastic mountains class, they depend on the stress that the crust can sustain before breaking that is

$$\epsilon_{th} \lesssim \frac{\mu_{cr}\sigma_{br}V_{cr}}{GM^2/R} \sim 10^{-5} \left(\frac{\sigma_{br}}{0.1}\right)$$

μ_{cr} is the shear modulus of the crust, V_{cr} the volume of the crust and σ_{br} the crustal breaking strain which maximum value can be ~ 0.1.

A last remarkable example of instability in rotating stars is the *unstable oscillation modes.* For what concern "normal" neutron stars (i.e. not magnetars), it's worth to

focus on *secular* rather than dynamical instabilities of normal modes formulated in the Chandrasekhar, Friedman and Schutz (CFS) theory. Two are the requisites for the onset of secular CFS instability: the change in sign of mode velocity and the coupling to a dissipative mechanism. The first request involves two frames, one is co-rotating with the star and the other is inertial. If the counter-moving mode in the co-rotating frame appears co-moving with the star in the inertial frame, then the request is satisfied; this means that the pattern speed [7]

$$\sigma_p = \frac{d\varphi}{dt} = -\frac{\omega_i}{m}$$

changes sign from negative (co-moving frame) to positive (inertial frame). From the relation $\omega_i = \omega_r - m\Omega$, this is achieved if the stellar angular frequency Ω is

$$\Omega > \frac{\omega_r}{m} \tag{1.38}$$

where ω_i is the angular frequency in the *inertial* frame and ω_r in the co-*rotating* frame.

For the second condition, it turns out that the GW radiation is often the dominant dissipative mechanism and it is effective when its emission is faster than the viscous damping rate i.e. $\tau_{GW} < \tau_{visc}$. Among the several oscillation modes that satisfy both the conditions, the two most important are the *fundamental f-mode* and the *inertial r-mode* (Coriolis force as restoring force). The *f-modes* are the first order of the *p-modes* instabilities which are *pressure* driven instabilities: it has been seen that, due to the strong reduction of the instabilities caused by superfluid vortex array, the only realistic candidate for these modes could be newly born and fast rotating NS called supramassive neutron star[10] with hot non-superfluid matter [17]. *r-modes* are quite a lot more interesting because they could be a real observable GW emission mechanism. In absence of dissipation, the instability is guaranteed for any Ω by the fact that the pattern velocities are

$$\sigma_r = -\frac{2\Omega}{l(l+1)} < 0 \qquad\qquad \sigma_i = \Omega\frac{(l-1)(l+2)}{l(l+1)} > 0$$

When the dissipation is switched on, an $\Omega - T$ instability window has to be taken into account [17] and it is wider than the *f-mode* one ($min\Omega_c = 0.045\Omega_{max}$ of *r-modes* against the $min\Omega_c = 0.91\Omega_{max}$ of *f-modes* [28] in order to satisfy $\Omega > \Omega_c$ for the change in sign of the pattern velocity).

To describe these modes, one starts by defining the displacement vector $\vec{\xi}$ which represents the perturbation from the equilibrium and hence the oscillation of the fluid. This displacement leads to a variation of the fluid velocity $\vec{u}$

$$\delta\vec{u} = \partial_t\vec{\xi}$$

In addition, one assumes an harmonic time-dependence of the modes which is

$$\vec{\xi} \to \vec{\xi}e^{i(m\varphi+\omega_r t)}$$

---

[10]This is the post-merger remnant of mass $1.2M_{TOV} \lesssim M \lesssim 1.5M_{TOV}$ where M_{TOV} is the Tolman-Oppenheimer-Volkoff mass [33].

to perturb Euler equations [7]. There exist two classes of displacement: spheroidal and toroidal

$$
\begin{cases}
\frac{\vec{\xi}}{r} = \sum_{lm} \left(S_{lm}, H_{lm}\partial_\theta, \frac{H_{lm}}{sin\theta}\partial_\varphi \right) Y_{lm} & spheroidal \\
\frac{\vec{\xi}}{r} = \sum_{lm} \left(0, \frac{T_{lm}}{sin\theta}\partial_\varphi, -T_{lm}, \partial_\theta, \right) Y_{lm} & toroidal
\end{cases}
\tag{1.39}
$$

with $Y_{lm}(\theta, \varphi)$ as the standard spherical harmonics. The overall displacement in the case of rotating star is

$$
\frac{\vec{\xi}}{r} = T + S = \sum_{lm} \left(0, \frac{T_{lm}}{sin\theta}\partial_\varphi, -T_{lm}, \partial_\theta, \right) Y_{lm} + \sum_{\nu=l\pm1} \left(S_{lm}, H_{lm}\partial_\theta, \frac{H_{lm}}{sin\theta}\partial_\varphi \right) Y_{\nu m}
\tag{1.40}
$$

the advantage of the rotating case is the disappearance of m degeneracy although it is more complicated to describe due to the fact that $[l, m]$ toroidal mode couples to the $[l\pm1, m]$ spheroidal one. By taking the $l = m$ case for slowly rotating barotropic stars, the velocity perturbation in the co-rotating frame is [28]

$$
\delta\vec{u} = \alpha\Omega R \left(\frac{a}{R} \right)^l \vec{Y}_{ll}^B e^{i\omega_r t}
$$

where α is a dimensionless amplitude, $\vec{Y}_{ll}^B$ are the magnetic multipoles introduced by Thorne [36] and a ranges from 0 to R of the non-rotating star. At leading order i.e. $\omega_r \approx \frac{2m\Omega}{l(l+1)}$, and for the case of $l = m = 2$ which is dominant for GW emission, the velocity field results in a elliptical shape whilst the single elements of fluid have ellipses with θ-dependent eccentricities and move according to

$$
\begin{cases}
\delta r \approx 0 \\
\delta\theta \propto \alpha sin\theta cos(m\varphi + \omega_r t) \\
\delta\varphi \propto \alpha sin\theta cos\theta sin(m\varphi + \omega_r t)
\end{cases}
$$

This is well illustrated in Fig. 1.6.

The GW emission - which occurs at $f_{GW} = \frac{4}{3}f_{rot}$ - takes away positive angular momentum from the rotating star; this positive angular momentum is subtracted from the negative angular momentum of the mode making it more negative and growing the amplitude of oscillation hence the mode falls in a positive-feedback: as the amplitude of the mode grows, there is an increase of the positive angular momentum emitted and therefore a more negative angular momentum of the mode [23], [31].

The strain associated to the *r-modes* is [34]

$$
h_0 = 4.4 \cdot 10^{-24}\alpha \left(\frac{\omega_r}{\sqrt{\pi G\bar{\rho}}} \right)^3 \left(\frac{20 \text{ Mpc}}{d} \right)
\tag{1.41}
$$

where α is the dimensionless parameter associated to the *r-modes* and $\bar{\rho}$ the mean density.
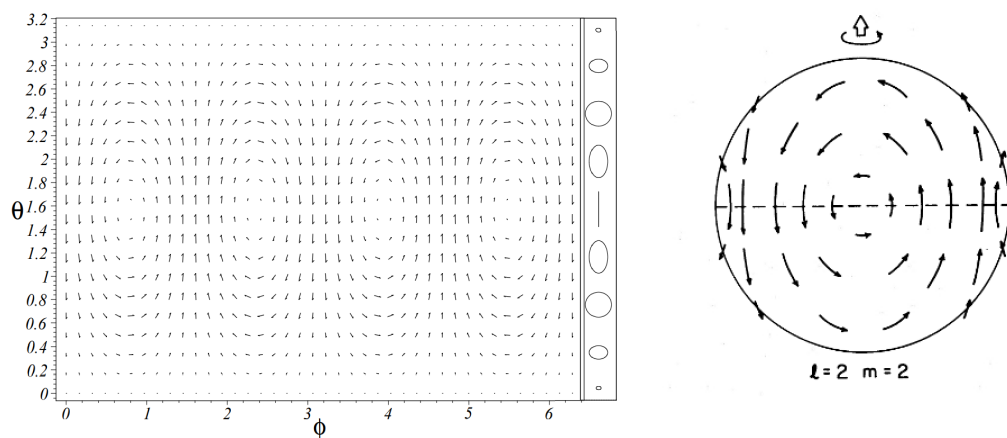
Figure 1.6. The main figure on the left represents the field velocity in the case of slow motion and at leading order $l = 2$ with $l = m = 2$. The narrow vertical slice contains the trajectory of the single fluid element around an equilibrium θ position: when $\theta \to 0, \pi$ the ellipses approach circles and the radius shrinks to zero; for $\theta \to \pi/2$ (equator) the trajectory is a line in which the fluid elements moves up and down respect to θ direction [7].

The figure on the right is a further focus of the field velocity for $l = m = 2$, but other modes (even $l \neq m$) can be found in [32].

1.3 Types of searches

Rapidly spinning neutron stars are the most promising continuous wave (CW) sources, but their search can be almost unmanageable from a computational point of view depending on the a priori knowledge of the source parameters. For a single source these parameters are its frequency and all the spin-down orders, the most important of which are $\dot{f}_0$ and $\ddot{f}_0$: the first order of spin down ($\dot{f}_0$) gives a description of the variation of the frequency of the source while how this variation changes during time comes from the second order ($\ddot{f}_0$). In the case of binary system, more parameters add to the previous ones as the ellipticity, the inclination of the orbit and the period. According to this a priori knowledge, research strategies for CW radiation are divided into three main categories: *targeted* searches in which star position, rotational frequency and all the spin-down orders are known; *directed* searches in which only the position is assumed as known[11]; *All-sky* for unknown position-and-frequency-evolution stars. From the first to the third category, the parameter space volume that need to be studied grows because more parameters are left unknown. There exist grey regions between them, as for example the narrow-band searches in which the sky position and the rotational parameters are known, but they refer to a more relaxed emission model in which the relation between f_{GW} and f_{rot} is not constrained. Because more computational resources can be focused on less parameters, the targeted search has the best sensitivity respect to the others classes but it is limited to known pulsars. All of this is well summarized in Fig. 1.7.
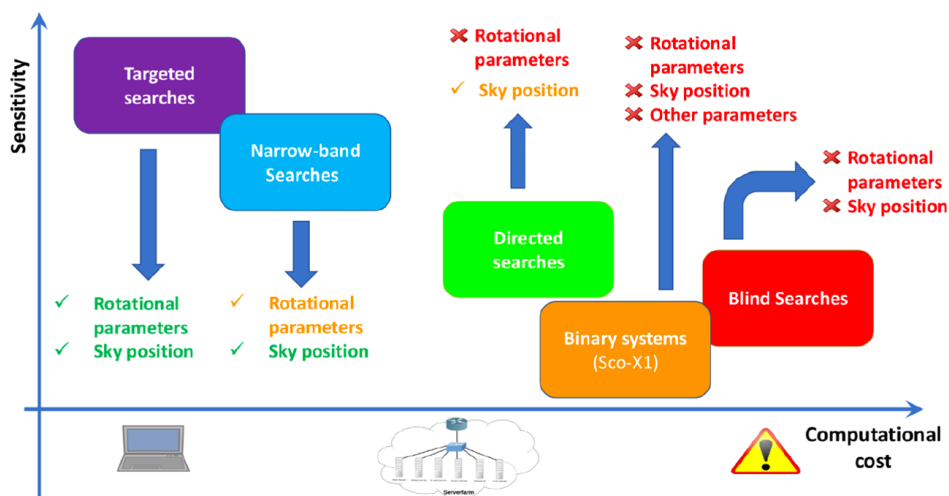

Figure 1.7. The figure contains sensitivity vs computational cost of several search strategies: the more parameters are left unknown the higher the computational cost. Nowadays, one refers to the *blind* searches as *all-sky* searches.

From a recent (2018) method strategy in the directed searches, therefore for a fixed sky location, it has been estimated a computational time equal to 2.4 CPU hours for a one month data of a single detector in order to recover the 131 fake signals in

---

[11]In the case of supernova remnant, the nebula that surrounds the NS is quite large, therefore the NS position is obtained thanks to several information in the electromagnetic spectrum.

[70-200] Hz frequency band, hence a very fast approach [24]. A CPU is the acronym for *Central Processing Unit*, the processor that executes the instructions.

In the last years, new computing strategies were born as the GPU which stands for *Graphical Processing Unit* that performs computations with high parallelism and efficiency. The new GPU is preferred to the old CPU in the most computational demanding searches. Giving some further details, the specific role in 2018 of the Italian center of calculus CNAF[12] for the Virgo CW searches regarding only the Hough transform (a step of the All-sky pipeline FrequencyHough) a total of 10^6 CPU hours have been used at CNAF for CW searches. For the All-sky searches at CNAF there are needed 30 million of cores per hour considering three detectors for a year. This request of 30 MSU, if the energy is distributed over 1 year, implies $30 \cdot 10^6 \frac{1}{365} \frac{1}{24} \sim 3425$ cores every hour. One core at CNAF is equal to 11 HS06[13] with 2 GB of RAM. For what concerns the operative system, it makes use of nodes of 36/72 cores each with 3G per core.

As last information, for the LIGO detectors a complete search on the 9 months long run can be accomplished in a couple of months with 200 GPUs whilst there are needed several months and 2000 CPUs in the old system [11].

Among the several CW searches, here I will focus on *isolated* and spinning neutron stars in the *All-sky* searches that are the subject of this work after having briefly described the *targeted* and *directed*.

1.3.1 Signal model

Considering a source, precisely a rigid rotating NS, that produces a strain which can be written as

$$h(t) = F_+(t, \psi) h_0 \frac{1 + cos^2(\iota)}{2} cos(\Phi(t)) + F_\times(t, \psi) h_0 cos(\iota) sin(\Phi(t)) \qquad (1.42)$$

where ι is the angle between star spin direction and the propagation direction of the GW, $F_+, F_\times$ are the detector radiation patterns (the "sensitivity" to h_+ or $h_\times$ polarization), ψ is the polarization angle and Φ the phase of the signal that has to be corrected and whose Taylor series expansion is [2]

$$\Phi(\tau) = \phi_0 + 2\pi \left[f_0(\tau - \tau_r) + \frac{1}{2} \dot{f}_0(\tau - \tau_r)^2 + \frac{1}{6} \ddot{f}_0(\tau - \tau_r)^3 \right] \qquad (1.43)$$

f_0, $\dot{f}_0$ and $\ddot{f}_0$ are the intrinsic source frequency, first and second order spin-down at the fiducial time τ_r, ϕ_0 is the initial phase, τ is the time at the source and t is the arrival time of the signal at the detector

$$\tau(t) = t + \frac{\vec{r}(t) \cdot \hat{n}}{c}$$

$\vec{r}(t)$ is the vector which joins the solar system barycenter (SSB) and the detector and $\hat{n}$ identifies the source position in the SSB. Here, the two Shapiro and Einstein time delays are getting neglected.

---

[12]It the national center the INFN (Istituto Nazionale di Fisica Nucleare) who is in control of the management and development of the principal information services and data for INFN.

[13]It is used for measuring CPU performance.

The signal emitted by the source is then subject to the Doppler effect only that is caused by the detector movement which has a velocity $\vec{v}$ respect to the SSB; this velocity is composed by the Earth orbit around itself ($\vec{v}_{rot}$) and around the Sun ($\vec{v}_{orb}$). Giving that

$$f(t) = \frac{1}{2\pi}\frac{d\Phi}{dt}$$

then this shift is described by

$$f(t) \simeq f_0 \left(1 + \frac{\vec{v}\cdot\hat{n}}{c}\right) \approx f_0 \left(1 + \frac{\Omega_{orb}R_{orb}cos\beta sin(\Omega_{orb}t)}{c}\right) \qquad (1.44)$$

where f_0 is always the intrinsic frequency of the source, Ω_{orb} is the Earth orbital angular velocity, R_{orb} the radius of that orbit and β the latitude of the source.

1.3.2 Targeted searches

Electromagnetic active pulsars are perfect candidates for this category thanks to the ephemerides measured from observation in the electromagnetic band (X-ray, γ-ray, optical, radio) and an accurate Doppler correction can be applied to these sources along with other GR effects. The correction can be accomplished through different methods: 5-vector which adopts the matched filter approach, $\mathcal{F}/\mathcal{G}$ statistic and the time-domain heterodyne-based pipelines (like Bayesian and Band Sampled Data). For example, regarding the Crab pulsar, the 5-vector analysis method computed an ellipticity ϵ of $16.3(15.7)\cdot 10^{-6}$ ($h_0^{95\%} = 3.0(2.9)\cdot 10^{-26}$), while the $\mathcal{F}/\mathcal{G}$ statistic $10(8.1)\cdot 10^{-6}$ ($h_0^{95\%} = 1.9(1.5)\cdot 10^{-26}$) and the Bayesian one $8.6(7.4)\cdot 10^{-6}$ ($h_0^{95\%} = 1.5(1.2)\cdot 10^{-26}$) [5].

1.3.3 Directed searches

For directed searches, a coherent integration of the observation time is not possible due to the knowledge of the position alone i.e. there is no information about the evolution of the phase. The computational cost depends on the nominal/intrinsic GW frequency and its derivatives $f_0, \dot{f}_0, \ddot{f}_0$ and grows accordingly to the observation time. In order to use computational resources effectively, a semi-coherent approach is applied to the data rather than a coherent procedure. The semi-coherent technique reduces computational cost by dividing into short segments the data that are analyzed coherently and then combined incoherently; unfortunately, the procedure reduces the sensitivity respect to a full coherent analysis. For example, from three directed search methods: BSD, Single-harmonic Viterbi and the Dual-harmonic Viterbi; the most strict constrains on the intrinsic GW strain from a sample of 15 supernova remnants comes from the BSD with $h_0^{95\%} \approx 7.7\cdot 10^{-26}$ for G39.2-03 and $h_0^{95\%} \approx 7.87\cdot 10^{-26}$ for G65.2+1.2 around 200 Hz [35].

1.3.4 All-sky searches

All-sky searches look for NS without electromagnetic counterpart: $10^8 - 10^9$ NS are supposed to populate the Milky Way, but only $\sim 2\cdot 10^3$ have been discovered thanks

to their electromagnetic signals. Hence, in this case, the detection of a CW would increase the number of known pulsars.

In the All-sky procedure, the Doppler and the antenna pattern corrections are sky-dependent since phase and position are unknown, making the computational cost high. If one considers for a *fixed* signal frequency f_0 a bin of size δf which is $\delta f = 1/T_{FFT}$, then the angular resolution

$$\delta\theta \approx 9 \cdot 10^{-3} rad \left(\frac{30 \text{ minutes}}{T_{FFT}}\right) \left(\frac{300 \text{ Hz}}{f_0}\right)$$

If $T_{FFT} = 1$ year and $f_0 = 1$ kHz $\rightarrow \delta\theta \sim 0.3$ μrad and the number of sky points $\sim 1/(\delta\theta)^2$ is of order $O(10^{14})$. If more parameters like $\dot{f}_0$ and $\ddot{f}_0$ are included in this 1 year data, the coherent analysis is unmanageable; hence a different strategy has to be used. By dividing the total observation time in N segments, i.e. $N = T_{obs}/T_{FFT}$, each of which is analyzed coherently and then the results are added incoherently (therefore a semi-coherent analysis is performed) a good compromise between strain sensitivity and computational cost is reached with a degradation in sensitivity $\sim N^{1/4}$ as T_{FFT} increases but also with the advantage of more robustness with respect to deviation of a signal compared to a coherent model.

Several search pipelines of semi-coherent analysis are based on the Hough transform as SkyHough and **FrequencyHough**, but others use the StackSlide algorithm as PowerFlux or can lay on the $\mathcal{F}$-statistic as Einstein@Home. Fig. 1.8 gives a view of the strain amplitude obtained from these several techniques. From these methods, the best limit on the strain amplitude $h_0^{95\%}$ is for O3 data using PowerFlux, near 200 Hz, $h_0^{95\%} \sim 1.7 \cdot 10^{-25}$ (linearly polarized), $h_0^{95\%} \sim 6.3 \cdot 10^{-26}$ (circularly polarized) and $h_0^{95\%} \sim 1.4 \cdot 10^{-25}$ (population-averaged ensemble) [27].
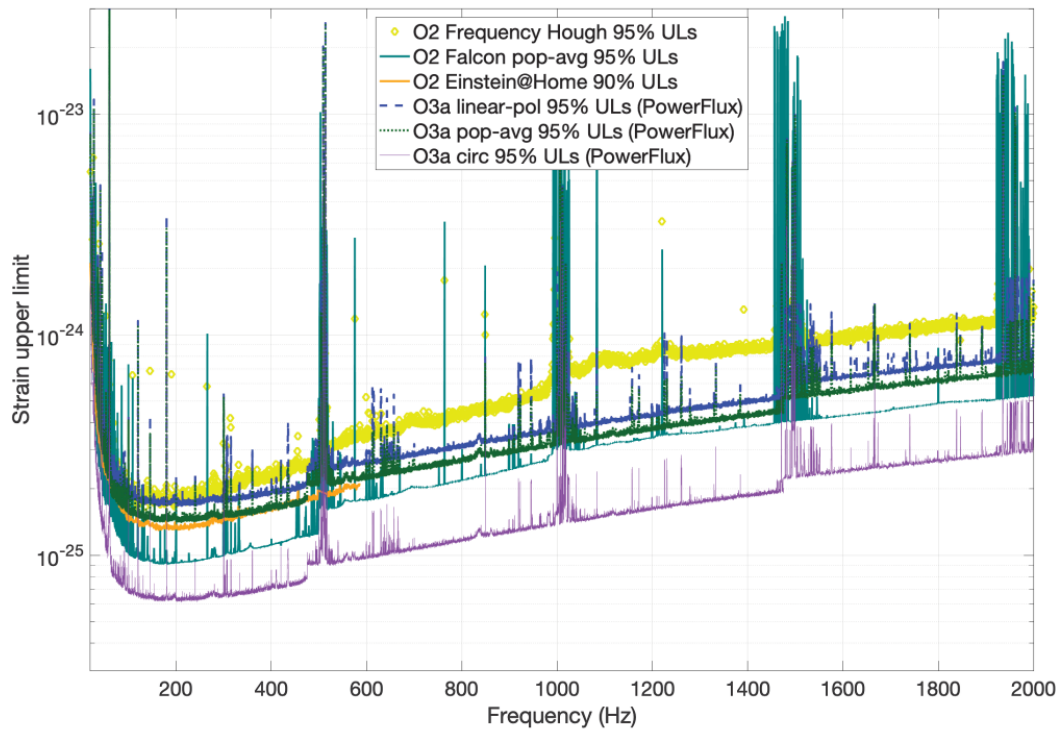
Figure 1.8. The curves represent the detectable strain amplitude h_0 with variable confidence level $(90\% - 95\%)$ from 20 Hz to 2000 Hz. There are reported the early O3a results along with the full O2 ones. The circular polarized (front view of the GW) curve is the optimistic case while the linear polarization (side view) the pessimistic one [27].

Chapter 2

Approaches in the All-sky search

Vast portions of sky and spin-down parameters are involved in order to search for continue wave sources. With a full coherent procedure the computational cost is prohibitive, hence the best strategy is a hierarchical approach. This method, frequently used in the All-sky search, is composed by several individual steps that are performed in sequence. Fig. 2.2 is a good representation of a general hierarchical method: the semi-coherent analysis is applied to the acquired data while a *refined*, i.e. full coherent, analysis is adopted for the (few) surviving candidates.
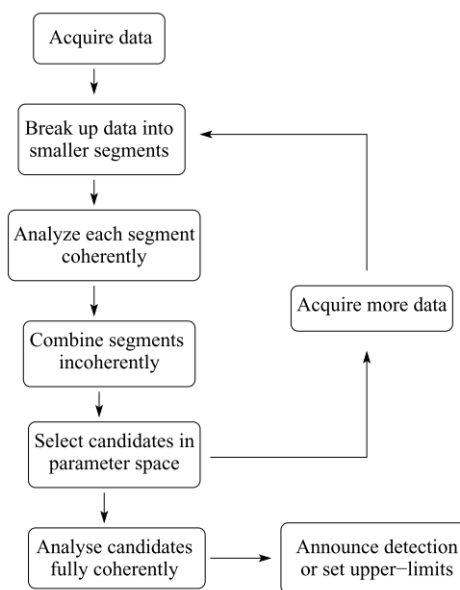
Figure 2.1. A general scheme of hierarchical approach which includes a semi-coherent analysis on the acquired data and then a full coherent analysis on the candidates that have survived all the previous steps [21].

The hierarchical semi-coherent pipeline that was chosen in this *All-sky* search is the **Frequency Hough**.

2.1   Frequency Hough (FH) method

By referring to Fig. 2.2, the semi-coherent Frequency Hough (FH) method is composed by a first *coherent* step that is the *Doppler correction* and a subsequent *incoherent* one, i.e. Hough transform. A detailed scheme of FH is given in Fig. 2.2 whose blocks will be discussed in the following sections.
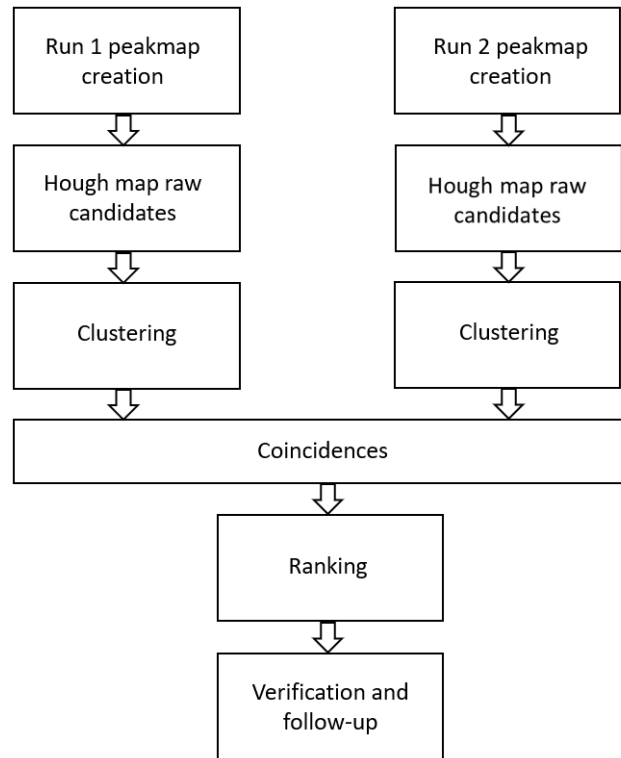

Figure 2.2.   The FH pipeline.   Scheme from   Rome Frequency Hough (FH) All-Sky search (including Follow-up) applied to O3 data page at `https://wiki.ligo.org/CW/RomeFrequencyHoughJUN2021`.

2.1.1   SFDB

The initial step of the FH hierarchical pipeline is the construction of the *Short*[1] *FFT*[2] *DataBase* (SFDB) starting from the time-domain calibrated[3] data acquired from the detector. These data are first divided into chunks each of time duration T_{FFT} called *coherence time*

$$T_{FFT} \sim \frac{1.1 \cdot 10^5}{\sqrt{f_{max}}}[s] \tag{2.1}$$

---

[1]Short respect to the observation time T_{obs} and to the effects of the Doppler shift due to Earth's motion.

[2]It stands for Fast Fourier Transform.

[3]Calibrated implies some procedure applied to the raw data of the detector like time domain disturbances removal.

that is taken accordingly to the maximum value of the frequency interval taken into account with the purpose to contain the Doppler shift of a potential signal within a frequency bin of the FFT which is $\delta f = \frac{1}{T_{FFT}}$. In the current case [10], four intervals and hence four T_{FFT} are chosen: $[10 - 128]$ Hz ($T_{FFT} = 8192$ s), $[128 - 512]$ Hz ($T_{FFT} = 4096$ s) , $[512 - 1024]$ Hz ($T_{FFT} = 2048$ s) and $[1024 - 2048]$ Hz ($T_{FFT} = 1024$ s). For each of the four intervals, the (time-domain) chunk is taken after $\Delta T = T_{FFT}/2$ s the previous one, i.e. it is half interlaced, and windowed with the *flat-top* cosine window: the two choices, together, assure the uncorrelation of the spectrogram data without information loss. The windowing before the conversion of the chunk into its corresponding FFT is crucial: if the period in the segment is not an integer multiple of T_{FFT}, then in the frequency domain a "spectral leakage" will occur and the spectrum will show a spread of the amplitude along other frequencies in addition to the original (true) frequency. By applying the window[4], this unwanted effect is minimized with the flat-top window being the best choice because its resulting spectrum amplitude is closest to the real one [18]. After this operation
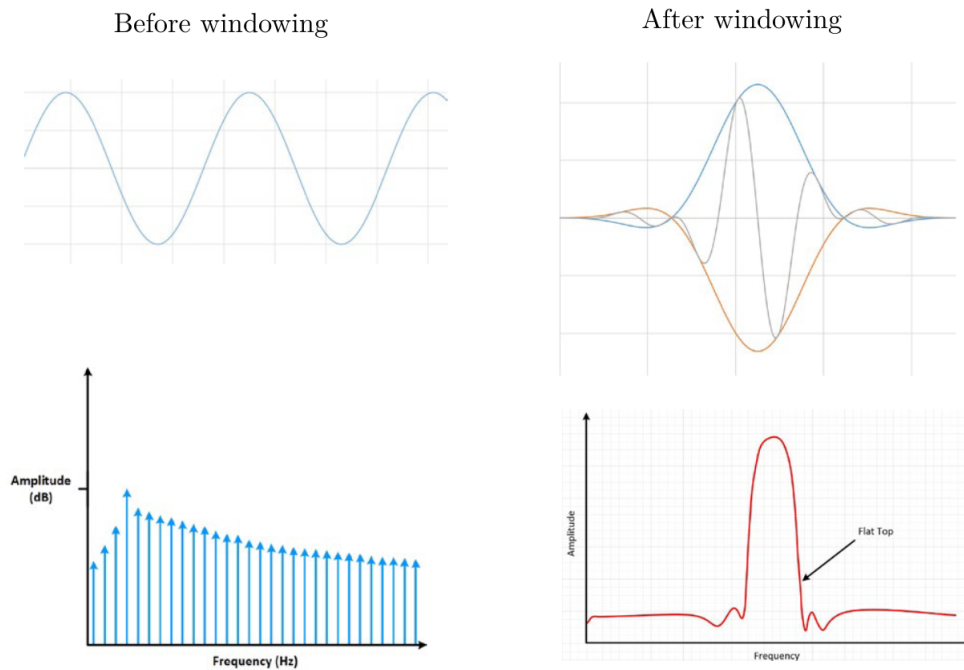

Figure 2.3. The left side of the figure shows the "leakage" problem cited in the text whilst the right one the solution to the problem that is the application of the flat-top window (blue and orange curves) thanks to which the signal (gray) goes toward zero smoothly, avoiding the edge problem. Collage made from figures in [18].

one makes the FFT of the windowed chunk; the collection of the N FFT of the N time-domain chunks produces a (t, f) spectrogram of resolutions (i.e. single bin length) $\delta t = \Delta T$ and $\delta f = \frac{1}{T_{FFT}}$. The single FFT appears then as a "frequency vertical slice" ($0 \leq f \leq f_{max}$) of length ΔT. The four spectrograms are then created

---

[4]With this expression one means that the time domain signal is multiplied with the window function.

B [Hz]	T_{FFT} [s]	δf [Hz]	N_f
1024–2048	1024	$9.7 \cdot 10^{-4}$	$2.09 \cdot 10^6$
512-1024	2048	$4.88 \cdot 10^{-4}$	$2.09 \cdot 10^6$
128-512	4096	$2.44 \cdot 10^{-4}$	$2.09 \cdot 10^6$
10-128	8192	$1.22 \cdot 10^{-4}$	$1.05 \cdot 10^6$

Table 2.1. The table summarizes the four band intervals B with their own T_{FFT}, frequency resolution δf and number of frequency bins N_f [10].

with the side-by-side slices, with an overall number of frequency bins N_f that varies in each interval due to the fact that the resolutions changes with the value of T_{FFT} as shown in Table 2.1. With the particular choice of T_{FFT} and frequency intervals, the last three N_f are the same.

2.1.2 Peakmap

After the creation of the spectrogram from the SFDB, the following step is the construction of the Peakmap which is a collection of peaks in the time-frequency plane. For each of the N FFTs in the SFDB, the periodogram $S_{p;i}(f)$, that is the square modulus of the $i-th$ FFT, and the auto-regressive average spectrum $S_{AR;i}(f)$ are computed, see Fig. 2.4. Their ratio is

$$R(i,j) = \frac{S_{p;i}(f)}{S_{AR;i}(f)} \qquad i = 1, 2, ...N$$

where the index i stands for the FFT taken into account and j for the $j-th$ frequency bin of the $i-th$ FFT. For every (i,j), $R(i,j)$ has to satisfy two conditions: being
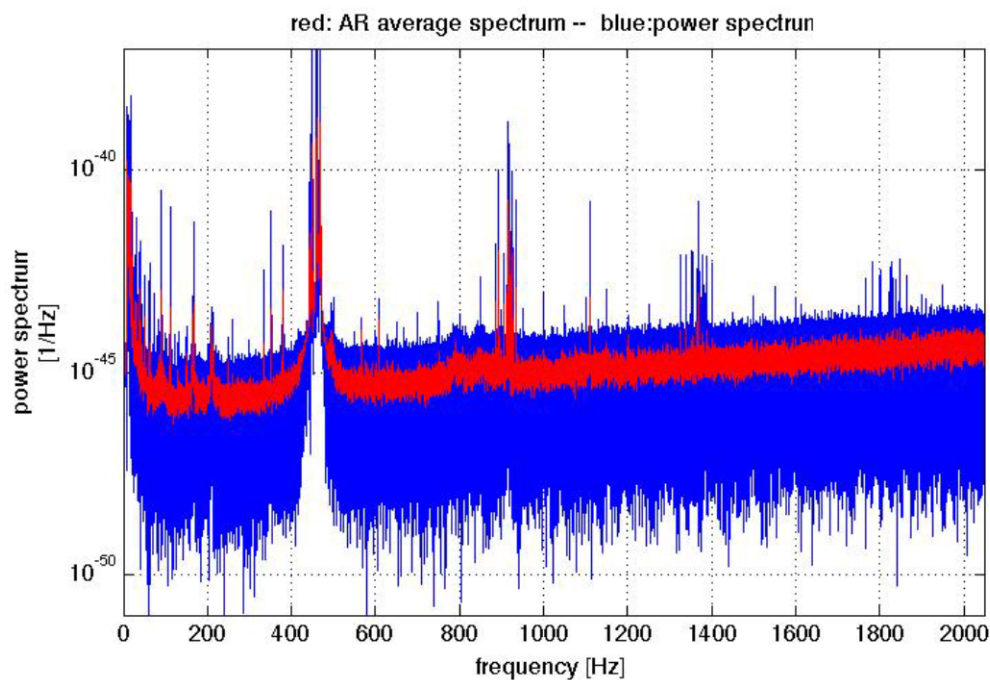
Figure 2.4. A representation of the spectrum (blue) and the average spectrum (red) from VSR4 data (Virgo detector). Image from Rome Frequency Hough review page, https://wiki.ligo.org/pub/CW/RomeFrequencyHough/Peak_maps.pdf.

above a threshold θ_{thr} *and* a local maximum respect to its $(j-1, j+1)$ neighboring bins; every time this happens, the corresponding peak is selected and the surviving bin contributes to the realization of the Peakmap. The choice of the threshold θ_{thr} is critical because it influences the search sensitivity and its computational weight whilst the addition of the local maxima condition gives to the criteria more robustness against disturbances. Fig. 2.5 shows the ratio R and the selected local maxima peaks above the threshold (magenta line).

The probability to select a peak in the case a *noise* is $P(\theta;0) = p_0$ and has the form of

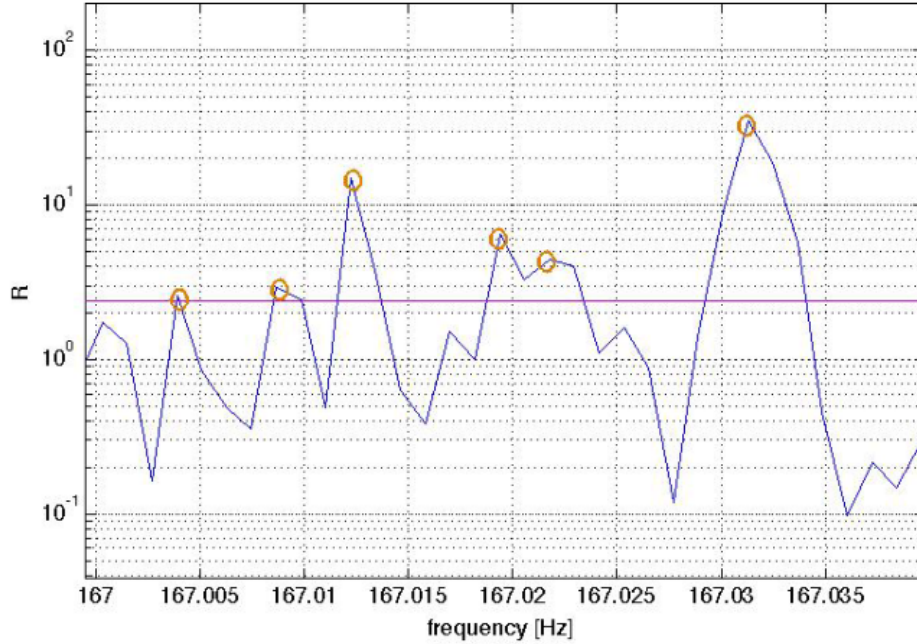$$p_0 = \int_{\theta}^{+\infty} e^{-x}(1 - e^{-x})^2 dx = e^{-\theta} - e^{-2\theta} + \frac{1}{3}e^{-3\theta}$$

Figure 2.5. Focus on a small frequency band for the Ratio R from VSR4 data. The horizontal magenta line represents the threshold θ_{thr} whilst the orange circles are the peaks which are also local maxima which are then going to be selected to form the Peakmap. Image from Rome Frequency Hough review page at `https://wiki.ligo.org/pub/CW/RomeFrequencyHough/Peak_maps.pdf`.

$e^{-x}dx$ is the probability of having a value of $R(i,j)$ in $[x; x+dx]$ and $(1-e^{-x})^2$ that this value is *also* a local maximum. With the same assumptions, for a *signal* of amplitude λ instead of a disturbance that probability $P(\theta_{thr}; \lambda) = p_\lambda$ is

$$p_\lambda \approx p_0 + \frac{\lambda}{2}\theta(e^{-\theta} - e^{-2\theta} + \frac{1}{3}e^{-3\theta})$$

The probability of having m peaks in the Peakmap is binomial with $\mu = N_{tot}p_0$ and $\sigma = \sqrt{N_{tot}p_0(1-p_0)}$ with $N_{tot} = N \cdot N_f$, the total number of bins in the Peakmap. With a sufficient high number of T_{FFT}s, i.e. N, the binomial distribution can be approximated to a Gaussian one [10].

The value of θ_{thr} can be obtained with the maximization of the expectation value of the critical ratio

$$\mu_{CR}(\theta, \lambda) = \frac{N(p_\lambda - p_0)}{\sqrt{Np_0(1-p_0)}}$$

It has been seen that choosing $\theta_{thr} = 2.5$ only produce small sensitivity loss of the search and the local maxima condition avoids the disturbances in the data from being selected because they spread in more than just one bin. Fig. 2.6 shows how an uncorrected[5] Peakmap appears if a real CW signal is present; in this case it is an hardware injection (HI) in the Virgo VSR2 run called *pulsar3* with the

---

[5]The correction regards mainly the Doppler effect.

following characteristics at the reference time[6] t_0 at epoch MJD[7] 52944: frequency $f_0 = 108.8572$ Hz, spin-down $\dot{f}_0 = -1.46 \cdot 10^{-17}$ Hz/s, right ascension $\alpha = 178.37°$, declination $\delta = -33.43°$ and strain amplitude $h_0 = 8.3 \cdot 10^{-24}$.
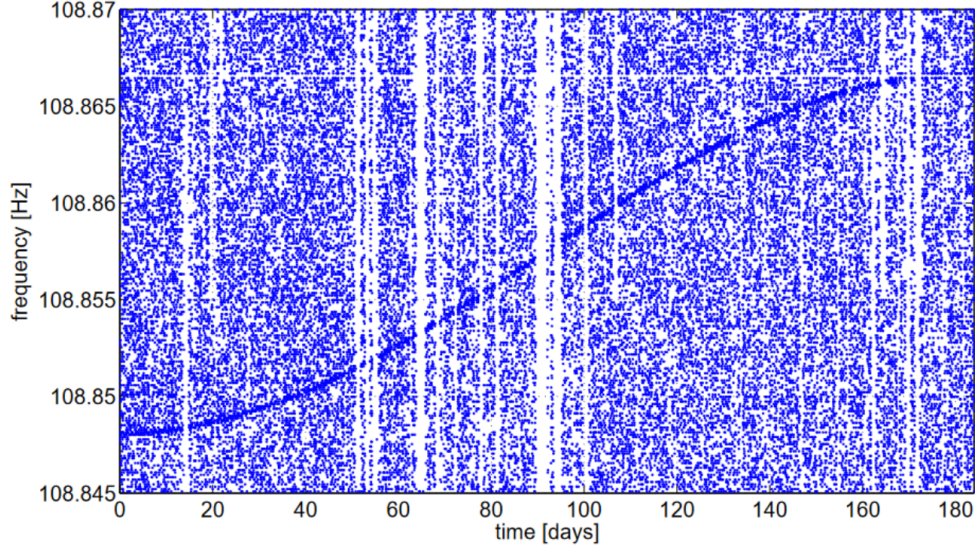

Figure 2.6. The resulting Peakmap from the data in which HI pulsar3 has been injected. The blank spaces that appear in the white background represent the positions of the non-surviving bins of the threshold and local maxima conditions or missing data. The (strong) CW signal varies in frequency due (mainly) to the lack of Doppler correction [10].

Sky grid

The constructed Peakmap has first to be Doppler corrected to be given as an input to the Hough transform step. This correction is applied to *each* sky point of the sky grid and it consists in a simple *shifting* of the Peakmap pixels thanks to the initial request of the Doppler effect to be contained within a single bin. The sky grid is produced as follows. It is taken into account the signal in Eq. 1.44 . If it is satisfied the request $\Delta f_{max} = \delta f$ i.e. the maximum Doppler variation of the source frequency corresponds to a frequency bin of the peak map, one can find the angular resolutions of the sky grid

$$\delta \lambda = \frac{1}{N_D cos\beta} \qquad \qquad \delta \beta = \frac{1}{N_D sin\beta}$$

where the longitude resolution is $\delta \lambda$, the latitude resolution is $\delta \beta$ and N_D

$$N_D = \frac{f_0 \Omega_{orb} R_{orb} T_{FFT}}{c} \qquad (2.2)$$

is the number of frequency bins interested by the Doppler band. The number of sky points in a sky grid of a specific f_0 is equal to

$$N_{sky} \simeq 4\pi K_{sky} N_D^2$$

---

[6]The reference time is a time respect to which the values of the parameters are given.

[7]The Julian Day begins at noon on January 1, 4713 B.C. and the Modified Julian Day is MJD = 240000.5 - JD.

Hence, N_{sky} increases with the source frequency f_0 whilst $\delta\lambda$ and $\delta\beta$ decrease. With this methodology, the sky grid formed is called *optimal*. A different grid in the *sky Hough* is used due to the chance o use fastest computing algorithms and it's called rectangular with a number of points

$$N_{sky} = K_{sky}2\pi^2 N_D^2$$

that has less sensitivity respect to the optimal one [8]. The over-resolution factor K_{sky} enhances the efficiency but also increase the number of artifacts (*false* candidates) and it is set $K_{sky} = 1$. Fig. 2.7 shows the optimal coarse sky grid in ecliptical coordinates for $f_0 = 200$ Hz and $K_{sky} = 1$.
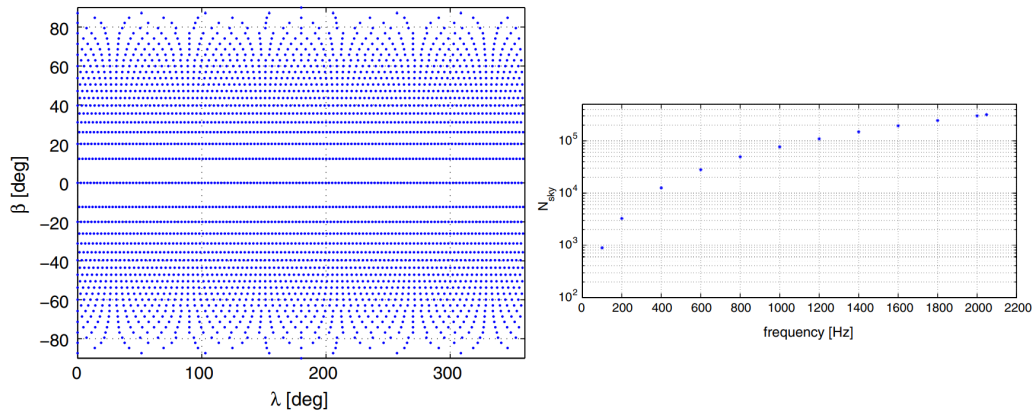

Figure 2.7. On the left: optimal coarse sky grid in ecliptical coordinates for $f_0 = 200$ Hz, $T_{FFT} = 1024$ s and $K_{sky} = 1$. On the right: Number of sky points N_{sky} as a function of the frequency (here $f_{max} = 2048$ hence $T_{FFT} = 1024$ s) [10].

To conclude and summarize: for each point in the sky grid a Doppler correction is computed, hence a single corrected Peakmap is generated and taken as input for the Hough transform that will give a Hough map in return. Therefore, for N_{sky} sky points there will be N_{sky} Doppler corrections, corrected Peakmaps and Hough maps.

2.1.3   Hough transform

The Hough transform is the core of the FH and is a function that provides a linear mapping between the corrected Peakmap and the nominal frequency and spin-down plane, i.e. $(t, f) \rightarrow (f_0, \dot{f}_0)$. The action of the Hough transform can be visualized as follow. Assuming the existence of two manifolds Σ and M, it exists a function $g : \Sigma \rightarrow \mathcal{C}$ that provides a one-to-one association and where Σ is the pulsar parameters plane $(f_0, \dot{f}_0)$, M is the (t, f) plane and the collection of hypersurfaces $\mathcal{C}$ lays in the manifold M. Given a set of observations $\{x_i\}$ in the manifold M of coordinates (t, f), the Hough transform takes each observation from the manifold M and describes a set of points $\mathcal{U}_i$ consistent with x_i. If the collection $\{x_i\}$ comes from a single hypersurface, then the observations belong all to the same source that evolves during time, and it is true that

$$\hat{\mu} \in \cap_i\mathcal{U}_i$$
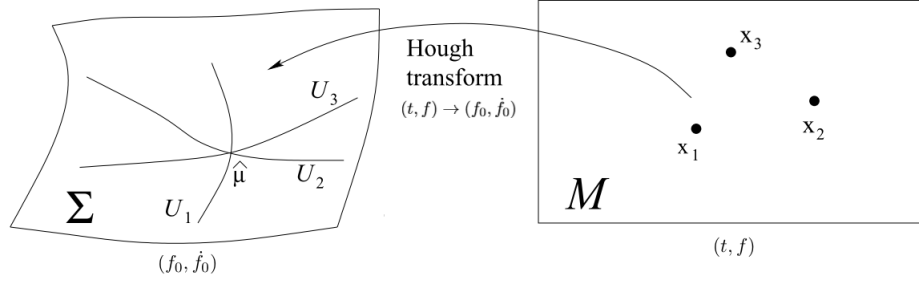
Figure 2.8. The ideal case of infinite resolution. It is reported the action of the Hough transform from the manifold M to Σ [21].

Where $\hat{\mu}$ is the source of coordinates $(f_0, \dot{f}_0)$.

A real case has finite resolution, therefore the manifolds M and Σ are composed by *pixels* of lengths $(\delta t, \delta f)$ and $(\delta f_0, \delta \dot{f}_0)$ respectively. Thus, an observation assumes the form of a pixel and the set of points $\mathcal{U}$ is a slice that touches several pixels in Σ. This mapping has then the form of Fig. 2.9.
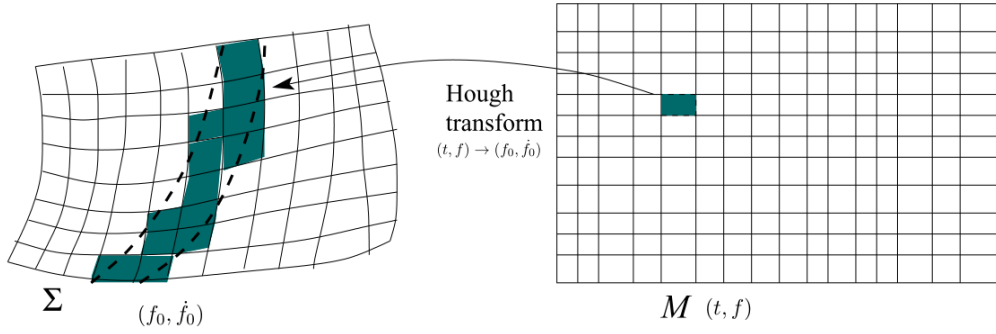

Figure 2.9. The action of the Hough transform from the manifold M to Σ. The shaded pixels in Σ are the ones interested by the dashed $\mathcal{U}_i$ region [21].

Regarding the specific case of the FH pipeline, the manifold M is the Doppler-corrected Peakmap and Σ the Hough map.

Due to the (electromagnetic/gravitational) energy emission, the proper - *true* - frequency of the source decreases with time. For a slowly decreasing frequency, its series expansion can be cut off at first order

$$f(t) = f_0 + \dot{f}_0(t - t_0) + ... \tag{2.3}$$

hence

$$\dot{f}_0 = -\frac{f_0}{t - t_0} + \frac{f}{t - t_0} \tag{2.4}$$

The real situation of finite resolution gives rise to the slice in the Hough map plane (Fig. 2.9) identified by

$$-\frac{f_0}{t - t_0} + \frac{f - \delta f_H/2}{t - t_0} < \dot{f}_0 < -\frac{f_0}{t - t_0} + \frac{f + \delta f_H/2}{t - t_0} \tag{2.5}$$

where $\delta f_H = \frac{\delta f}{K_f}$ is the width of the frequency bin in the Hough maps, from the δf of the Peakmap and the K_f as frequency over-resolution factor. In order to determine whether a source is present in the data or not, each time a slice touches a pixel of coordinates $(f_0, \dot{f}_0)$ the number count of that pixel increases of +1. A first approach is simply

$$n = \sum_{i=1}^{N} n_i$$

which is the final number count in that pixel and where n_i can be 0 or +1. Hence the Hough map is binomial because the pixel *is* or *is not* touched by the slice of Eq. 2.5. In the Hough map, one is interested in the pixel with an high number count n respect to the average and, if in the input plane the reference time t_0 is in the middle of the observation time, the signal of the potential source reduces the slop given by $-\frac{1}{t-t_0}$ in Eq. 2.5. The FH pipeline of this work makes use of the *adaptive* number count that is

$$n = \sum_{i=1}^{N} w_i n_i$$

where w_i are *weights* associated to the $i-th$ pixel. The role of the weights is to take into account non stationary noises and time-varying detector beam pattern functions $F_+, F_\times$. With this implementation, n is not a integer number anymore. The adaptive Hough map of pulsar3 visible in Fig. 2.10 appears as a double cone with high number count around the already known coordinates $f_0 = 108.8572$ Hz, $\dot{f}_0 = -1.46 \cdot 10^{-17}$ Hz/s proving the validity of the *adaptive* Hough transform.

Frequency and spin-down grid

The Hough map is function of the intrinsic source frequency f_0 and its spin-down $\dot{f}_0$. As aforementioned, the standard step of the frequency is $\delta f_H = \delta f / K_f$ in order to reduce the digitalization loss. A good choice for the over-resolution factor K_f is 10 for the coarse grid. This choice increases the number of frequency bins N_f which is equal to

$$N_f = K_f \frac{T_{FFT}}{2\delta t} = \frac{1}{2 \cdot \delta t \cdot \delta f_H}$$

For what concern the spin-down step $\delta \dot{f}$ its definition is

$$\delta \dot{f} = \frac{\delta f}{T_{obs} K_{\dot{f}}}$$

In the current analysis only the first order spin-down is taken into account (see Eq. 2.3): this is acceptable depending on the value of a quantity called *minimum spin-down age* τ_{min} that has an impact on the computational cost of the analysis. Generally, it is equal to

$$\tau_{min} = MIN(\frac{f_0}{\dot{f}_0}) \tag{2.6}$$

while the number of spin-down values of order j $N_{sd}^{(j)}$ is

$$N_{sd}^{(j)} = \frac{T_{FFT}}{\delta t} \left(\frac{T_{obs}}{\tau_{min}} \right)^j$$
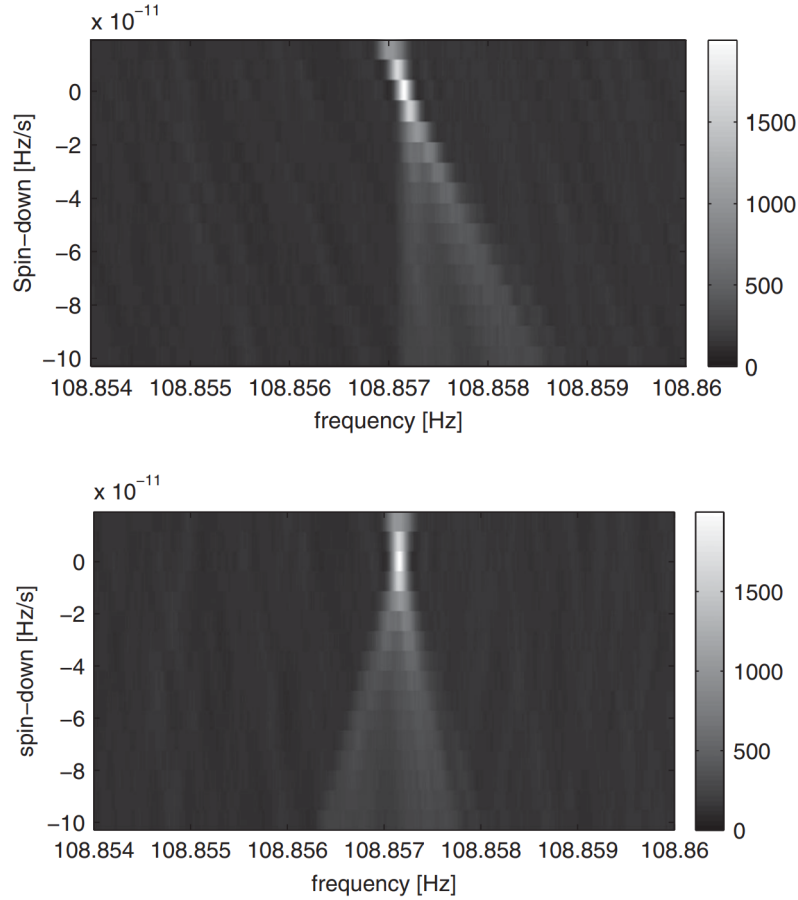
Figure 2.10. Adaptive Hough maps of pulsar3. On top, the double light cone appears sloping. On the bottom, the slope is gone because the reference time t_0 is in the middle of the observation time [10].

In Fig. 2.11 it is provided an example of the values of τ_{min}. If one wants to stop at the first spin-down order as it has been done in Eq. 2.3 then $\tau_{min} = 2100$ yr. With these information, for the *coarse* grid $K_{\dot{f}}$ is set equal to 1 giving an amplitude digitalization loss of $\sim 3.6\%$.

2.1.4 Selection of candidates, clustering and coincidences

After the Hough map has been computed, candidates are selected[8]. Each 1 Hz of the Hough maps is divided into 20 sub-bands (each of 0.05 Hz) from which the candidates with the highest number count n get selected; in most of cases there are taken the strongest *two*. All of this is applied to one detector data, but the purpose is to compare two sets of data from different detectors. Hence, the candidates of the same detector are clustered and then coincidence between clusters occurs. Given two candidates with parameters $\vec{c}_1 = (\lambda_1, \beta_1, f_1, \dot{f}_1)$ and $\vec{c}_2 = (\lambda_2, \beta_2, f_2, \dot{f}_2)$ their

---

[8]For more than one sky location, an equal number of Hough maps will be computed and then for each of the maps, a selection will occur.
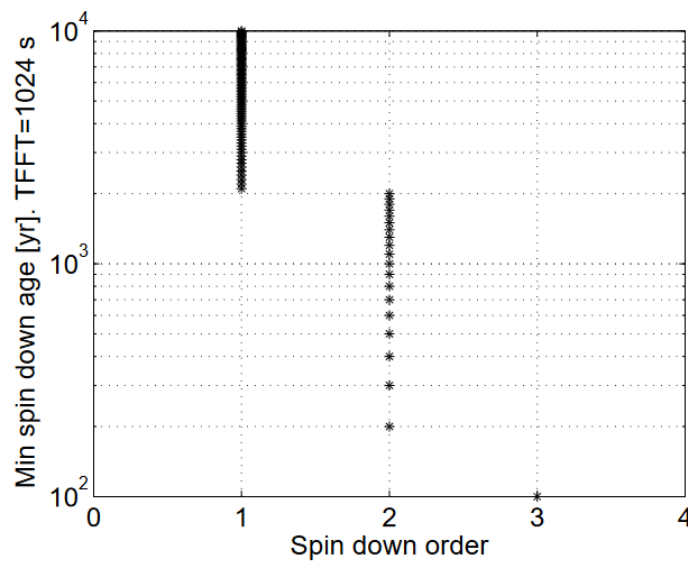
Figure 2.11. An example of the value of τ_{min} needed to adopt the first order spin-down approximation. For $T_{FTT} = 1024$ s ($f_{max} = 2048$ Hz), the minimum value of τ_{min} giving the lowest computational cost is 2100 yr [10].

distance is

$$d = ||\vec{c}_1 - \vec{c}_2|| = \sqrt{k_\lambda^2 + k_\beta^2 + k_f^2 + k_{\dot{f}}^2} \tag{2.7}$$

where $k_\lambda = \frac{|\lambda_2 - \lambda_1|}{\delta\lambda}$. The clusterization of candidates from a single dataset/detector is composed by 4 steps [9]. The **first** step is a preliminar clusterization based on the frequency. Starting from the i candidate ($i = 1, 2, ..., N_{cand}$), it is checked on the $j = i + 1, i + 2, etc...$ candidates that are on the *right* of i the maximum frequency distance imposed. Once this frequency distance is exceeded, the first cluster is "complete" and a new cluster c_i starts with the same request. The **second** step works on the general distance computed with all the parameters of the candidates, Eq 2.7, which is often imposed $d = 2$. This distance is checked only for the *right* j candidates respect to the starting one i. All the candidates that satisfies $d \leq 2$ with the first candidate i belongs to the cluster c_i. What it may happen is that two candidates from two separate clusters can have $d \leq 2$. This is possible because in step two the distance is computed only for the "first" candidate (progenitor) and every candidate on *its* right. If two clusters are taken into account, the one of which has only one element, and this one has $d \leq 2$ from the last element of the first cluster that is on its *left*, then the singleton gets incorporated, **third** step. The **fourth** step is about the record of the numerosity of each cluster. After the clusterization, the clusters of two different dataset go through the coincidences step. Candidates of these different clusters are coincident if $d \leq 3$ one from another. This value has been chosen after studies with simulated signals: it reduces the false alarm probability (the probability to select a candidate that is disturbance) and it is sufficiently robust in the case of a signal with slightly different parameters in the two detectors.

---

[9]This can be found with further details in the Rome Frequency Hough PartTwo review at https://wiki.ligo.org/pub/CW/RomeFrequencyHoughPartTwo/code_rev_clustering.pdf

After this step, coincident candidates go through a ranking procedure. The rank occurs every 0.1 Hz band for the N_{cand} coincidences candidates in it. It is divided into two parts: number count and distance. For what concerns the rank for the number count, the candidates of each dataset are separately ordered in *descending* order (from the one with the highest n to the lowest) and there are ranked with $r_{i,j}$ which is $1/N_{cand}$ for the highest and 1 for the smallest. The index $i = 1, 2$ stands for the detector/dataset and j is the position of the candidate of the i-th dataset. The ranking about the distance is done by ordering the candidates in *ascending* order (hence from the nearest to the farthest). This rank is computed for each pair of candidates and it is called $r_{d,j}$, running over the j candidates of a single dataset, where j is defined before the sorting; for the lowest distance it is $1/N_{cand}$ and for the highest 1. The final rank is a combination of the two discussed above

$$r_j = r_{d,j} \times \prod_{i=1}^{2} r_{i,j}$$

If the j is the highest in a dataset $r_{i,j} = 1/N_{cand}$ and $(1/N_{cand})^2$ if it is for both of the dataset; for the nearest couple $r_{d,j} = 1/N_{cand}$, then $r_j = 1/N_{cand} \times (1/N_{cand} \cdot 1/N_{cand})$. Hence a lower value of r_j implies, for the j candidate, an higher number count and small distance from the other dataset candidate [25].

The last procedure consist in the *Follow-up*, described in [26]. An important step is a consistency test based on the Critical Ratio, a random variable that measures the statistical significance of the number count n of a pixel of the Hough map respect to its expected value in presence of the noise alone.

$$CR = \frac{n - \mu}{\sigma} \tag{2.8}$$

where $\mu = Np_0$ and $\sigma^2 = Np_0(1 - p_0)$. The same discussion made in Section 2.6 is valid here as well: when the number of T_{FFT}s of the Peakmap N is sufficiently large, the binomial probability of having n can be approximated with a Gaussian having the parameters written above. The threshold for taking the coincidences candidates to the next step of the Follow-up is usually set to $CR_{thr} = 5$.

2.2 Band sampled data (BSD)

The Band sampled data (BSD) is a data framework given as new input for an analysis pipeline; it has the advantage of opportunely combine sets of data for a given purpose and easily optimize the choice of the parameters to use in a given search. This flexibility translates into the possibility to increase the sensitivity which makes the difference between a detected or a missed signal. This BSD collection can be used for several types of searches like targeted, directed and All-sky for isolated sources and binary systems. The same framework is well suited to the search of unconventional CW signals like the one for dark matter candidates: namely boson clouds formed around spinning BH or dark-photon dark matter. For what concern the work of this thesis, the BSD database will be applied to the all-sky search for isolated neutron stars.

2.2.1 The construction of the BSD database

The construction of the BSD database starts from the SFDB of an half-overlapped FFTs as the one used in the All-sky CW analysis and discussed in Section 2.1.1.

- (a) From the SFDB a band, for example of 10 Hz it taken;

- (b) This same band is hence extracted and the inverse Fourier transform (IFFT) is computed, bringing the band from frequency domain into time domain.

- (c) It is created the time strain data of the sub-band of the i-th FFT.

- (d) As aforementioned, the FFTs are half-interlaced; in order to remove this effect the first and last quarter of the time domain data are eliminated, keeping only their central part.

This procedure is repeated for all the n-FFTs spanning a one-month data and then the next 10 Hz band is taken into account. At the end, one has a collection of blocks of dimensions "10 Hz/1 month" that is the BSD database with new sampling time of $\frac{1}{\Delta f_{BSD}}$ with $\Delta f_{BSD} = 10$ Hz in this case. This satisfies the Nyquist theorem as will be explained later. The Hz and time lengths are tunable parameters: for example, one could choose to have blocks of "20 Hz/3 months". Hence, the BSD database is composed by data in time domain rather than frequency domain: the coherence time T_{FFT} is not fixed but can be chosen accordingly to the type of source of the search (targeted, directed, all-sky and isolated or binary system) [29].
Fig. 2.12 gives an optimal visualization of the construction technique while Fig. 2.13 of the resulting BSD database.

The analytic signal

The step of IFFT on the sub-sampled FFT identified by the letter (c) in Fig. 2.12 can be further discussed in order to understand its advantage. The time domain data stored in the so called *reduced*-analytic signal format and it is different from the *classical* analytic one. In the original SFDB only the positive part of each FFT is stored, so the *classical* analytic signal requires to add zeros to the frequency part of the FFT before the IFFT is performed, being sampled at $f = 2f_{max}$ of the band as required by the Nyquist theorem. The *reduced* one is still a complex time series with only positive frequency, but it is obtained by discarding the negative and zero component of the classical analytic signal sampled at $f = f_{max}$ [30].
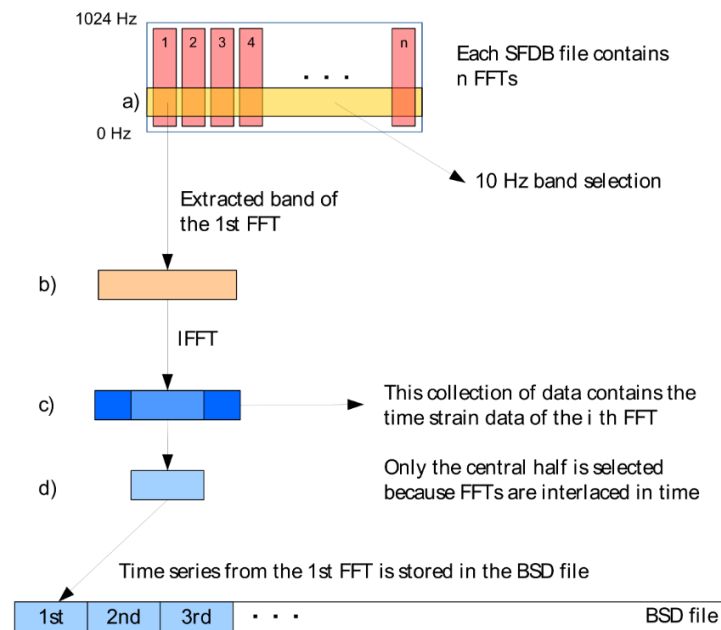
Figure 2.12. The several steps that bring to the single "10 Hz/1 month" block. (a) First, it is chosen the frequency length in Hz and (b) extracted, (10 Hz in the example); (c) the IFFT is performed on this $i - th$ FFT and (d) only the central part is taken. The resulting analytical signal is a single piece of the BSD file that will be filled with all the n-FFTs of the selected 10 Hz band [30].
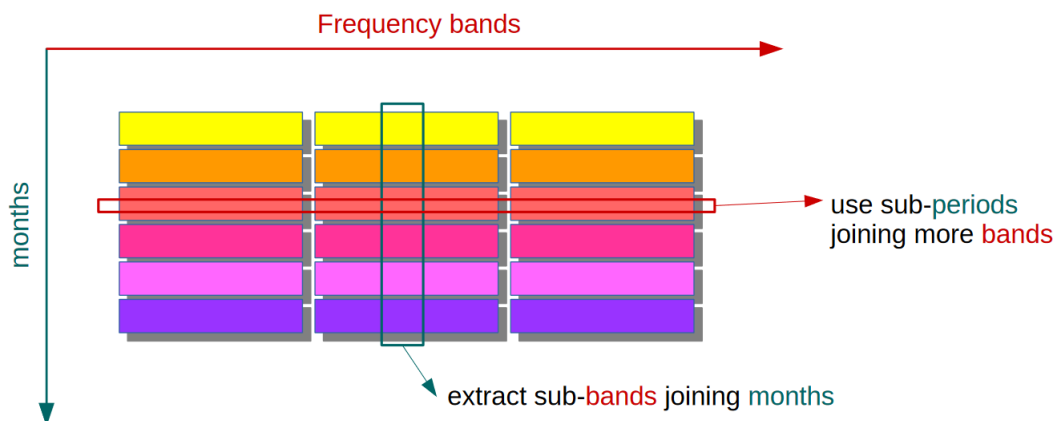

Figure 2.13. The BSD file of Fig. 2.12 is a single block of the BSD database. The extraction of sub-bands from the blocks can be performed respect to frequency or time direction [30].

2.2.2 Advantage respect to the standard four-bands method

As discussed above, the lengths of T_{FFT} can be changed independently and can take any value. This is a great advantage in gaining sensitivity at those frequencies that are penalized in the standard four-bands division. For example, with following four intervals $[10 - 128]$ Hz ($T_{FFT} = 8192$ s), $[128 - 512]$ Hz ($T_{FFT} = 4096$ s), $[512 - 1024]$ Hz ($T_{FFT} = 2048$ s) and $[1024 - 2048]$ Hz ($T_{FFT} = 1024$ s), for the frequency at the begging of each interval the Doppler shift is over-estimated i.e. the frequency bin could be smaller than the one from the standard T_{FFT}. Thanks to the flexibility of the BSD database, the sensitivity improvement is, for a semi-coherent search, $S \propto \frac{1}{\sqrt[4]{T_{FFT}}}$ where $T_{FFT} = \frac{T_{FFT}^{(BSD)}}{T_{FFT}^{(SFDB)}}$ (see [10]).
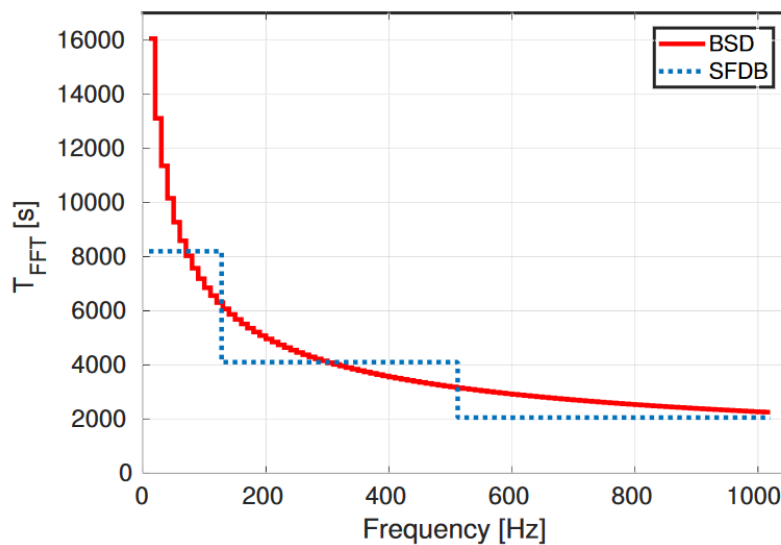

Figure 2.14. The difference between the BSD and the four-bands of SFDB. It is clearly visible the gain in sensitivity of the BSD database specially for the frequencies at the beginning of each of the fours standard bands. For example, for the first SFDB $[10 - 128]$ Hz it is $T_{FFT}^{(SFDB)} = 8192$ s whilst for the $[10 - 20]$ Hz band $T_{FFT}^{(BSD)} \sim 16000$ s [30].

Fig. 2.14 shows the difference between the two methods of interval subdivision in function of the frequency.

Further examples will be provided in Chapter 4.

Chapter 3

A new sensitivity estimation method

In this Chapter I will discuss about a new sensitivity estimation method. The purpose of this first part of my work was to obtain a quicker sensitivity curve starting from the CR of the candidates in the standard four-bands FH pipeline rather than using SIs which implies an higher computational cost of the operation. I firstly tested the validity of the method by using the UL from SIs to make a comparison with several other recalibrated curves in order to understand which one was the most similar to the UL and which one could be accounted as new sensitivity curve, then I proceed to apply this method to produce the upper limits for the all-sky search using O3 data. With this idea, more computational resources can be focused elsewhere as for example in the follow up of the candidates which would imply an higher chance of detection. This method was included in the article **All-sky search for continuous gravitational waves from isolated neutron stars using Advanced LIGO and Advanced Virgo O3 data** of the LIGO-Virgo-KAGRA collaboration in the Section of the *FrequencyHough* pipeline which reports the final results of the search.

3.1   The sensitivity curve

Several definitions of what "a sensitivity curve is" are possible, hence it is relevant to tell precisely which one I am going to refer to in my work.
"The sensitivity, at a given confidence level Γ is defined as the minimum signal amplitude which would produce a candidate in a fraction $\geq \Gamma$ of a large number of repeated experiments." [10]
Γ is the confidence level expressed in % of recovering signals from the injected ones. For example, $\Gamma = 95\%$ means that one will recover the 95% of the signals every time. The probability of selecting a candidate that is above the Hough map threshold i.e. $n > n_{thr}$ is $P_{n>n_{thr}}$ and it is imposed to be equal to Γ

$$P_{n>n_{thr}}(\lambda) = \int_{n_{thr}}^{\infty} P_n(\theta_{thr}; \lambda)dn = \Gamma \tag{3.1}$$

where $P_n(\theta_{thr}; \lambda)$ is the probability of having a signal of amplitude λ and above the peakmap threshold θ_{thr} to have a n count number in a given pixel. Here it is

assumed in its Gaussian approximation to the binomial distribution

$$P_n(\theta_{thr}; \lambda) = \frac{1}{\sqrt{2\pi\sigma^2}} e^{-\frac{(n-\mu)^2}{2\sigma^2}} \qquad \mu = N\eta \qquad \sigma^2 = N\eta(1-\eta)$$

where $\eta = p_0$ in absence of signal and $\eta = p_\lambda$ if a signal is present. Thanks to this approximation and considering the case of small signals, one is able to compute the minimum detectable spectral amplitude λ_{min} which is

$$\lambda_{min} \approx \frac{2}{\theta_{thr}} \sqrt{\frac{p_0(1-p_0)}{Np_1^2}} \left(CR_{thr} - \sqrt{\mathrm{ercf}(2\Gamma)} \right) = \frac{\Lambda_1}{\sqrt{N}} \tag{3.2}$$

where $p_1 = e^{-\theta_{thr}} - e^{-2\theta_{thr}} + e^{-3\theta_{thr}}$ and N is the number of FFTs. The quantity I recalibrated is the minimum detectable strain amplitude $h_{0,min}$, hence some further steps need to be done.
The relation between λ and $h(t)$ is

$$\lambda = \frac{4|\tilde{h}(f)|^2}{T_{FFT}S_n(f)} \tag{3.3}$$

where $\tilde{h}(f)$ is the Fourier Tranform (FT) of $h(t)$ and S_n the detector uni-lateral noise spectral density. The GW signal in a detector takes the form

$$h(t) = F_+ h_{0+}\cos(\phi(t)) + F_\times h_{0\times}\sin(\phi(t)) \tag{3.4}$$

where $\phi(t)$ is the phase of the GW $phi(t) = \int_{t_0}^t \pi f_{GW} dt$, h_{0+} and $h_{0\times}$ the two polarizations $h_{0+} = h_0\frac{1+\cos^2\iota}{2}$ and $h_{0\times} = h_0\cos\iota$ with ι as the angle between the rotation axis of the source and the line of sight , and F_+, $F_\times$ are the beam-pattern functions. The purpose is to compute the FT of $h(t)$ and substitute it in Eq. 3.3. Regarding the cosine and sine function for a frequency f_0, their FT are

$$Y_1(f) = \frac{\delta(f - f_0) + \delta(f + f_0)}{2}$$

$$Y_2(f) = -j\frac{\delta(f - f_0) + \delta(f + f_0)}{2}$$

Thanks to the request formulated for T_{FFT} to have the Doppler shift of the frequency within one bin, (Section 2.1.1), the signal frequency can be accounted as constant. For a finite length signal, the FFT is the convolution of the FT of the signal and a rectangular window of length T_{FFT} i.e.

$$Z(f) = \int_{-\infty}^{+\infty} Y(f') \cdot \frac{\sin\pi(f - f')T_{FFT}}{\pi(f - f')} df' \tag{3.5}$$

Referring to Eq. 3.4, the FT of the cosine part $\cos\phi(t)$ for a frequency bin f_k is

$$Z_1 = \frac{h_0}{2} \frac{\sin\pi(f - f_k)T_{FFT}}{\pi(f - f_k)}$$

while for the sine $\sin\phi(t)$

$$Z_2 = -j\frac{h_0}{2} \frac{\sin\pi(f - f_k)T_{FFT}}{\pi(f - f_k)}$$

Hence, the FT $\tilde{h}(f)$ of $h(t)$ is

$$\tilde{h}(f) \approx T_{FFT} \frac{(F_+ A_+ - jF_\times A_\times)^2}{2} \frac{h_0}{2} \frac{sin\pi(f - f_k)T_{FFT}}{\pi(f - f_k)T_{FFT}} \tag{3.6}$$

Making the square modulus of $\tilde{h}(f)$ and averaging all the quantities,

$$\begin{cases} < F_+^2 >_{\alpha,\delta,\psi} = < F_\times^2 >_{\alpha,\delta,\psi} = \frac{1}{5}, & < F_+ \cdot F_\times >_{\alpha,\delta,\psi} = 0 \\ < A_+^2 + A_\times^2 >_{cos\iota} = \frac{4}{5} \\ \frac{1}{\delta f} \int_{f_k - \frac{\delta f}{2}}^{f_k + \frac{\delta f}{2}} \left(\frac{sin\pi(f - f_k)T_{FFT}}{\pi(f - f_k)T_{FFT}} \right)^2 df = \frac{2.4308}{\pi} \end{cases}$$

the Eq. 3.3 has then the explicit form of

$$< \lambda >_{\alpha,\delta,\psi} \approx \frac{4h_0^2}{S_n(f)} \frac{2.4308}{25\pi} T_{FFT} \tag{3.7}$$

By equating Eqs. 3.2 and 3.7 one obtains the minimum detectable strain amplitude

$$h_0 \approx \frac{4.02}{\theta_{thr}^{1/2}} \left(\frac{p_0(1 - p_0)}{p_1^2} \right)^{1/4} \frac{1}{N^{1/4}} \sqrt{\frac{S_n(f)}{T_{FFT}}} \sqrt{CR_{thr} - \sqrt{2}\,\text{ercf}(2\Gamma)} \tag{3.8}$$

This equation can be generalized noticing that it composed by three main factors: $h_0(S_n, CR) = A(\theta)B(N, S_n)C(CR)$. $A(\theta)$ contains only constants values once the θ_{thr} is fixed for the search[1], therefore it isn't directly included in the h_0 expression; $B(N, S_n)$ can be different for the run and for the detectors, indeed N is linked to the observation time ($T_{obs} = NT_{FFT}$) and S_n is different for each of the two run O2, O3 and, considering the same run, can be higher for the less sensitive detector; $C(CR)$ depends on the Critical ratio chosen, in particular if $CR = CR_{thr}$ the resulting h_0 is the minimum detectable strain amplitude for a given run and detector, also known as *sensitivity*. If $CR = CR_{max}$, then h_0 is more representative of the *Upper limit*, i.e. the maximum detectable strain. Fig. 3.1 shows the two sensitivity curves for both the LIGO detectors (Hanford and Livingston) for O2 (red) and O3 (blue) with S_n for its own detector/run.

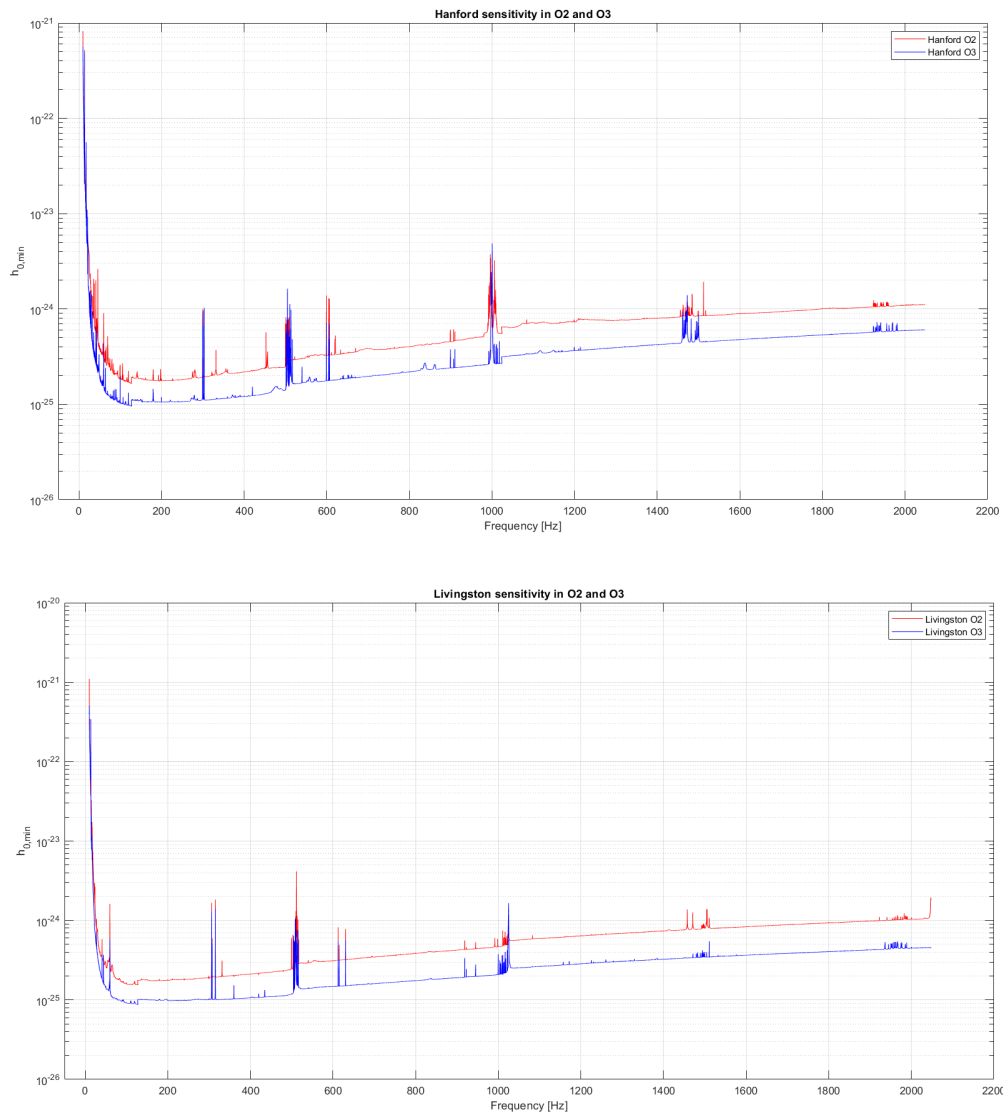[1]θ_{thr} is the same for O2, O3 and both the detectors.

Figure 3.1. The sensitivity curves for the two LIGO detectors Hanford and Livingston for the second and third run called O2 (red) and O3 (blue), respectively.

3.2 On the validity of the FH sensitivity formula

In this part of the work I used the standard four-bands division of the *FrequencyHough* pipeline as reported in Table 3.1 in a spin-down range of $[-1 \cdot 10^{-8}; 1 \cdot 10^{-9}]$ Hz/s. As already discussed in Section 2.1.4 the Hough map are selected 20 candidates per Hz and Sky position with a maximum number of 40 candidates (if there are selected second strongest ones too) for each detector. In the *Ranking* step, the number of the candidates is reduced to 2 for each 1/4 sub-interval of the full spin-down range written above, resulting in a total number of 8 candidates every 0.1 Hz. The last choice consists in the selection of the strongest candidate in each 1 Hz band which will be subjected to the *Follow-up*. The detailed scheme of the FH pipeline used in

B [Hz]	T_{FFT} [s]
1024-2048	1024
512-1024	2048
128-512	4096
10-128	8192

Table 3.1. The table summarizes the four band intervals B with their own T_{FFT}.

given in Fig. 2.2
The candidates I started with are the surviving ones from the *Ranking* step.
As first purpose of this Chapter, I will show the results of the recalibrated sensitivity respect to the Upper limit (UL) curve obtained from SIs of the observation run called O2; while in the second part I will apply this validated method to define new UL and sensitivity curves for the run O3 without the use of SIs. The UL curve which I am referring to is obtained by injecting in each 1 Hz several sets of signals (SIs) with fixed amplitude and random parameters generated in the time domain and then converted in FFTs. After this first step, a specific function is called to perform an analysis in which the candidates are selected, then another one finds the coincidences and a third one ranks the candidates.
In order to obtain these plethora of curves, I will make use of Eq. 3.8 that here takes the precise form of

$$h_{0,rec}^{det,run} = h_{0,min}^{det,run} \sqrt{\frac{CR_{measured} - \sqrt{2}\ \mathrm{ercf}(2\Gamma)}{CR_{thr} - \sqrt{2}\ \mathrm{ercf}(2\Gamma)}} \tag{3.9}$$

where $h_{0,min}$ is the one of Eq. 3.8, det is the detector (Livingston or Hanford), $CR_{measured}$ is the Critical ratio, in each sub-interval of frequency, which satisfies some requests (this will explained in detail in the next Section) from the O2 and O3; $CR_{thr} = 5$ is the one used to compute $h_{0,min}$ with $\Gamma = 95\%$, Eq. 3.8. For $CR_{measured}$ in O3, it was set a minimum CR $CR_{thr} = 3$ in $[10 - 128]$ Hz and $CR_{thr} = 5$ in $[128 - 2048]$ Hz for both detectors.
h_0 depends also on the detector spectral density S_n - which changes from O2 to O3 and for each detector - therefore, following Eq. 3.8, here I recalibrated for CR and S_n.

3.2.1   Testing the new sensitivity formula with O2 data

Starting from Eq. 3.8, in the code I work with the parameter CR and S_n. This brings to Eq. 3.9 in which I take the CR-depending factor and divide it by $1/\sqrt{CR_{measured} - \sqrt{2}\ \mathrm{ercf}(2\Gamma)}$, producing different curves according to what CR takes the place of $CR_{measured}$. Three cases are possible: CR_{max}, CR_{min} and CR_{mean} of each sub-interval (0.1 Hz or 1 Hz) of the full frequency range $[10; 2048]$ Hz. After having computed this for both the detectors, their sensitivity gets recalibrated with the three CR possibilities. For example, for LIGO Hanford in the case of CR_{max} it is

$\vdots$

```
sens_combined(:,4)=sens_temp(:,2).*sqrt(CRmeas-AA)/sqrt(CRUSED-AA);
```
$\vdots$

where `sens_temp(:,2)` is the input the sensitivity of LH, `CRmeas=CR_min_H`, `CRUSED=5` and `AA=-`$\sqrt{2}ercf^{-1}(2\Gamma)$.
The next step is the extraction of the max, min and mean of $h_{0,rec}^{det}$ amongst the detectors $det = LL, LH$ from the ones just computed. These final recalibrated sensitivities take the name from the combination of CR and sensitivity that have been chosen. In the case of selection of the best sensitivity value among the two computed with CR_{max} (Livingston and Hanford) it is $min(h_{0,rec}^{det}(CR_{max}))$. Further details on the algorithm are provided in Appendix A.

Fig. 3.2 shows the full frequency range $[10; 2048]$ Hz of the four curves that have been selected: the UL with SIs is represented by the red curve, whilst the blue, magenta and the black ones are the recalibrated ones. The blue curve is $max(h_{0,rec}^{det}(CR_{max}))$ and it is the most conservative choice because it is composed by the worst sensitivity amongst the ones of LIGO Hanford and LIGO Livingston obtained with the highest CR of the 1 Hz interval (CR_{max}). A less conservative one is the magenta curve, i.e. $min(h_{0,rec}^{det}(CR_{max}))$, due to the choice to take the best sensitivity instead. The black curve, i.e. $max(h_{0,rec}^{det}(CR_{min}))$, is the result of the worst sensitivity between the two recalibrated with the lowest CR of the interval ($minCR$).
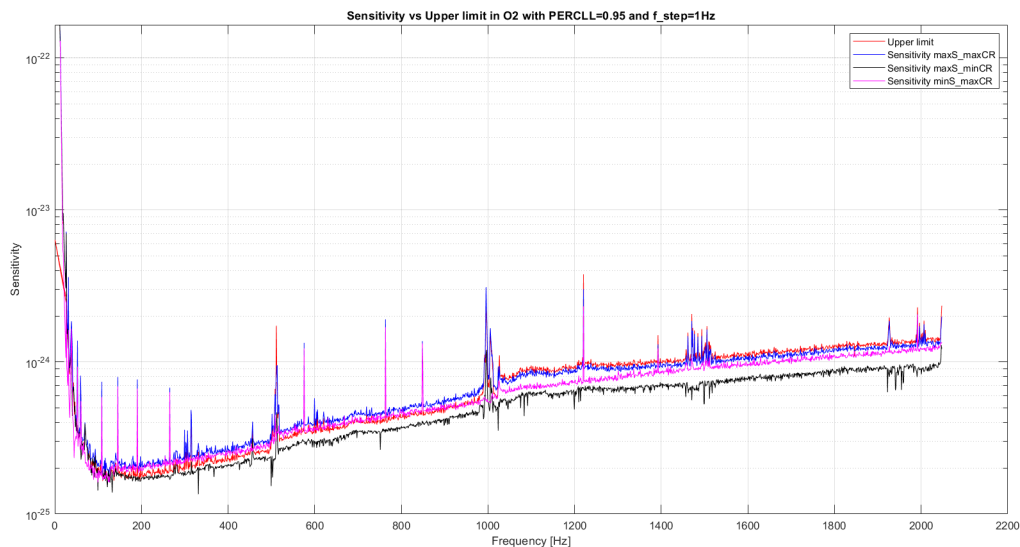

Figure 3.2. A full view of the three recalibrated and the UL curves. The formers are in blue i.e $max(h_{0,rec}^{det}(CR_{max}))$, magenta i.e. $min(h_{0,rec}^{det}(CR_{max}))$, and black i.e. $max(h_{0,rec}^{det}(CR_{min}))$ while the latter is in red.

Several zooms of peaks are reported in the following figures in order to show the behaviours of the three recalibrated curves. It can been seen how in the most conservative approach (blue curve) the sensitivity lays over the UL curve whilst correctly following the peaks. Concerning the last interval of the four bands subdivision $[1024 - 2048]$ Hz, the UL has not been interested by an adequate number

of SIs, therefore it has a wider uncertainty about the value of the curve: its position is switched with the blue curve, indeed, whilst the peaks are still followed in an appropriate way by the most conservative approach. This last observation is well illustrated in Fig. 3.4, Fig. 3.5 and Fig. 3.6.
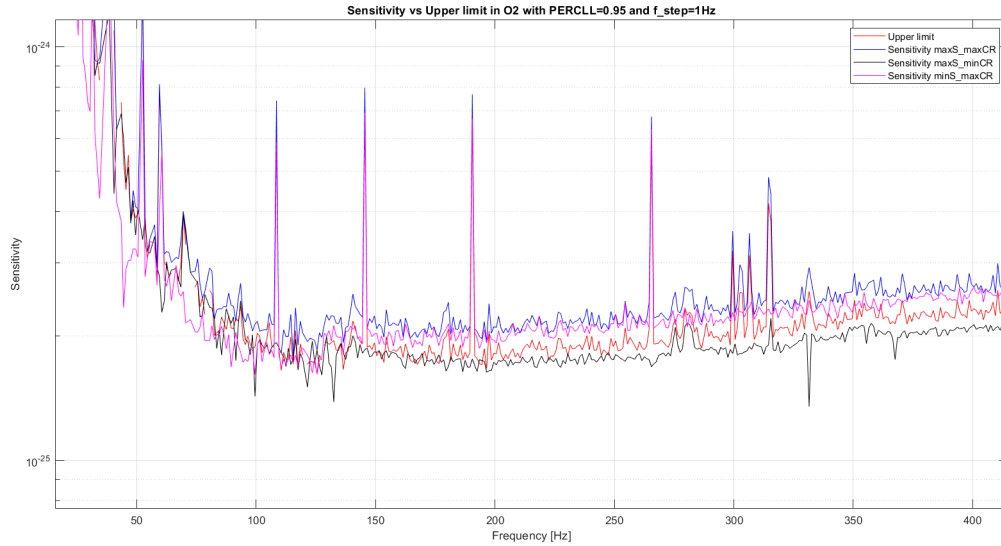

Figure 3.3. The four curves in the first two frequency intervals $[10; 128]$ Hz and $[128; 512]$ Hz. The most conservative approach (blue curve) lays on top of magenta and red curve while the black one is at the bottom.
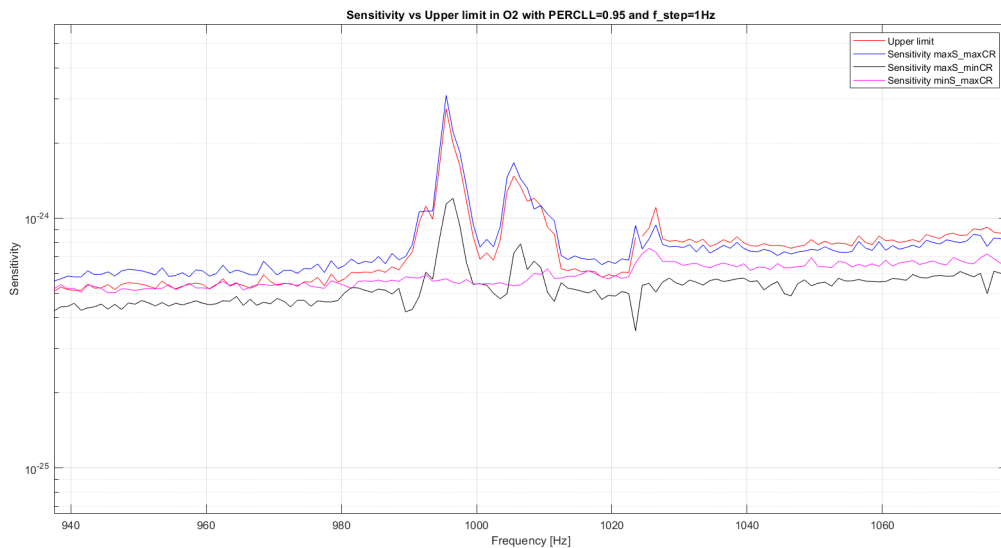
Figure 3.4. Focus in the last part of the third frequency interval $[512 - 1024]$ Hz and the beginning of the fourth one $[1024 - 2048]$ Hz that shows the switch between the blue and red curves due to the lack of adequate number of SIs for the UL in the last interval.
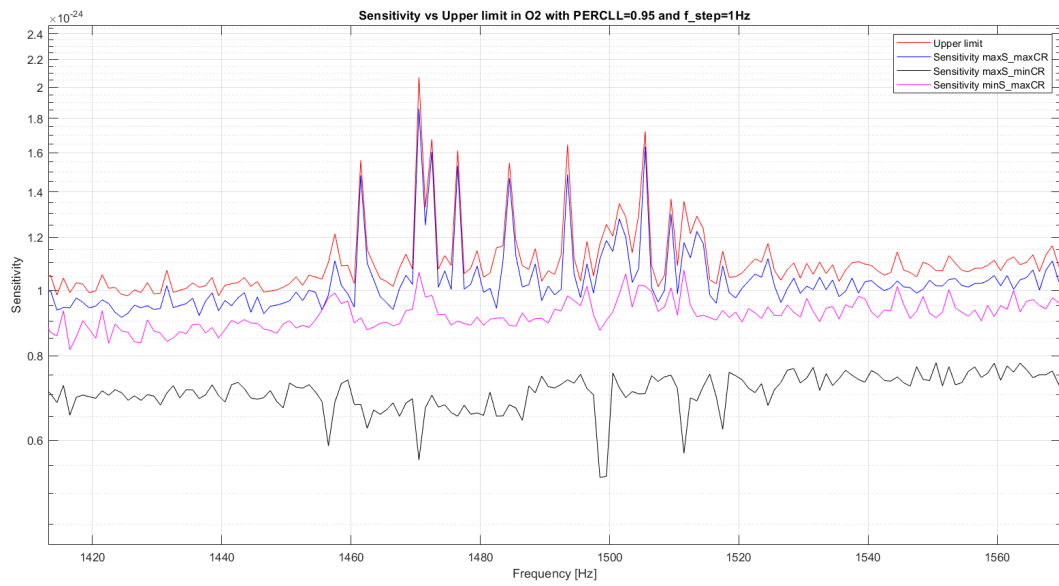
Figure 3.5. Further focus of the curves. The switch occurred in the third frequency interval still persists in the fourth.
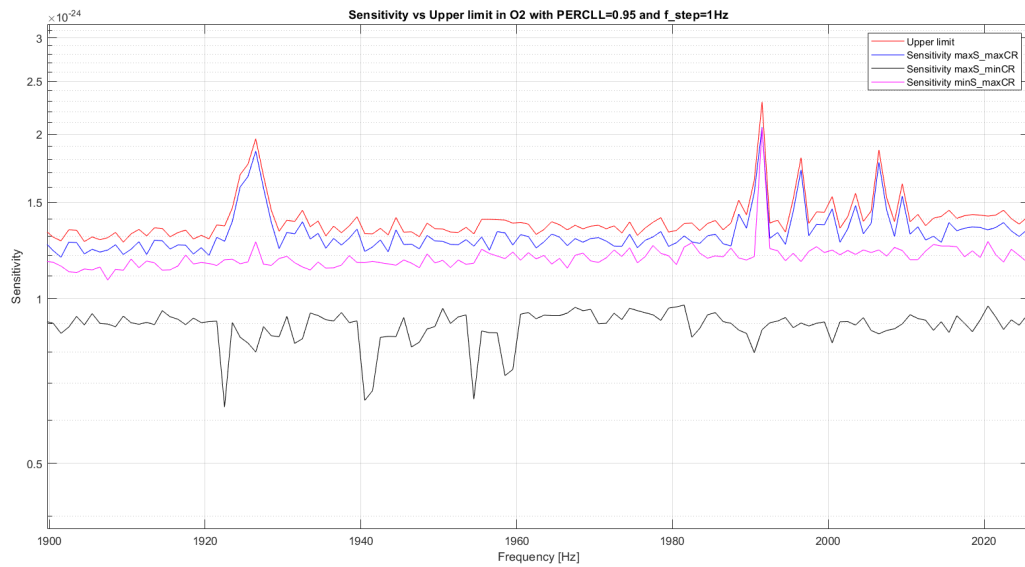

Figure 3.6. A last zoom of the recalibrated and UL curves. The blue one follows the UL curves at the best whilst the magenta one doesn't have the same peak amplitude in several cases.

The magenta curve, while following most of the UL peaks, doesn't have the same peak amplitude making it the second best conservative curve taken from CR_{max}. For what concern the black curve, it lays on the bottom of the two recalibrated ones and the UL curve hence our inferior limit. Its peaks are often upside-down (Fig. 3.5) but not always in correspondence (Fig. 3.6) of the UL ones. This happens due to the definition of the CR itself. Recalling Eq. 2.8, in the frequencies interested

by the noise peaks, the values of μ and σ grow; this could brings μ to be higher of the number count n, returning a negative CR. By taking the worst sensibility from CR_{min}, the reversed peaks are enhanced. If CR is not negative, it is anyway reduced and the resulting worst curve doesn't show evident peaks.

In conclusion, the UL lays between the three displayed recalibrated curves. If one prefers to remain conservative, then the blue curve of Fig. 3.2 assumes the role of the new UL, making the discussed method a new path to obtain the UL curve without spending computational power in the SIs analysis. Fig. 3.7 represents the error in % between the $max(h_{0,rec}^{det}(CR_{max}))$ curve and the original UL; this value is always under 20% with some negative peaks due to disturbances.
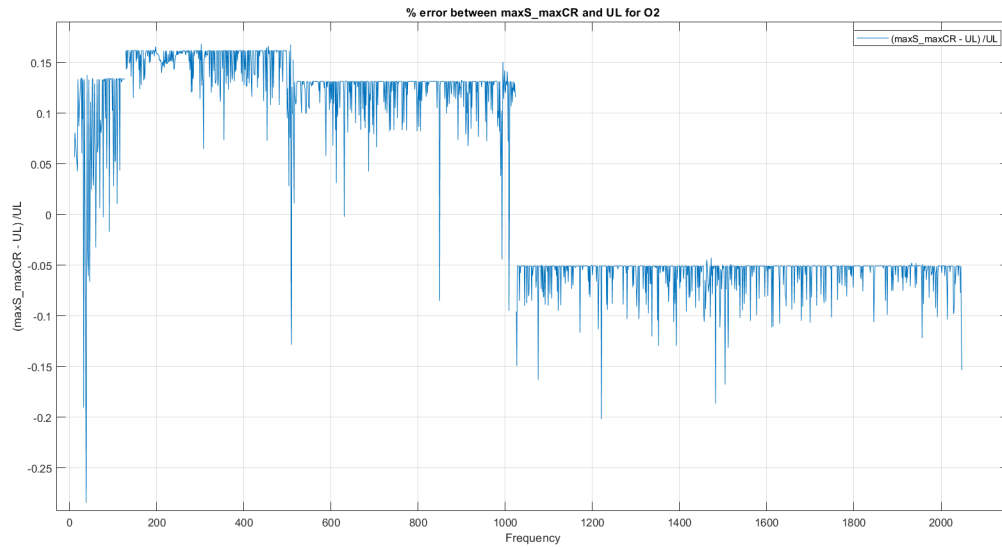

Figure 3.7. Error in % between $max(h_{0,rec}^{det}(CR_{max}))$ i.e. the alternative UL, and UL from SIs. The switch at 1024 Hz discussed in the text appears in this plot too and it is visible due to the persistence in having negative values of the % error.

These are the results with a step frequency of 1 Hz, but smaller steps can be used to have an even more accurate recalibrated sensitivity curve.

3.3 Application of the new method to O3 data

A slightly change respect to O2 is the preliminary threshold concerning the CR. For O2 there were followed every candidated without any threshold on CR, but for O3 it depends on the frequency interval: CR=3 for $[10 - 128]$ Hz and CR=5 for $[128 - 2048]$ Hz. This choice is due to the minimum CR followed during the *Follow-up* step; it would be pointless to select a candidate knowing in advance that it is going to be discarded later.

After having proved that $max(h_{0,rec}^{det}(CR_{max}))$ and $max(h_{0,rec}^{det}(CR_{min}))$ define the interval in which the UL lays and having defined their new roles, the first interesting result to show in this Section is a comparison between O2 and O3 with these exact same two curves, Fig. 3.8. Here are reported the two selected ones of O2 and the four curves of O3 for the two different values of the frequency step in which is done the CR selection.
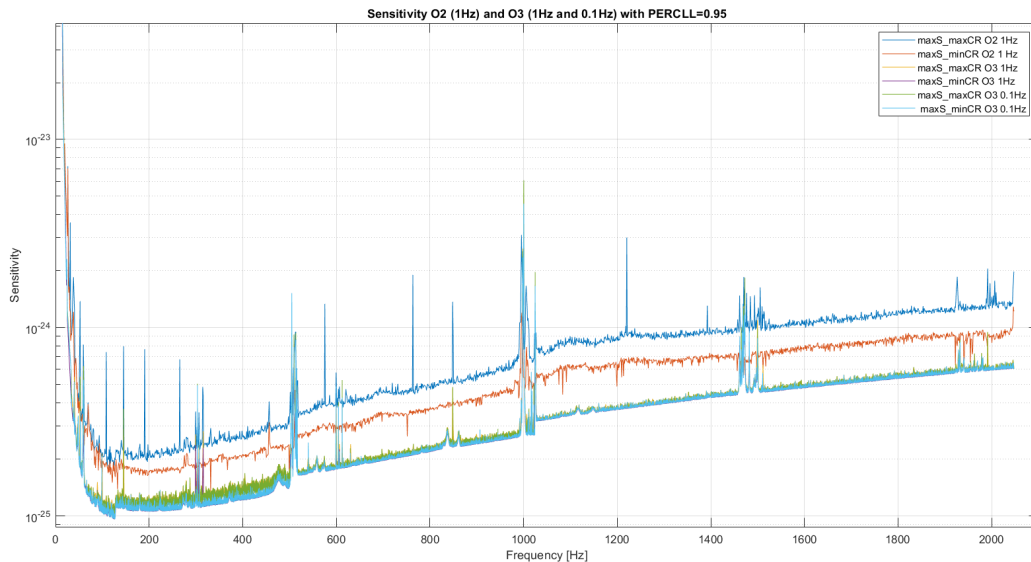

Figure 3.8. In this plot there are shown six recalibrated curves for $max(h_{0,rec}^{det}(CR_{max}))$ and $max(h_{0,rec}^{det}(CR_{min}))$. For O2 the frequency step is 1 Hz (blue and red curves) whilst for O3 it is 1 Hz and 0.1 Hz (orange, purple and green, cyan respectively).

In Fig. 3.9 it is provided a first zoom in frequency to focus on the lowest sensitivity values.
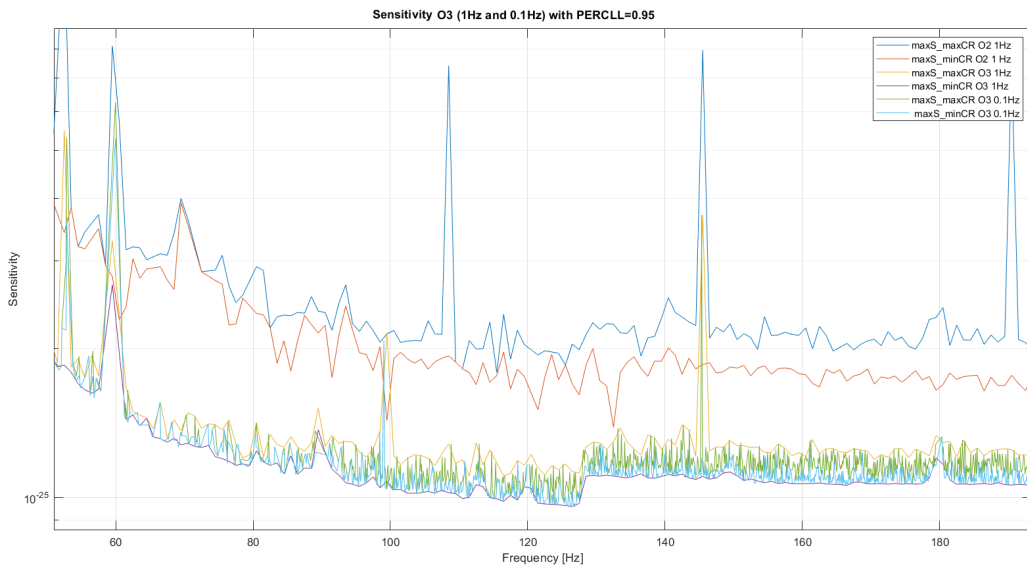
Figure 3.9. Focus on the frequency interval in which the lowest values of the sensitivity are reached.

By following the same approach and conclusion of the previous Section, O3 curves $max(h_{0,rec}^{det}(CR_{max}))$ for 1 and 0.1 Hz are the Upper limits of their own frequency step.

A further focus on just O3 curves is useful to show the behaviour around the peaks. As example, Fig. 3.10 follows the curves in a small frequency sub-interval of $[512 - 1024]$ Hz. As expected, both of the 1 Hz and 0.1 Hz most conservative curves i.e. $max(h_{0,rec}^{det}(CR_{max}))$ show a peak whereas the other two $max(h_{0,rec}^{det}(CR_{min}))$ don't. Hence, the UL recovered from SIs would have a peak around the same frequency as shown in Section 3.2.1 with O2.

As mentioned at the beginning of this Chapter, the work I'm presenting here has brought a little contribution to the non-yet-published article **All-sky search for continuous gravitational waves from isolated neutron stars using Advanced LIGO and Advanced Virgo O3 data** of the LIGO-Virgo-KAGRA collaboration. In this article it is included the approved result of Fig. 3.11 that concerns the $max(h_{0,rec}^{det}(CR_{max}))$ and $max(h_{0,rec}^{det}(CR_{min}))$ curves with frequency step of 1 Hz. Here, the $max(h_{0,rec}^{det}(CR_{max}))$ curve (in yellow) takes the name of Upper limit while the $max(h_{0,rec}^{det}(CR_{min}))$ (in purple) is the new sensitivity, i.e. the lowest value that can be recovered - hence detected - from the data every 1 Hz.

On the other hand, while they could have been even more accurate results, the two curves with frequency step of 0.1 Hz cannot be adequately discriminated from each other, Fig. 3.12, therefore it's safer to use the 1 Hz resolution for the definition of the new UL and sensitivity. In the case of SIs every 0.1 Hz, the comparison would surely have had a better outcome.
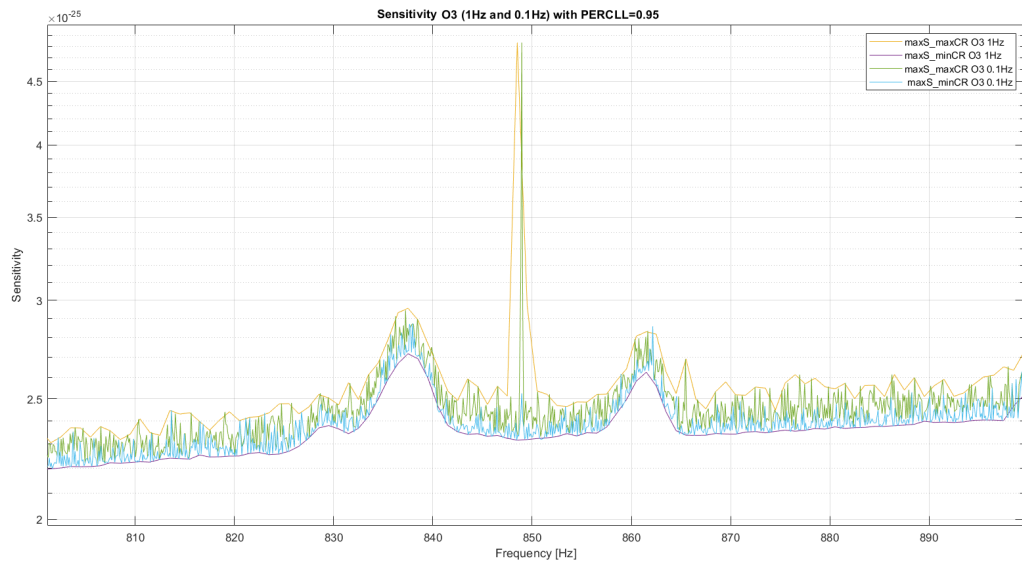
Figure 3.10. The behaviour of the curves satisfies the expectations that are based on the result obtained with the UL for O2, especially $max(h_{0,rec}^{det}(CR_{max}))$ for what concern the peaks.
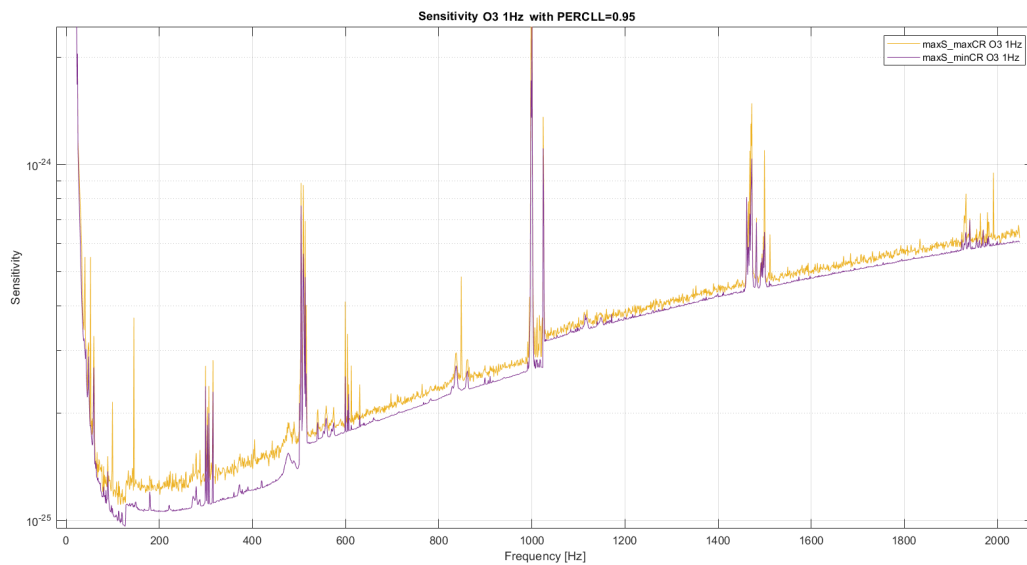

Figure 3.11. The two approved curves for O3 and the frequency step of 1 Hz. The most conservative one, in yellow, has been defined the new UL for O3 whilst the purple curve is the new sensitivity.
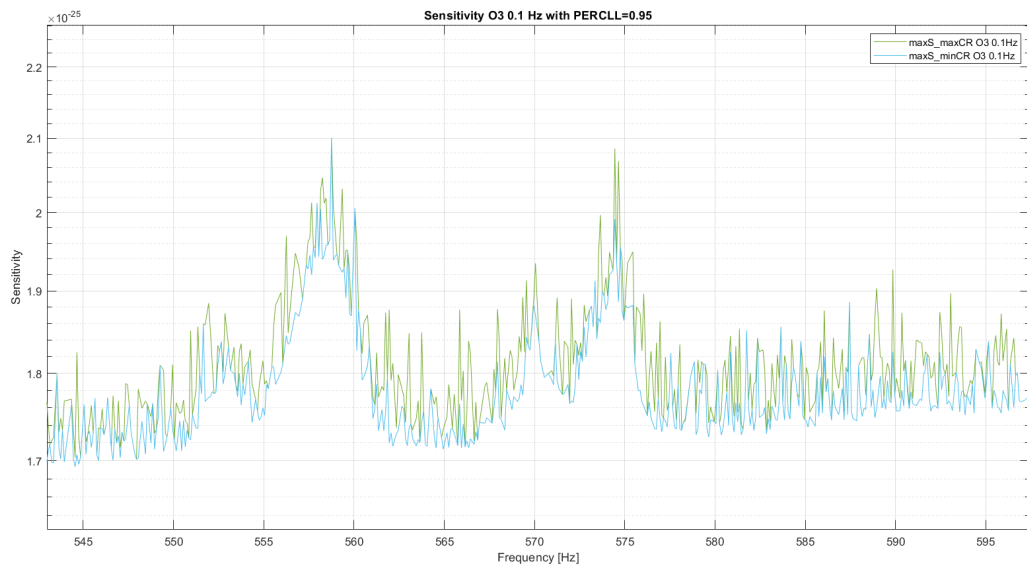
Figure 3.12. The two curves for frequency step equal to 0.1 Hz have been discarded in the final results because they are not well separated i.e. the UL and sensitivity curves can't be properly defined.
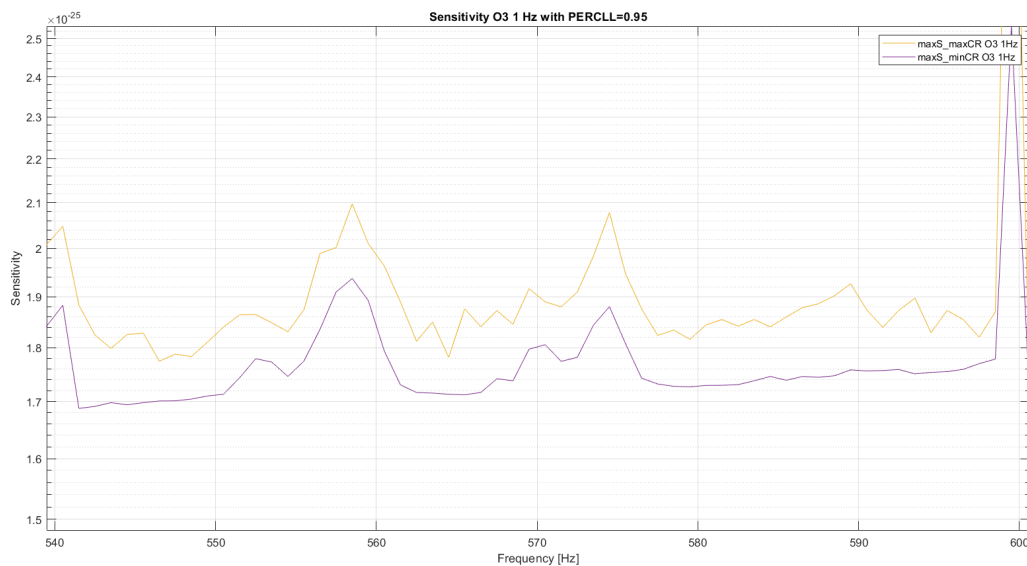

Figure 3.13. The two curves for a frequency step of 1 Hz in the same frequency range of Fig. 3.12. In this case, a precise distinction can be made.

Chapter 4

A new algorithm

In the previous Chapter I used Candidates and sensitivities computed from the FH pipeline with the standard four-bands division $[10 - 128]$ Hz, $[128 - 512]$ Hz, $[512 - 1024]$ Hz and $[1024 - 2048]$ Hz. With this method, four SFDBs are created and then fed to the pipeline as already discussed in Section 2.1. The aim of the current Chapter is to switch from the database input SFDB to BSD while keeping the remaining part of the FH algorithm unchanged. This would increase the sensitivity of the code especially for the lowest frequency of each of the four intervals, who were in fact penalized by the choice of the coherence time T_{FFT}, Section 2.2.2.

In Section 4.1 I will discuss about how the BSD was implemented in the FH pipeline, and show Hough maps after having applied different Doppler correction methods. In Section 4.1.2 there will be faced the limits of the T_{FFT} length respect to the *optimal* one by showing the behaviour of the Critical ratio CR as its function.

4.1 BSD as new input in the FH algorithm

In this first part of the Chapter, the purpose was the implementation of the BSD framework instead of the old SFDB. An important difference from this two database is the tunability of the coherence time T_{FFT}; for SFDB it is fixed for a large interval of frequency penalizing the lower frequencies of each band. The request for the T_{FFT} is that the Doppler effect has to be contained in a frequency bin δf: this suits the higher frequency of each interval, but for the lower ones the bin is even too large. Then, with an appropriate T_{FFT}, which is greater that the standard one, δf would be smaller with an improvement of the analysis for the aforementioned frequencies. In this thesis the implementation was compared for three Doppler corrections: $hfdf$, *heterodyne* and in absence of correction (none). The first correction is the one actually used in the FH pipeline also in the All-sky searches for which the second one is inapplicable because it needs the frequency of the source to be known. Further details on the code are provided in Appendix B.1.

The $hfdf$ Doppler correction method has already been discussed in Section 2.1.2. For what concerns *heterodyne* correction, it has the form of [30]

$$y(t) = [h(t) + n(t)]e^{-i\Phi_{corr}(t)}$$

where $h(t)$ and $n(t)$ are the GW signal and the noise, respectively, and $\Phi_{corr}(t)$ is the total phase correction (Doppler + spin-down)

$$\Phi_{corr}(t) = \phi_d(t) + \phi_{sd}(t)$$

where

$$\phi_d(t) = 2\pi \int_{t_0}^{t} f_0(t') \frac{\vec{v} \cdot \hat{n}}{c} dt' \approx \frac{2\pi}{c} p_{\hat{n}}(t) f_0(t) \tag{4.1}$$

$$\phi_{sd} = 2\pi \int_{t_0}^{t} \left[\dot{f}_0(t' - t_0) + \frac{1}{2}\ddot{f}_0(t' - t_0)^2 + ... \right] dt'$$

As one would expect from the *hfdf*, after the *heterodyne* correction the signal should appear monochromatic, except for residual modulations. In our case, only the $\phi_d(t)$ Doppler correction is performed.

4.1.1 BSD and the Doppler-correction methods

In this Section I show and discuss the results concerning the two Doppler correction methods, *hfdf* and *heterodyne*, thanks to the Hough maps computed with the BSD-implementation in Section 4.1. It will be also provided the Hough map without any correction (none) in order to show the impact of the corrections on the data. Some examples will be provided by running the code for some known HIs whose T_{FFT} still belong to the standard four-bands division. From the HIs that are available, the ones chosen as examples are, sorted by frequency: pulsar10, pulsar3, pulsar6 and pulsar1. For each of the HIs, the Table 4.1 summarizes the frequencies computed in the function together with the spin-down, the strain amplitude associated and the T_{FFT} of the SFDB. The two times at which the frequencies are calculated are the BSD initial time t_{BSD} and the Hough map initial time t_H. It's worth to notice that the number of digits reported are not the same for all the HIs: this has been done to underline the difference from $f(t_{BSD})$ and $f(t_H)$ for each pulsar. Moreover, here the initial time of the run and of the BSD coincide, hence only $f(t_{BSD})$ is reported to avoid redundancy; anyway, in general this is not always true. In this case, the two times in the Table are: $t_{BSD} = 1/Apr/2019\ 00:00:00$ and $t_H = 28/Sep/2019\ 20:22:15$ (hence in the middle time of t_{BSD}).

	$f(t_{BSD})$ [Hz]	$f(t_H)$ [Hz]	$\dot{f}(t_{BSD})$	h_0	T_{FFT} [s]
pulsar10	26.332	26.331	-8.50·10^{-11}	6.26·10^{-25}	8192
pulsar3	108.8571593929	108.8571593927	-6.73·10^{-9}	1.29·10^{-25}	8192
pulsar6	145.445	145.340	-1.46·10^{-17}	3.84·10^{-25}	4096
pulsar1	848.937	848.932	-3.00·10^{-10}	5.47·10^{-25}	2048

Table 4.1. The pulsars with their frequencies at the BSD initial time $f(t_{BSD})$ and Hough map initial time $f(t_H)$ with. In the table are also reported the $\dot{f}(t_{BSD})$ (since the time of *BSD* coincides with the run initial time), the strain h_0 and the standard T_{FFT} for the classic SFDB of the HI.

The first two HIs lie near the opposite extreme values of the first frequency band which is $[10 - 128]$ Hz; pulsar6 belongs to the second frequency band $[128 - 512]$

while pulsar1 to the third one $[512 - 1024]$ Hz. Here I present the pulsar Hough maps for their standard T_{FFT}, but the reason of their choice concerns specifically the improvement that will be visible thanks to the gain in the CR with a different T_{FFT}, especially for the HIs with the lowest frequency of their own band.

(a) Hough map with *hfdf* correction.

(b) x projection for the Hough map on the left.

(c) Hough map with *heterodyne* correction.

(d) x projection for the Hough map on the left.

(e) Hough map without correction.
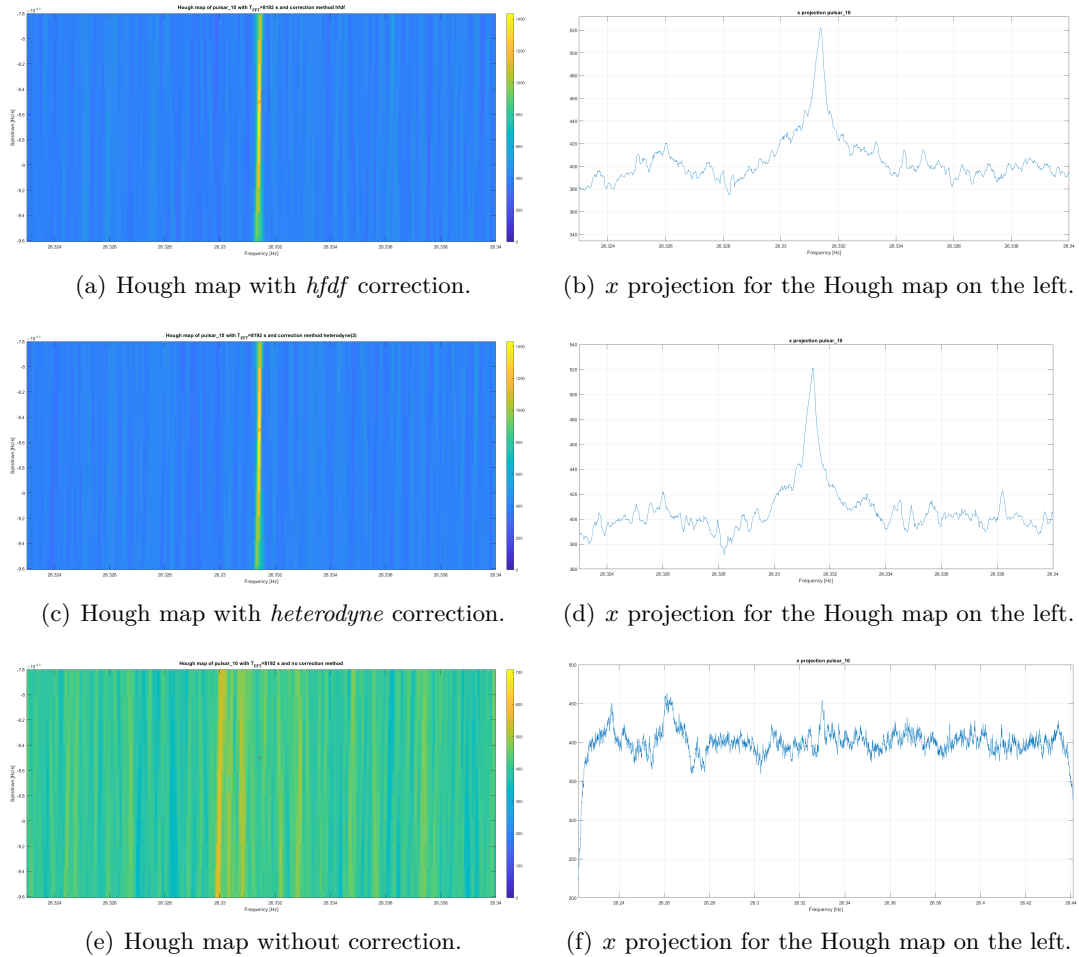

(f) x projection for the Hough map on the left.

Figure 4.1. This collage gathers the three Hough maps for pulsar6. On the right of each Hough map it is reported the projection respect to the Frequency axes. It's clearly visible the SI pulsar10 in the corrections thanks to the peaks in the number count whilst it can't be recognized in the last x projection.

(a) Hough map with *hfdf* correction.

(b) x projection for the Hough map on the left.

(c) Hough map with *heterodyne* correction.

(d) *x* projection for the Hough map on the left.

(e) Hough map without correction.

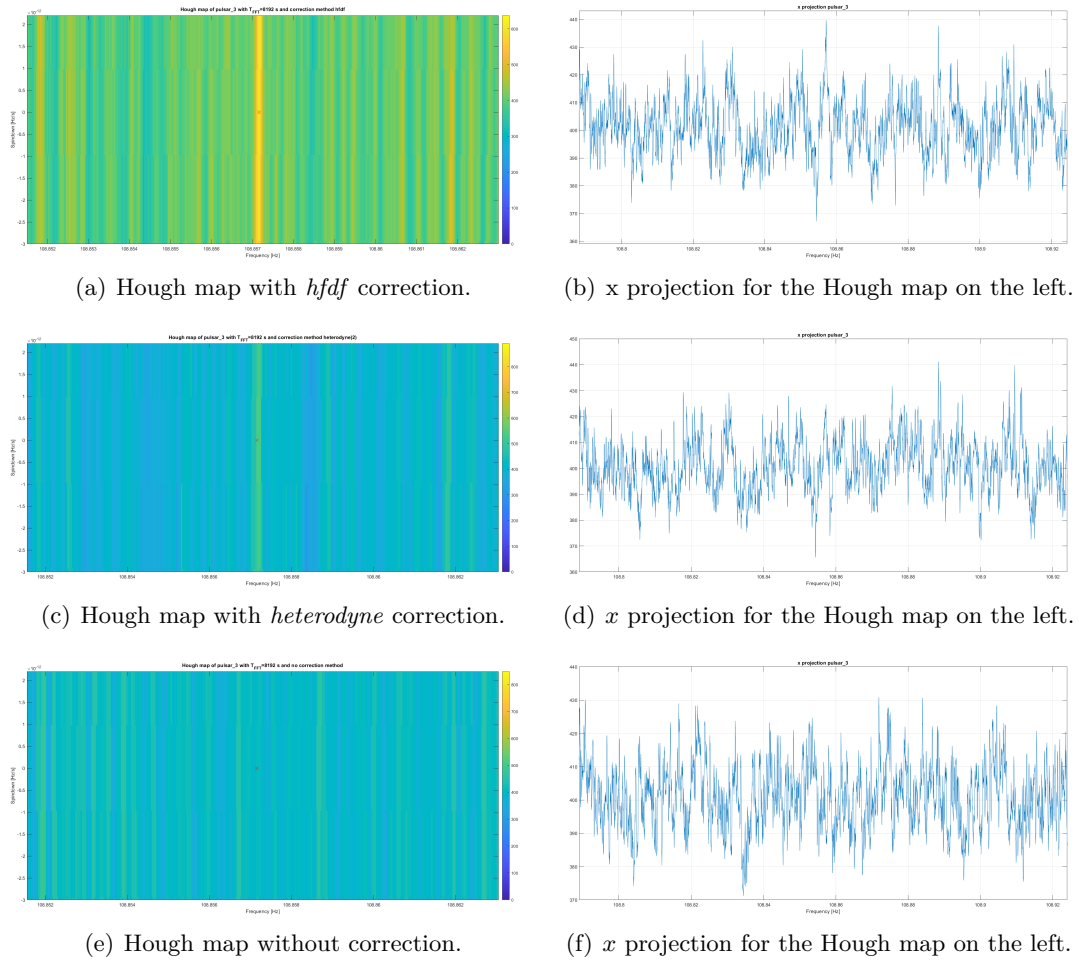(f) *x* projection for the Hough map on the left.

Figure 4.2. This collage gathers the three Hough maps for pulsar3. On the right of each Hough map it is reported the projection respect to the Frequency axes. The *hfdf* correction gives the most clear signal while for *heterodyne* and the *none* corrections there isn't shown any dominant peak.
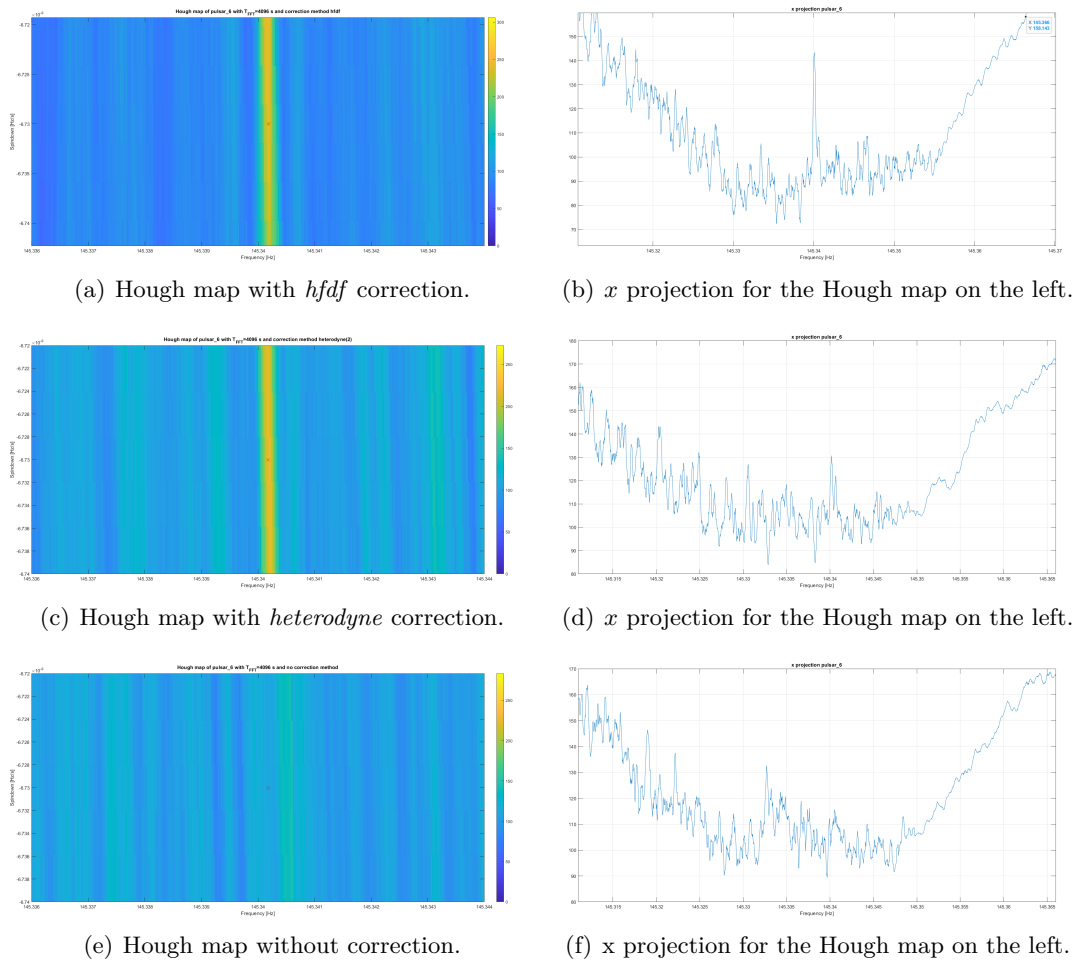
(a) Hough map with *hfdf* correction.

(b) *x* projection for the Hough map on the left.

(c) Hough map with *heterodyne* correction.

(d) *x* projection for the Hough map on the left.

(e) Hough map without correction.

(f) x projection for the Hough map on the left.

Figure 4.3. This third collage gathers the three Hough maps for pulsar6. On the right of each Hough map it is reported the projection respect to the Frequency axes. Both *hfdf* and *heterodyne* corrections shows a distinct color from the background that indicates the pulsar6 coordinates. In *hfdf* it is clearly visible a peak in the *x* projection.
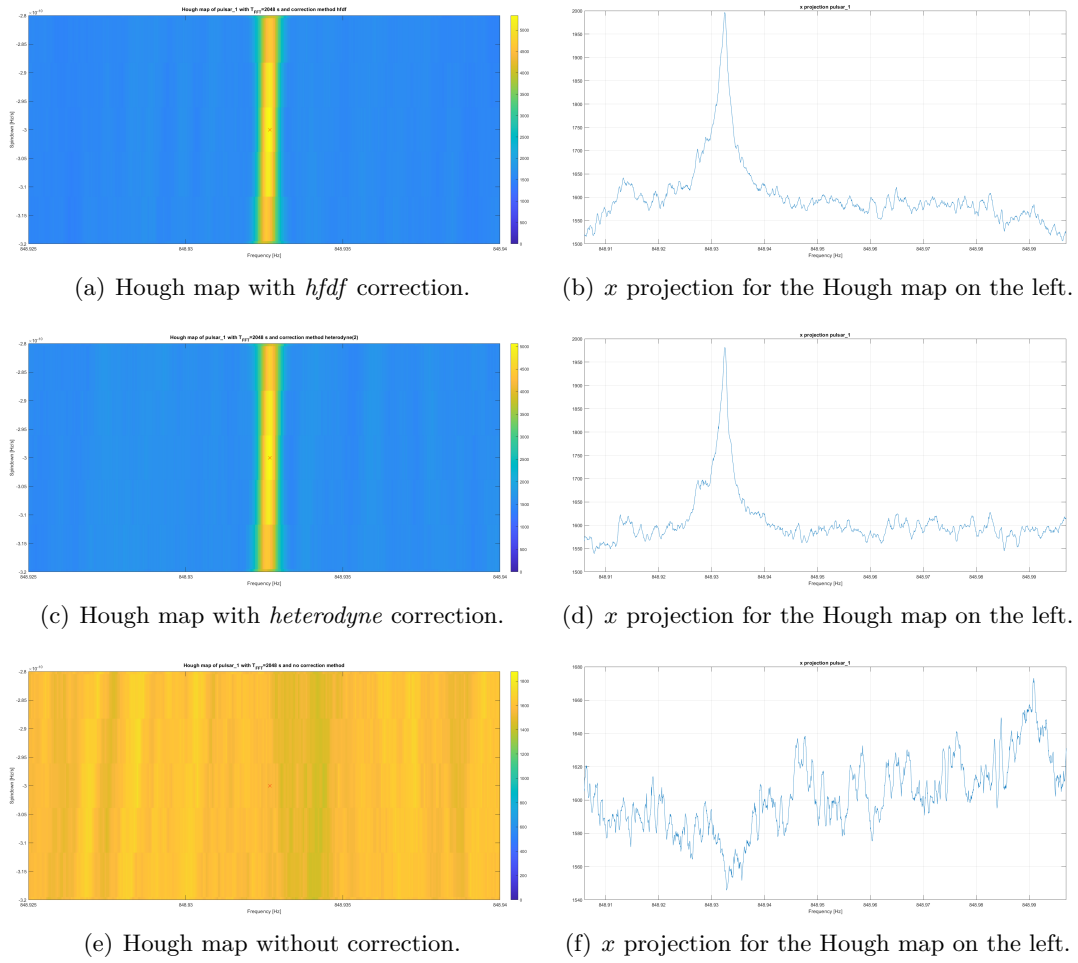
(a) Hough map with *hfdf* correction.

(b) *x* projection for the Hough map on the left.

(c) Hough map with *heterodyne* correction.

(d) *x* projection for the Hough map on the left.

(e) Hough map without correction.

(f) *x* projection for the Hough map on the left.

Figure 4.4. This last collage gathers the three Hough maps for pulsar1. On the right of each Hough map it is reported the projection respect to the Frequency axes. As can be seen from the *none* correction, the signal would be absolutely invisible and surrounded in the background; but thanks to the two correction, an evident peak appears in the *x* projection.

The collages of Figs. 4.1, 4.2, 4.3 and 4.4 show the Hough map on the left with their *x* projection on the right for the three corrections: *hfdf, heterodyne* and *none*. The *x* projection is an histogram. The red cross that is present in all the Hough maps stands for the expected pulsar position if updated at the time of the Hough map which is in the middle respect to the BSD initial time. It can be found in the pixel with the highest number count or in the one next to it: this is due to the absence of the spin-down correction which makes the Doppler correction less precise; the choice to overlook this parameter was due to the computational weight of the code, but it can be changed if requested.

	n_{hfdf}	n_{het2}
pulsar10	1434.62	1430.21
pulsar3	637.51	535.79
pulsar6	240.52	221.83
pulsar1	5340.72	5068.83

Table 4.2. Here are reported the number counts n of the HIs for the two corrections methods.

4.1.2 Limits of the T_{FFT} length

The previous results concerned the standard coherence time. The BSD improvement is the opportunity to change T_{FFT} with the aim of finding the optimal coherence time. With *optimal* coherence time I'm referring to the T_{FFT} that gives the highest CR for the chosen HI. This is extremely useful for the signals with lowest amplitude because with the standard T_{FFT} they could be difficult to identify - or worse: they could be missed - in the analysis.

The standard values of the four-bands division are the nearest numbers in power of 2 to the T_{FFT} defined in Eq. 2.1. For example, in the $[10 - 128]$ Hz band from the aforementioned equation it is $T_{FFT} \sim 9723$ s and the nearest power of 2 is $T_{FTT} = 2^{13} = 8192$ s. Instead, for the optimal T_{FFT} more variables are involved. The approximations concern the frequency modulation formula [9]

$$f(t) = f_0 - Asin(\Omega_{rot}t + \phi_a - \alpha) + Bsin(\Omega_{orb}t + \phi_b) \tag{4.2}$$

where Ω_{rot} and Ω_{orb} are the sidereal and the angular orbital frequency respectively, ϕ_a and ϕ_b constant phases, α the right ascension of the source and f_0 the GW frequency at the source. The orbital amplitude is

$$A = f_0 R_E \Omega_{orb} cos\phi cos\delta/c$$

where R_E is the Earth radius, ϕ is the latitude of the detector and δ the declination of the source.

The maximum sideral contribution to the Doppler is

$$a = \left| \frac{df_{rot}}{dt} \right|_{max} = A \cdot \Omega_{rot} \cdot cos(\Omega_{rot} + \phi_a - \alpha)|_{max} \tag{4.3}$$

the maximum value that a cosine function can assume is 1, hence $cos(\Omega_{rot} + \phi_a - \alpha)|_{max} = 1$

$$a = A \cdot \Omega_{rot} = (f_0 R_E cos\phi cos\delta/c) \cdot \Omega_{rot} \tag{4.4}$$

For the orbital modulation the amplitude is

$$B = f_0 R_{orb} \Omega_{orb}/c$$

whilst the maximum contribution

$$b = \left| \frac{df_{orb}}{dt} \right|_{max} = B \cdot \Omega_{orb} \cdot cos(\Omega_{orb}t + \phi_b)|_{max} \tag{4.5}$$

and, like before, $cos(\Omega_{orb}t + \phi_b)|_{max} = 1$

$$b = B \cdot \Omega_{orb} = (f_0 R_{orb}\Omega_{orb}/c) \cdot \Omega_{orb} \tag{4.6}$$

In order to have the Doppler modulation confined within a frequency bin, it has to be

$$\frac{1}{T_{FFT}} > T_{FFT}(a + b) \rightarrow T_{FFT} < \sqrt{\frac{1}{(a + b)}}$$

The optimal T_{FFT} is defined as

$$T_{FFT}^{opt} = \sqrt{\frac{1}{(a + b)}} \tag{4.7}$$

The value of the optimal T_{FFT} changes along with a and b, therefore with the approximations one makes for these Doppler contributions. For example, the rotational shift a can be taken into account while neglecting b, or it can be considered the reverse case by taking b but not a. Here I am discussing about a specific source and detector, but even these parameters can be generalized by setting $cos\delta = 1$ for the former and $cos\phi = 1$ for the latter; with $cos\phi = cos\delta = 1$ at the same time, it is computed the lowest optimal T_{FFT} due to the maximization of the cosine functions. By putting both of the cosines equal to 1 in Eqs. 4.3 and 4.5, I am taking the *minimum* value amongst the possible optimal times[1]. In our case it is sufficient to set this condition, but in order to be more precise there should be verified the actual values that $\Omega_{rot}t + \phi_a$ and $\Omega_{orb}t + \phi_b$ can assume and then take the maximum of the full-arguments cosines.

Here below it is reported Table 4.3 which summarizes the three T_{FFT} approxmations (rotational, orbital, both) together with the *standard* one i.e. the coherence time that comes from the SFDB. From this same table it can bee seen that, for the chosen pulsars, the coherence time in the orbital approximation, i.e. T_{FFT}^{orb}, is the longest one for every pulsar due to the fact that in these cases $b < a$ (anyway, this is not a rule).

	f [Hz]	T_{FFT}^{std} [s]	$T_{FFT}^{opt,rot}$ [s]	$T_{FFT}^{opt,orb}$ [s]	$T_{FFT}^{opt,rot+orb}$ [s]
pulsar10	26.36	8192	24825.38	43794.09	21596.78
pulsar3	108.86	8192	11447.63	21550.17	10109.75
pulsar6	145.44	4096	13872.89	18437.24	11085.32
pulsar1	848.95	1024	4012.64	7716.21	3560.04

Table 4.3. This table summarizes the principal T_{FFT}s taken into account in the code for each pulsar.

In order to have an adequate understanding of the CR respect to the T_{FFT}, a number of point equal to 80 has been computed in addition to the three values of the approximations; in these 80 points it is included the *standard* T_{FFT}. The overall number of T_{FFT}s computed is 83 T_{FFT}.

Here in the followings are reported the results for the pulsars for both the corrections: *hfdf* and *heterodyne.*

---

[1] $cos\delta$ and $cos\phi$ are *not* equal to 1 here.
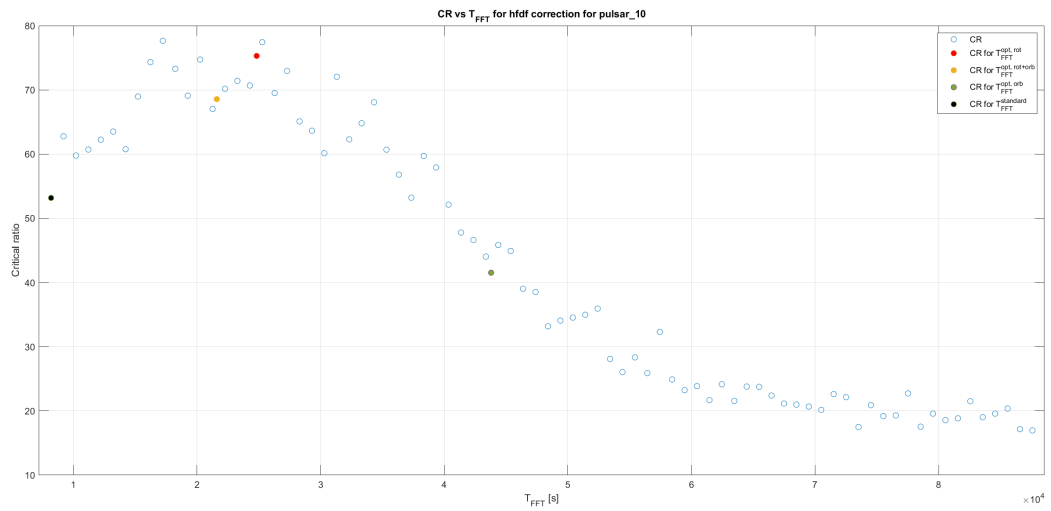
(a) CR computed for different T_{FFT}s for *hfdf* correction.
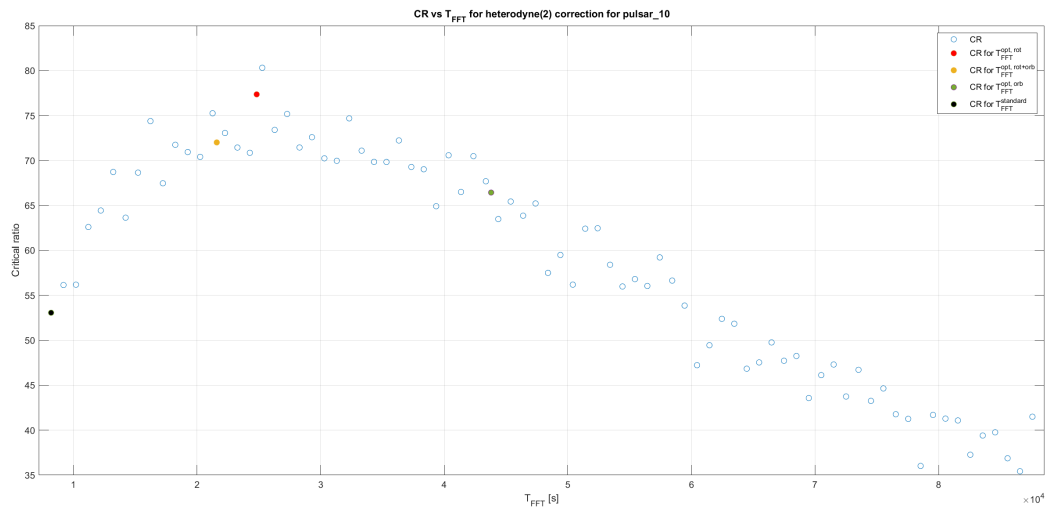
(b) CR computed for different T_{FFT}s for *heterodyne* correction.

Figure 4.5. CR vs T_{FFT} for pulsar10.
$f(t_{BSD}) = 26.33$ Hz and $\dot{f}(t_{BSD}) = -8.50 \cdot 10^{-11}$ Hz/s.
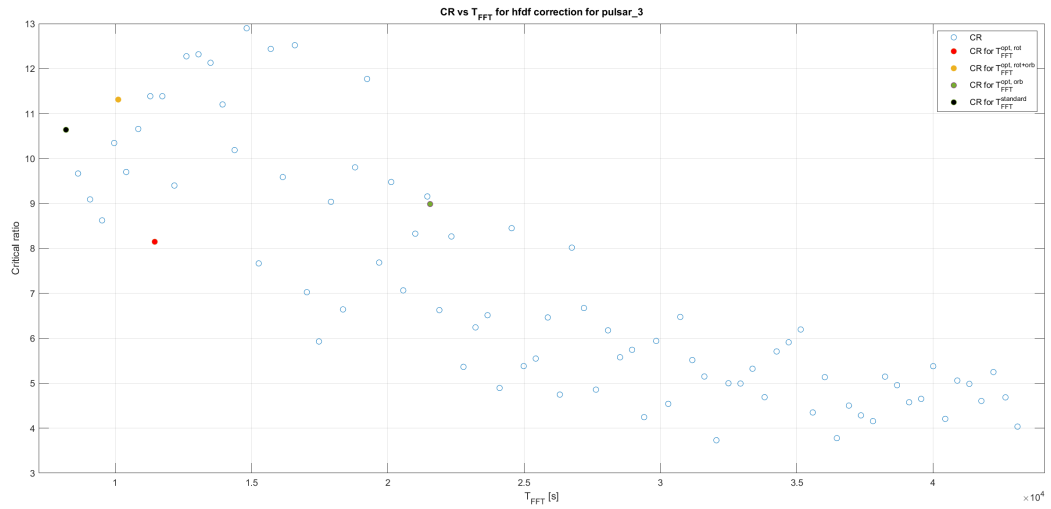
(a) CR computed for different T_{FFT}s for *hfdf* correction.
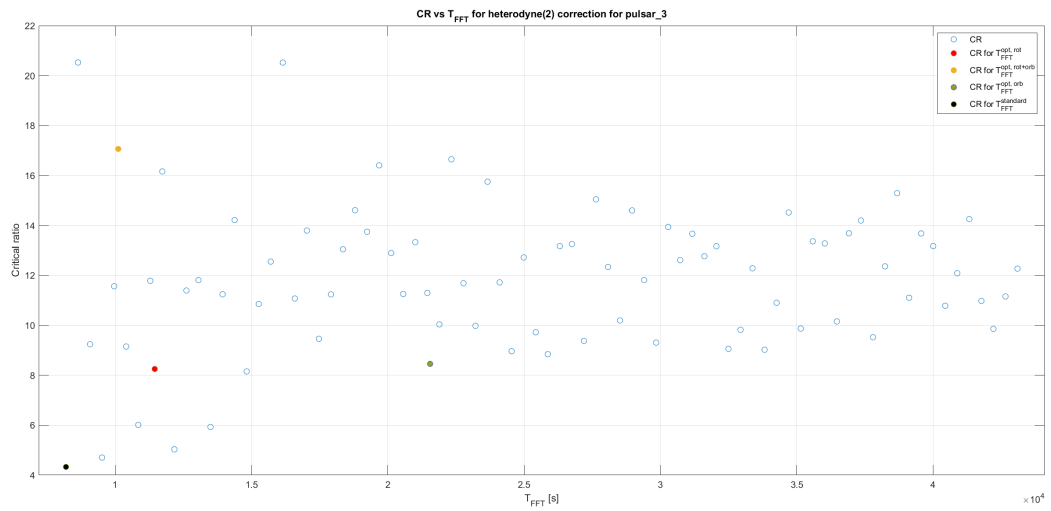
(b) CR computed for different T_{FFT}s for *heterodyne* correction.

Figure 4.6. CR vs T_{FFT} for pulsar3.
$f(t_{BSD}) = 108.86$ Hz and $\dot{f}(t_{BSD}) = -1.46 \cdot 10^{-17}$ Hz/s.
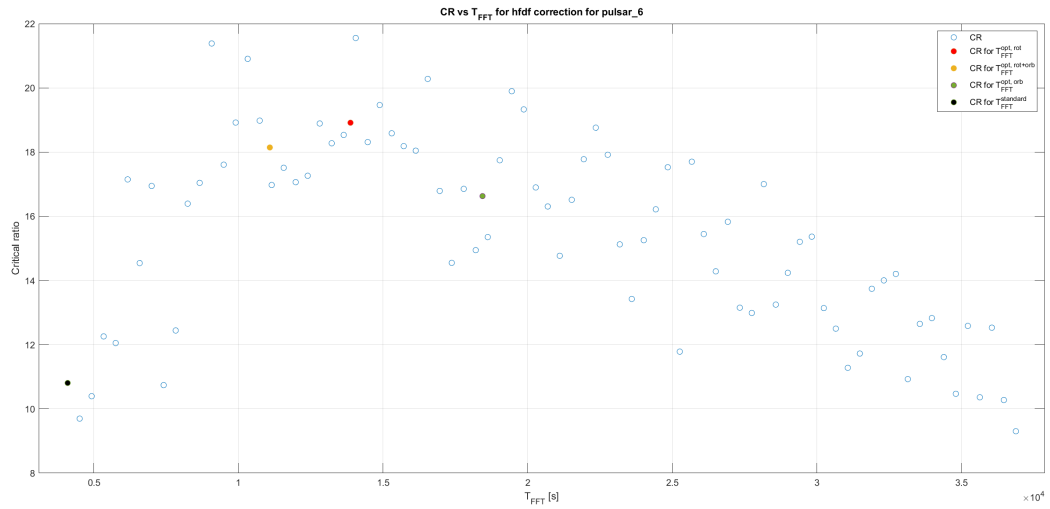
(a) CR computed for different T_{FFT}s for *hfdf* correction.
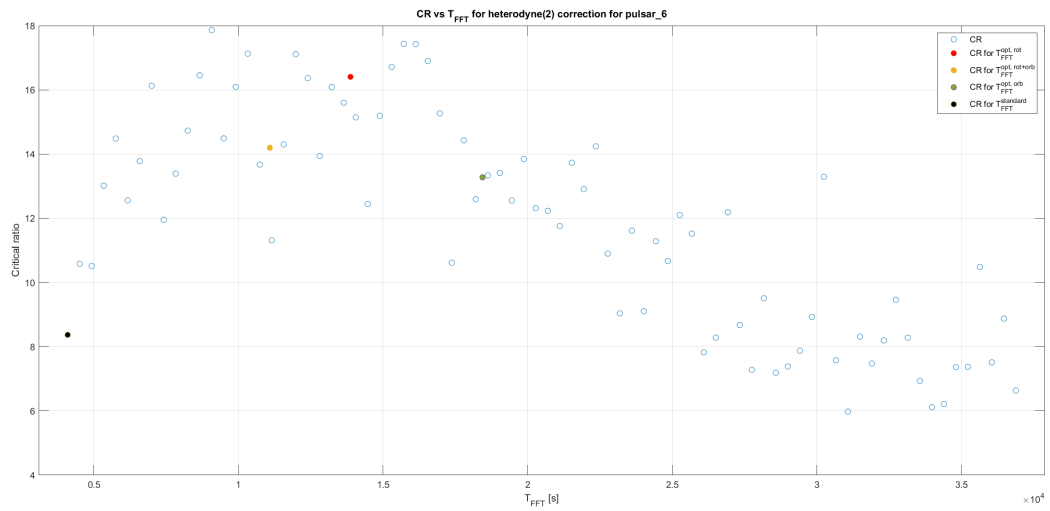
(b) CR computed for different T_{FFT}s for *heterodyne* correction.
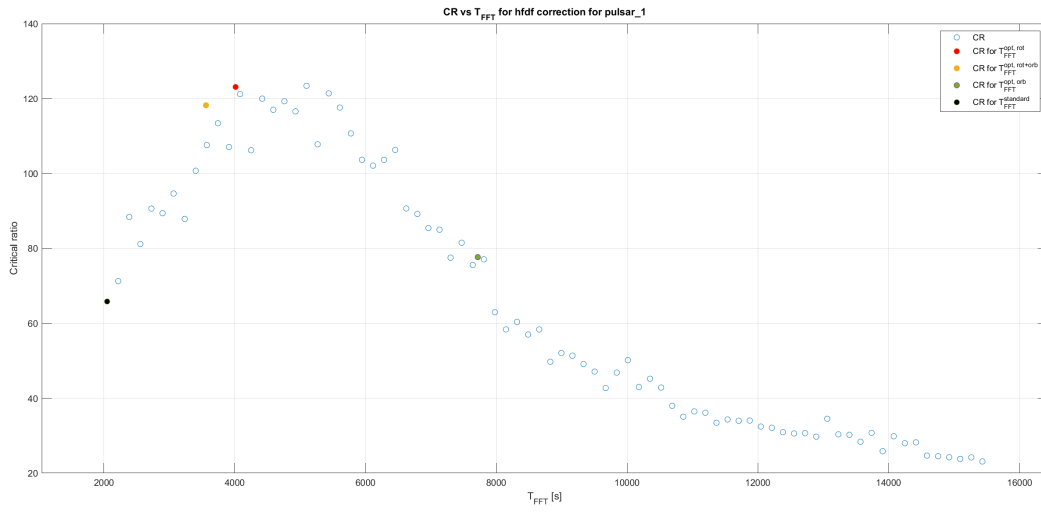
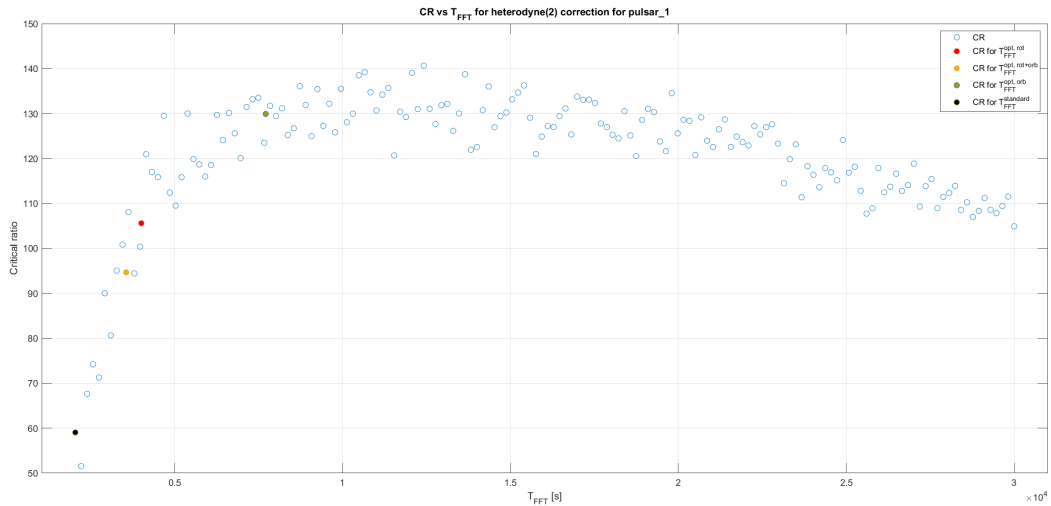**Figure 4.7.** CR vs T_{FFT} for pulsar6.
$f(t_{BSD}) = 145.44$ Hz and $\dot{f}(t_{BSD}) = -6.73 \cdot 10^{-9}$ Hz/s.

(a) CR computed for different T_{FFT} for *hfdf* correction.

(b) CR computed for different T_{FFT}s for *heterodyne* correction.

Figure 4.8. CR vs T_{FFT} for pulsar1.
$f(t_{BSD}) = 848.94$ Hz and $\dot{f}(t_{BSD}) = -3.00 \cdot 10^{-10}$ Hz/s.

In this context it is confirmed how the choice of the pulsars in Table 4.1 is coming useful: thanks to pulsar10 and pulsar3 a direct comparison between the two extremes point of $[10-128]$ Hz can be performed while pulsar6 shows the improvement in the second frequency band and pulsar1 in the third one.

Figs. 4.5, 4.6, 4.7 show the CR values respect to T_{FFT} with empty blue circles; the filled ones are the T_{FFT} from Table 4.3 with T_{FFT}^{std} in black, $T_{FFT}^{opt,rot}$ in red, $T_{FFT}^{opt,rot+orb}$ in yellow and $T_{FFT}^{opt,orb}$ in dark green.

Starting from the first pulsar, i.e. pulsar10, it can been seen how for the two corrections the behaviour of CR respect to T_{FFT} is similar: T_{FFT}^{std} is the first value of the plot and, respect to the three approximations, gives the lowest CR for the first

half of the interval; for pulsar10 the maximum CR can be found near $T_{FFT}^{opt,rot+orb}$ and $T_{FFT}^{opt,rot}$ with a clear improvement respect to the CR for T_{FFT}^{std}. After the peak, the value of CR slowly decreases due to the excessive length of the T_{FFT}: as aforementioned in the previous Sections, the frequency bin is $\delta f = \frac{1}{T_{FFT}}$, with the request of the confinement of the Doppler effect within a bin. If T_{FFT} becomes too long, this request breaks down and the signal is distributed in more bins making the corresponding CR lower.

For pulsar3 the two corrections show slightly different behaviours: for *hfdf* there is a slow slope from the first T_{FFT} value whilst in *heterodyne* the CRs form almost a plateau. Respect to the comments about pulsar10, here there isn't a clear distinction amongst the CRs from the three approximations and T_{FFT}^{std}; this is can be accounted as a proof of how the improvement in the T_{FFT} value concerns mainly the lower frequencies of the SFDB intervals.

A similar behaviour of pulsar10 is found in pulsar6: this HI is at the beginning of the second frequency band $[128 - 512]$ Hz. As before, the CR assumes higher and higher values as it approaches a T_{FFT} near $T_{FFT}^{opt,rot+orb}$ and $T_{FFT}^{opt,rot}$ after which it decreases.

As last HI there is pulsar1. For the heterodyne correction of this pulsar, more points have been computed (160) in order to have an adequate understanding of the CR trend until $T_{FFT} \sim 30000$ s. In fact, while the CRs after $T_{FFT} \sim 5000$ s rapidly decrease for *hfdf* correction, they keep an almost constant value until $T_{FFT} \sim 15000$ s in the heterodyne. The trend is therefore slower, with a smaller slope respect to the other Doppler correction. This is due to the fact that the for the heterodyne the HI keeps being contained in the frequency bin for more T_{FFT}s also thanks to its spin-down. This occurs also in the other two available pulsars in the third band, i.e. pulsar2 and pulsar9.

From the collection of figures reported and discussed above, it appears clear the

	f [Hz]	CR_{hfdf}^{std}	$CR_{hfdf}^{opt,rot}$	$CR_{hfdf}^{opt,orb}$	$CR_{hfdf}^{opt,rot+orb}$
pulsar10	26.33	53.17	75.29	41.52	68.56
pulsar3	108.86	10.64	8.15	8.99	11.31
pulsar6	145.44	10.81	18.91	16.63	18.14
pulsar1	848.95	59.05	105.59	129.92	94.67

Table 4.4. The CRs associated to the four T_{FFT}s for the *hfdf* Doppler correction.

|	f [Hz]	CR_{het}^{std}	$CR_{het}^{opt,rot}$	$CR_{het}^{opt,orb}$	$CR_{het}^{opt,rot+orb}$
pulsar10	26.33	53.06	77.34	66.43	72.01
pulsar3	108.86	4.33	8.25	8.45	17.06
pulsar6	145.44	8.37	16.41	13.28	14.19
pulsar1	848.95	59.05	105.59	129.92	94.67

Table 4.5. The CRs associated to the four T_{FFT}s for the *heterodyne* Doppler correction.

improvement regarding the BSD database thanks to its tunable T_{FFT} respect to the

standard ones from the SFDB.

It is useful to recall that the Critical ratio, i.e. CR, is a statistical parameter whose meaning is, given a number N of FFTs, to weight the number count of the Hough map n respect to the probability that the associated pixel contains noise, Section 2.1.4 Eq. 2.8.

The role of changing the length of the T_{FFT} is then to improve the CR due to the different number N of FFTs that are constructed. Hence, whilst the number count n can diminish due to the redistribution of the noise with the T_{FFT} associated to the highest CR, this former parameter is the one to take into account in the following step of the analysis; therefore it is not a case that the next step of the FH pipeline selects candidates respect to a CR_{thr}.
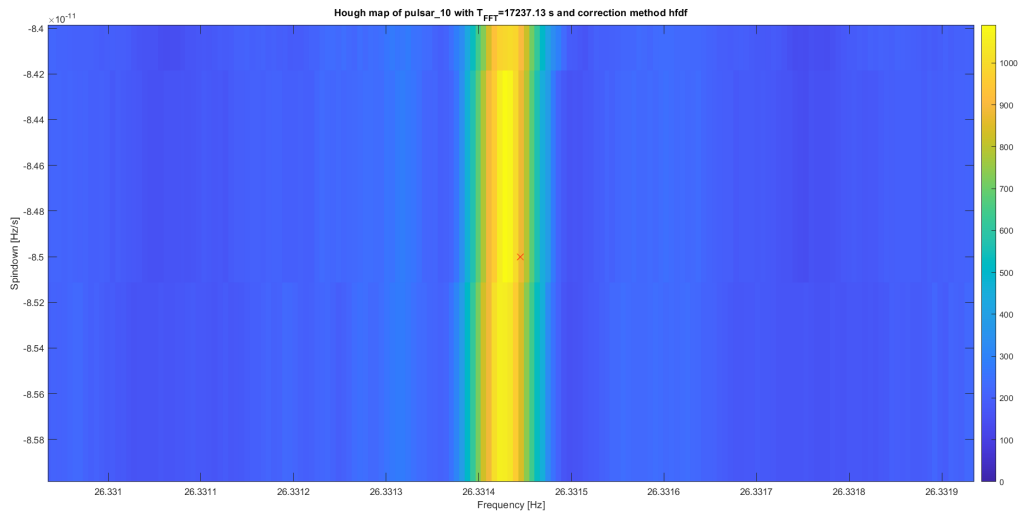
(a) Hough map for $T_{FFT}^{CR_{max}}$ for *hfdf* correction.
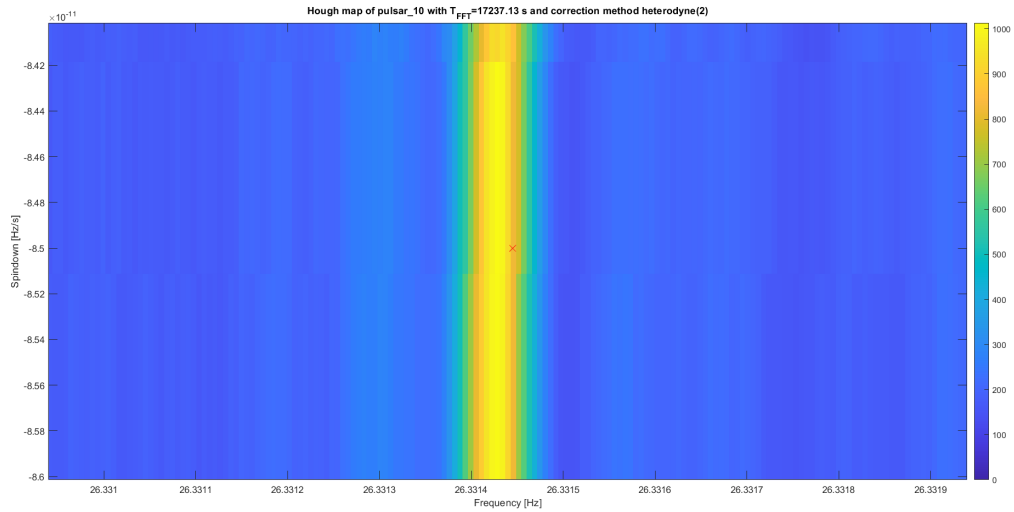
(b) Hough map for $T_{FFT}^{CR_{max}}$s for *heterodyne* correction.

Figure 4.9. Hough map for the T_{FFT} which gives the maximum CR for pulsar10

	n_{hfdf}^{std}	n_{hfdf}^{max}	n_{het}^{std}	n_{het}^{max}
pulsar10	1434.62	1091.09	1430.21	1013.20

Table 4.6. This table summarizes the number count n for the two corrections. For T_{FFT}^{std} the data are taken from Table 4.2, while the others are from $T_{FFT}^{CR_{max}}$ which gives the highest CR. As discussed in the text, the parameter to take into account for the following pipeline steps is the CR not n; hence while $n_{hfdf,het}^{max}<n_{hfdf,het}^{std}$, the signal is improved because of the CR.

Conclusions

The work of thesis is divided in two communicating halves. The first accomplishment of this work was the computation of a new Upper limit (UL) and sensitivity curves with the purpose of saving computational power in the future. This was necessary due to the heavy old procedure that injected 100 SIs every 1 Hz for a fixed amplitude, and then again for more different amplitudes. Thanks to the encouraging results obtained with the comparison with O2, I produced for O3 an alternative UL curve that was slightly overestimated respect to the real UL but still a valid result. Moreover, I was able to define a O3 new sensitivity curve as well.

The second half of this thesis was focused on the implementation of a new framework called Band Sampled Data (BSD) instead of the standard SFDB as input database in the Frequency Hough (FH) pipeline. This approach gave to the lower frequencies of the SFDB the right Doppler effect estimation: in the old database this effect was in fact over-estimated. After the implementation, thanks to Hardware injections (HIs), the code was tested in two Doppler corrections and in absence of any frequency modulation: *hfdf*, *heterodyne* and *no correction* (none). This lead to a first comparison between the three cases with their Hough maps, where the $hfdf$ is the method actually used in the FH pipeline. After that, the code run for several T_{FFT}s for both the corrections in order to see which one of them would have given the maximum CR respect to the ones computed for the standard T_{FFT}s. Thanks to this, it has been proved the gain in the value of the Critical Ratio of the injected pulsars, especially for ones with low frequencies respect to the upper frequencies of the old four band division. This result makes valid the conclusion that the introduction of the BSD as input can make possible a detection of a low-CR signal due to the enhancement of the Critical ratio. This is surely a starting point to have an improved sensitivity curve of the detectors as well. Beyond the work of this thesis, the following step will be a comparison between the old SFDB framework and the new BSD in the FH pipeline in the All-sky search in order to understand the details of the amelioration.

Appendix A

New estimation algorithm

In this Appendix I will describe in detail the algorithm used for the sensitivity recalibration.

The function I wrote is named `funz_sens` with the following form

$$[\text{sens\_combined}]=\text{funz\_sens(Cand\_all,run,f\_step,sens)} \qquad (A.1)$$

the input (`Cand_all, run, f_step, sens`) are

- `Cand_all`: a $\{1 \times 4\}$ cell array in which each cell contains the full band candidates of the selected detector, i.e. for LIGO Hanford and Livingston:
  `Cand_all={Cand_HO2, Cand_LO2, Cand_HO3, Cand_LO3}`
  in the form of a [9,N] matrix Cand=[frequency; λ; β; spin-down; amplitude; CR; $\delta\lambda$; $\delta\beta$; type];

- `run`: the two run that are available are O2 and O3;

- `f_step`: the frequency step for the candidate selection;

- `sens`: the sensitivity, i.e. $h_{0,min}$ used for the recalibration, for example `sens=[frequency sensHanford sensLivingston]`.

while the output is `sens_combined` i.e. the recalibrated sensitivity that is given as a [N,12] matrix of columns `sens_combined=[freq, newsensH_max, CR_Hmax, newsensH_min, CR_Hmin, newsensL_max, CR_Lmax, newsensL_min, CR_Lmin, newsensHmean, CR_Hmean, newsensLmean, CR_Lmean]`.

These elements will be explained and discussed in the followings.

For what concern O2, the input of the function are

$$[\text{sens\_O2\_combined}]= \text{funz\_sens(Cand\_all\_freq,'O2',fstepO2)} \qquad (A.2)$$

where $\text{fstepO2} = 1$ Hz but it is tunable. The choice relays on the step interval used in the UL. The code operates as follows.

First, it is checked the existence of the frequency step as input: if it is not present, the standard value of $\text{f\_step} = 1$ Hz is taken. After that, for run O2 the sensitivity input is loaded even if not explicitly given.

The core of the algorithm is the selection of the candidates of each detector

which are within the frequency interval. The `for` cycle starts with f=10 Hz and ends at f=2048 Hz accordingly to the FH pipeline, with step `f_step`, i.e. `for freq=10:f_step:2048`. If the interval [frequency frequency+f_step] doesn't involve any candidate, hence it is empty, the cycle simply skips to the next one. If at least one candidate is present, these operations are performed:

- minimum CR amongst the candidates of the interval
  `CR_min_H=min(CR_Htemp(6,kkHL))`
  `CR_min_L=min(CR_Ltemp(6,kkHL));`

- maximum CR
  `CR_max_H=max(CR_Htemp(6,kkHL))`
  `CR_max_L=max(CR_Ltemp(6,kkHL));`

- mean of all the candidates CR of the interval to compute a CR mean
  `CR_mean_H=mean(CR_Htemp(6,kkHL))`
  `CR_mean_L=mean(CR_Ltemp(6,kkHL));`

where `CR_Htemp(6,kkHL)` and `CR_Ltemp(6,kkHL)` are the two temporary arrays of the i-th step and kkHL refers to the index candidates that are taken into account. All of this is saved in the odd columns of `sens_combined` as anticipated before, and the frequency is shifted to the middle frequency of the interval i.e. freq+f_step/2, in order to simplify the identification to which frequency interval the stored CR belongs. The even columns of the matrix are filled with the recalibrated sensitivities that are computed as follows.

For example, the resulting sensitivity of the LIGO Hanford (LH) detector if the minimum CR is used is

$$\vdots$$

`sens_combined(:,4)=sens_temp(:,2).*sqrt(CRmeas-AA)/sqrt(CRUSED-AA);`

$$\vdots$$

where `sens_temp(:,2)` is the input the sensitivity of LH, `CRmeas=CR_min_H`, `CRUSED=5` and `AA=`$-\sqrt{2}ercf^{-1}(2\Gamma)$.

The function `funz_sens` with input and output written in Eq. A.2 is called in the `DO_PLOTs_CRNEW.m` file in which is also loaded the Upper limit (UL) computed with software injections (SIs).

For what concern the results of O3, the procedure is analog. Function `funz_sens` takes the explicit form of

$$[\texttt{sens\_O3\_combined}]= \texttt{funz\_sens(Cand\_all\_freq,'O3',fstepO3)} \qquad (A.3)$$

where `fstepO3`=1, 0.1 Hz.

A slightly change respect to O2 is the preliminary threshold concerning the CR. For O2 the threshold was set to 0.1, but for O3 it depends on the frequency interval: CR=3 for $[10 - 128]$ Hz and CR=5 for $[128 - 2048]$ Hz.

Appendix B

BSD in Frequency Hough

B.1 Implementation

The core of the new algorithm is the function `bsd_2_hough`.m which has the following form
```
[hmap, job_info_s, pout, sky] = bsd_2_hough(bh, direct, Tfft, sd_lim,
patchon, freq_start, freq_step, ploton).
```
The input are

- `bh`: is the BSD and one of the output of another function called `bsd_lego`; this function gets access to the data once the path is given. One can choose the period length and frequency interval to be extracted as it has been discussed in Section 2.2.1;

- `direct`: a struct that contains information about the pulsar;

- `Tfft`: is the *coherence time*;

- `sd_lim`: is the spin-down interval to be taken into account;

- `patchon`: can assume three values: 1, 0 and -1.
  `patchon`=1 the *hfdf* Doppler correction is used (peaks shift, Section 2.1.2), `patchon`=0 implies *heterodyne* Doppler correction while `patchon`=-1 leaves the data uncorrected;

- `freq_start`: is used to plot the Peakmap and Hough map if `patchon`=1;

- `freq_step`: the frequency step of the two plots mentioned above;

- `ploton`: if `ploton`=1 the two plots are computed, otherwise the aren't.

For the output it is

- `hmap`: is the Hough map in gd2[1] format file that, if plotted, shows the 2D histrogram in the $(f_0, \dot{f}_0)$ plane with a side colored-bar indicating the number count n;

---

[1]A gd is a group of data defined by an abscissa and a single value; the gd2 format, also called Data Map, is a gd with a two dimension abscissa and it is used for bi-dimensional data like the time-frequency spectrum.

- `job_info_s`: is a struct including several typologies of information;

- `pout`: this Peakmap file is given in the form of a [5, N] matrix, pout=[time; frequency; amplitude; wien-nois; wien-nois_radpat];

- `sky`: is a struct that contains information about the point of the sky that is going to be analyzed. The `direct` data are assigned to it in order to look at its position.

The first step of the function is to assign some parameters of the `direct` to the `sky` struct. Among all the assignations, the most important ones are the sky coordinates (α, δ) and the frequency f_0; in the current analysis the correction regarding the spin down `df0` isn't performed, therefore it is set equal to zero for `sky`.

```
⋮
sky.a=direct.a;
sky.d=direct.d;
sky.f0=direct.f0;
sky.df0=0;
⋮
```

Then is checked the value of `patchon` in order to compute the Doppler correction that has been given in the input

```
⋮
switch patchon
case 1
disp('Using peaks correction (hfdf)')
case 0
disp('Using heterodyne correction')
sky
bh=bsd_dopp_sd(bh,sky); %heterodyne correction
case -1
disp('No correction')
end
⋮
```

The case `patchon`=0 corresponds to the *heterodyne* correction which is computed with the function `bsd_dopp_sd`. This typology of correction is suitable if the frequency and position of the source are already known, hence it couldn't be applied to our All-sky search. In fact, the heterodyne correction is used here only to compare its results with the *hfdf* which is the method actually used in the FH All-sky pipeline. For this value of `patchon`, the correction is performed at this point of the code and not after the construction of the Peakmap like in the *hfdf* case.

After having checked the correction to be applied, the Peakmap is computed with the `bsd_peakmap` function and saved in `tfstr` whose name stands for *time-frequency struct*

$\vdots$

```
tfstr=bsd_peakmap(bh,Tfft/dx);
```

$\vdots$

where `Tfft/dx` is the length of the FFTs, with `Tfft` as the FFTs time duration and `dx` as the sampling time. In this function, $\theta_{thr} = 2.5$.
The peaks are then extracted from the struct and saved in a new variable

$\vdots$

```
peaks=tfstr.pt.peaks;
```

$\vdots$

In order to obtain the velocities for the *hfdf* Doppler correction of the Peakmap, the function `interp1` is called thrice in the code. This function computes the three components of the velocities `vx_bsd_peaks`, `vy_bsd_peaks` and `vz_bsd_peaks` associated to the peaks of the Peakmap stored in `tfstr.pt.peaks(1,:)` from the velocities sampled in `job_info_s.bsdcont.v_eq(:,i)` with $i = 1, 2, 3$ for the x, y and z component at time `t_mjd`. By using a simplified notation, `Vq = interp1(X, V, Xq)` one can say that, from the values of `X` and `V`, the function `interp1` interpolates the values `Vq` associated to `Xq`.

$\vdots$

```
vx_bsd_peaks=interp1(t_mjd,job_info_s.bsdcont.v_eq(:,1),unique(tfstr.pt.peaks(1,:)));
vy_bsd_peaks=interp1(t_mjd,job_info_s.bsdcont.v_eq(:,2),unique(tfstr.pt.peaks(1,:)));
vz_bsd_peaks=interp1(t_mjd,job_info_s.bsdcont.v_eq(:,3),unique(tfstr.pt.peaks(1,:)));
```

Once the components are given, they are stored in the [3, N] matrix `velpos` and assigned to the `job_info_s` struct

```
velpos=[vx_bsd_peaks;vy_bsd_peaks;vz_bsd_peaks];
```

$\vdots$

```
job_info_s.velpos=velpos;
```

At this point of the code it is checked again which one of the correction method has been given as input. If `patchon=1` the function `hfdf_patch` is called and it returns the peaks corrected (`pout`) after having taken the uncorrected ones (`peaks`) and the velocities needed for the correction (`job_info_s`). In the case of `patchon=0`, the correction has already taken place in the first `switch patchon`, hence the corrected peaks `pout` are simply equal to `peaks`. If `patchon=-1`, `pout` corresponds to the uncorrected peaks.

```
switch patchon
    case 1
        [pout,job_info_s_,checkD]=hfdf_patch(peaks,job_info_s,patch);
    case 0
        pout=peaks; %heterodyne correction
    case -1
        pout=peaks; %no correction
end
```

$\vdots$

It is now possible to compute the Hough map

```
hmap=bsd_hough_compile(4,pout,job_info_s,Tfft);
```

which is plotted if `ploton=1` together with the corrected Peakmaps

```
if ploton==1

    k=find(pout(2,:)>=freq_start & pout(2,:)<= (freq_start+freq_step));
    plot_triplets(pout(1,k),pout(2,k),pout(6,k))

    plot(hmap)

else
end
```

In order to make a comparison between the two Doppler correction and the none, the function `bsd_2_hough` is called thrice The explicit forms of the two corrections are

```
[hmap_hfdf,job_info_s_hfdf,pout_hfdf]=bsd_2_hough(bh,direct,Tfft,sd_lim,1,freq_start,freq_step)
```

```
[hmap_het2,job_info_s_het2,pout_het2]=bsd_2_hough(bh,direct2,Tfft,sd_lim,0,freq_start,freq_step)
```

```
[hmap_none,job_info_s_none,pout_none]=bsd_2_hough(bh,direct,Tfft,sd_lim,0,freq_start,freq_step)
```

The input `sd_lim` can be either given or not because it can be defined after having taken the pulsar spin-down `sd`

```
⋮
T_obs=n_gd(bh)*dx_gd(bh);
df_bin=1/(Tfft*T_obs);

if ~exist('sd_lim','var')

    sd_lim=[sd-51*df_bin sd+10*df_bin]

end
```

Where `T_obs` is the observation time and `df_bin` the spin-down length. The definition of `df_bin` can be recovered from Section 2.1 in which $\delta f = 1/T_{FFT}$ therefore, by having $K_{\dot{f}} = 1$, it is $\delta \dot{f} = \delta f/T_{obs} = 1/T_{obs} \cdot T_{FFT}$. The coefficients of `df_bin` are chosen accordingly to a compromise between the length of the spin-down bin and the time needed for the code to be run.

The two Doppler corrections get fed with the same input, except for `patchon` and `direct`. *hfdf* correction doesn't need any input frequency in order to correct the Peakmap due to its simple shifting technique whereas the *heterodyne* does, hence the pulsar frequency in the database has to be updated respect to the BSD initial time `t0`: `direct2` implies this additional step

```
⋮
cont=cont_gd(bh);
```

```
t0=cont.t0;
direct2=new_posfr(direct,t0);
```
⋮

After that, the corrected Peakmaps and the Hough maps are returned as output.

B.2 CR for several T_{FFT}

In order to find this optimal coherence time, I wrote another function named `comparison_hfdf_bsd` called in a `for` cycle that runs over several T_{FFT} values. As already said in the main text, the *optimal* coherence time is the T_{FFT} that gives the highest CR for the chosen HI.
The function `comparison_hfdf_bsd` has the form of
$[\mathtt{CR\_hfdf}, \mathtt{CR\_het2}, \mathtt{hmap\_hfdf}, \mathtt{hmap\_het2}, \mathtt{freq\_hfdf}, \mathtt{freq\_het2},$
$\mathtt{cand\_hfdf}, \mathtt{cand\_het2}, \mathtt{direct2}, \mathtt{direct\_hough}, \mathtt{sd\_het2}, \mathtt{sd\_hfdf}] =$
$\mathtt{comparison\_hfdf\_bsd}(\mathtt{bh}, \mathtt{pul}, \mathtt{freq\_start}, \mathtt{freq\_step}, \mathtt{kcand}, \mathtt{Tfft}, \mathtt{sd\_lim}).$
Several of the input have already been explained for `bsd_2_hough`; the only two different are

- `pul`: corresponds to `direct` of `bsd_2_hough`;

- `kcand`: is the number of the divisions of the selected frequency interval.

The output are

- `CR_hfdf`, `hmap_hfdf`, `freq_hfdf`, `cand_hfdf`, `sd_hfdf`: as it will be explained later in detail, it is possible to select the strongest candidate (`CR_hfdf`) in each sub-band of `cand_hfdf` defined by `kcand` and to save the corresponding candidate frequency `freq_hfdf` together with its spin-down `sd_hfdf`. These output are repeated for the heterodyne correction with `_het2` instead of `_hfdf`;

- `direct2`: is the pulsar updated at the beginning time of BSD;

- `direct_hough`: is the pulsar updated at the beginning time of the Hough map.

The first lines of this function are the same as the ones written in the previous Section: it is computed the `sd_lim` and the pulsar is updated to the BSD initial time (`direct2`); then `bsd_2_hough` is called twice, once for each of the two Doppler corrections.
The following step is the construction of the [9,N] candidates matrices (`cand_hfdf` and `cand_het2`) thanks to the `bsd_cand_compile`

⋮
```
[cand_hfdf,job_info,checkF]=bsd_cand_compile(hmap_hfdf,job_info_s_hfdf,kcand);
[cand_het2,job_info,checkF]=bsd_cand_compile(hmap_het2,job_info_s_het2,kcand);
```
⋮

The role of `kcand` can be explained with this simple example: if `kcand=10`, then the frequency interval given as input will be divided in 10 sub-bands from which it is selected the strongest candidate - or the strongest two.

The purpose is to recover the SI and store its corresponding CR, therefore it is requested to find the nearest candidate i.e. the one with the minimum distance respect to the frequency and spin-down of the HI. This is done with the pulsar updated to the starting time of the Hough map which is called `direct_hough` be cause the candidates are extracted from it

```
⋮
deltaf_hfdf=1/Tfft;
deltasd_hfdf=deltaf_hfdf/T_obs;
d_hfdf=[];
d_het2=[];
for i=1:length(cand_hfdf(1,:))
    d_hfdf(i)=sqrt(((cand_hfdf(1,i) - direct_hough.f0)/deltaf_hfdf)^2+
((cand_hfdf(4,i) - direct_hough.df0)/deltasd_hfdf)^2);
end
[value_1,col_1]=min(d_hfdf(:));
CR_hfdf=cand_hfdf(6,col_1);
freq_hfdf=cand_hfdf(1,col_1);
sd_hfdf=cand_hfdf(4,col_1);


deltaf_het2=1/Tfft;
deltasd_het2=deltaf_het2/T_obs;

for j=1:length(cand_het2(1,:))
    d_het2(j)=sqrt(((cand_het2(1,j) - direct_hough.f0)/deltaf_het2)^2+
((cand_het2(4,j) - direct_hough.df0)/deltasd_het2)^2);
end
[value_2,col_2]=min(d_het2(:));
CR_het2=cand_het2(6,col_2);
freq_het2=cand_het2(1,col_2);
sd_het2=cand_het2(4,col_2);
```

The differences `d_hfdf` and `d_het2` have the same form of the one defined in Section 2.1.4 and they can be easily displayed in the generic form of

$$d = \sqrt{k_f^2 + k_{\dot{f}}^2} \tag{B.1}$$

where

$$k_f^2 = \left(\frac{f_{cand} - f_{direct}(t_{Hough})}{\delta f} \right)^2$$

$$k_{\dot{f}}^2 = \left(\frac{\dot{f}_{cand} - \dot{f}_{direct}(t_{Hough})}{\delta \dot{f}} \right)^2$$

The results of the previous Section regarded the standard four-bands division, therefore the T_{FFT}s in input were not optimized for the HIs. Hence, the purpose here is to find the value of T_{FFT} which gives the maximum CR, i.e. the higher Signal to Noise ratio (SNR), for the pulsars chosen before.

In order to find the *optimal T_{FFT}* value the `comparison_hfdf_bsd` function needs to be called in a `for` cycle as aforementioned. This is done in the `CRvsTFFT.m` file. First, it is asked which pulsar has to be taken as input in order to acquire its sky coordinates (α, δ), the frequency and the spin-down. After that, the run and the detector are selected. In the current case it is taken the O3 run of the LIGO Hanford detector, i.e. `run=O3LH`. Moreover, the pulsar of the database has to be updated at the detector initial and final observation time, the frequency interval [`f_initial f_final`] and the step `f_step` are set soon after as the number of sub-division, here called `n_cand`.

Several values of what is called `tfft0_optimal` are possible according to which approximation one decides to consider. In the main text there have been explained the different approximations used to define three principal optimal T_{FFT}s. Here more details on the code are given. In the function `CRvsTFFT.m` there are first defined the constants useful for the approximation definitions

```
c=299792458; % light
R0orb=149597870700; % UA
Om0orb=2*pi/(365.256363051*86400); % 1/year
vc=R0orb*Om0orb/c;
R0=5.5e6; % rotational radius at Livingston (lower latitude)
SD=86164.09053083288; %sidereal day
Om0=2*pi/SD;
```

and then the detector plus the contributions of Eqs. 4.4 and 4.6

```
det=ligol;
```

```
A=frequency*R0*Om0*cosd(phi)*cosd(delta)/c;
B=frequency*R0orb*Om0orb/c;
a=A*Om0;
b=B*Om0orb;
```

The specific choice of `det=ligol`, that is the LIGO Livingston detector, corresponds to take the worst latitude between the two LIGOs that is the the most pessimistic situation.

The first possible T_{FFT}^{opt} is the one obtained by considering only the *rotational contribution*, i.e. a in Eq. 4.4.

```
tfft0_optimal_rot=1/sqrt(a);
```

This is equivalent to the T_{FFT} computed for the pulsar frequency in [12] in which it is also found the equivalence between the definition used in the code and the one of Eq. 2.1, i.e.

$$T_{FFT} = T_E \sqrt{\frac{c}{4\pi^2 f R_E}} \approx \frac{1.1 \cdot 10^5}{\sqrt{f}}[s] \tag{B.2}$$

here $\Omega_{rot} = \frac{T_E}{\sqrt{4\pi^2}}$ and $cos\delta = cos\phi = 1$.

The second possibility is the *orbital contribution only*, i.e. b in Eq. 4.6

```
tfft0_optimal_orb=1/sqrt(b);
```

The third and last one includes *both* contributions

```
tfft0_optimal_rotorb=1/(sqrt(a+b));
```

Other 79 values of T_{FFT}s are generated in order to have an adequate understanding of the CR trend

$\vdots$

```
upper_interval=max([tfft0_optimal_rot,tfft0_optimal_rotorb,tfft0_optimal_orb]);
tfft_step=linspace(T_FFT,2*upper_interval,80);
```

$\vdots$

Even if it has been proved that for the HIs chosen $T_{FFT}^{opt,orb} > T_{FFT}^{opt,rot}, T_{FFT}^{opt,rot+orb}$, the interval is computed from T_{FFT}^{std} to the double of the highest amongst the three approximations just in order to be sure to have a sufficient number of points after the resulting maximum T_{FFT} for a generic signal.

Bibliography

[1] B. P. Abbott, R. Abbott, T. D. Abbott, M. R. Abernathy, and et al. Observation of gravitational waves from a binary black hole merger. *Phys. Rev. Lett.*, 116:061102, Feb 2016. doi: `10.1103/PhysRevLett.116.061102`.

[2] B. P. Abbott, R. Abbott, T. D. Abbott, S. Abraham, F. Acernese, K. Ackley, C. Adams, R. X. Adhikari, and et al. All-sky search for continuous gravitational waves from isolated neutron stars using Advanced LIGO O2 data. *Phys. Rev. D*, 100:024004, Jul 2019. doi: `10.1103/PhysRevD.100.024004`.

[3] B. P. Abbott, R. Abbott, T. D. Abbott, S. Abraham, F. Acernese, K. Ackley, and et al. GWTC-1: A gravitational-wave transient catalog of compact binary mergers observed by LIGO and Virgo during the first and second observing runs. *Phys. Rev. X*, 9:031040, Sep 2019. doi: `10.1103/PhysRevX.9.031040`.

[4] B. P. Abbott, R. Abbott, T. D. Abbott, F. Acernese, K. Ackley, C. Adams, T. Adams, P. Addesso, R. X. Adhikari, and et al. Gravitational Waves and Gamma-Rays from a Binary Neutron Star Merger: GW170817 and GRB 170817A. ApJ, 848(2):L13, Oct. 2017. doi: `10.3847/2041-8213/aa920c`.

[5] R. Abbott, T. D. Abbott, S. Abraham, F. Acernese, K. Ackley, A. Adams, and et al. Gravitational-wave Constraints on the Equatorial Ellipticity of Millisecond Pulsars. ApJ, 902(1):L21, Oct. 2020. doi: `10.3847/2041-8213/abb655`.

[6] T. Akgün, A. Reisenegger, A. Mastrano, and P. Marchant. Stability of magnetic fields in non-barotropic stars: an analytic treatment. *Monthly Notices of the Royal Astronomical Society*, 433(3):2445–2466, 06 2013. doi: `10.1093/mnras/stt913`.

[7] N. Andersson and K. D. Kokkotas. The R-Mode Instability in Rotating Neutron Stars. *International Journal of Modern Physics D*, 10(4):381–441, Jan. 2001. doi: `10.1142/S0218271801001062`.

[8] F. Antonucci, P. Astone, S. D'Antonio, S. Frasca, and C. Palomba. Detection of periodic gravitational wave sources by Hough transform in the f versus $\dot{f}$ plane. *Classical and Quantum Gravity*, 25(18):184015, Sept. 2008. doi: `10.1088/0264-9381/25/18/184015`.

[9] P. Astone, M. Bassan, P. Bonifazi, P. Carelli, E. Coccia, C. Cosmelli, S. D'Antonio, V. Fafone, S. Frasca, Y. Minenkov, I. Modena, G. Modestino, A. Moleti, G. V. Pallottino, M. A. Papa, G. Pizzella, L. Quintieri, F. Ronga,

R. Terenzi, and M. Visco. Search for periodic gravitational wave sources with the Explorer detector. Phys. Rev. D, 65(2):022001, Dec. 2001. doi: 10.1103/PhysRevD.65.022001.

[10] P. Astone, A. Colla, S. D'Antonio, S. Frasca, and C. Palomba. Method for all-sky searches of continuous gravitational wave signals using the Frequency-Hough transform. Phys. Rev. D, 90(4):042002, Aug. 2014. doi: 10.1103/PhysRevD.90.042002.

[11] P. Astone and et al. Advanced Virgo computing at CNAF. *CNAF annual report*, 2019. https://www.cnaf.infn.it/wp-content/uploads/2020/05/cnaf-annual-report-2019.pdf.

[12] P. Astone, S. Frasca, and C. Palomba. The short fft database and the peak map for the hierarchical search of periodic sources. *Classical and Quantum Gravity*, 2260, 09 2005. doi: 10.1088/0264-9381/22/18/S34.

[13] M. Bailes, B. K. Berger, P. R. Brady, M. Branchesi, K. Danzmann, and et al. Gravitational-wave physics and astronomy in the 2020s and 2030s. *Nature Reviews Physics*, 3(5):344–366, Apr. 2021. doi: 10.1038/s42254-021-00303-8.

[14] A. Buonanno and B. S. Sathyaprakash. *Sources of Gravitational Waves: Theory and Observations*, page 287–346. Cambridge University Press, 2015. doi:10.1017/CBO9781139583961.009.

[15] C. Cutler and É. E. Flanagan. Gravitational waves from merging compact binaries: How accurately can one extract the binary's parameters from the inspiral waveform? Phys. Rev. D, 49(6):2658–2697, Mar. 1994. doi: 10.1103/PhysRevD.49.2658.

[16] V. Ferrari, L. Gualtieri, and P. Pani. *General Relativity and its Applications: Black Holes, Compact Stars and Gravitational Waves*. CRC Press, 1 edition, 2020. doi:10.1201/9780429491405.

[17] K. Glampedakis and L. Gualtieri. Gravitational Waves from Single Neutron Stars: An Advanced Detector Era Survey. In L. Rezzolla, P. Pizzochero, D. I. Jones, N. Rea, and I. Vidaña, editors, *Astrophysics and Space Science Library*, volume 457 of *Astrophysics and Space Science Library*, page 673, Jan. 2018. doi: 10.1007/978-3-319-97616-7_12.

[18] N. instruments. *Understanding FFTs and Windowing*.

[19] K. Jani, J. Healy, J. A. Clark, L. London, P. Laguna, and D. Shoemaker. Georgia tech catalog of gravitational waveforms. *Classical and Quantum Gravity*, 33(20):204001, Oct. 2016. doi: 10.1088/0264-9381/33/20/204001.

[20] K. D. Kokkotas. Gravitational Wave Astronomy. *Reviews in Modern Astronomy*, 20:140, Oct. 2008. doi: 10.1002/9783527622993.ch7.

[21] B. Krishnan, A. M. Sintes, M. A. Papa, B. F. Schutz, S. Frasca, and C. Palomba. Hough transform search for continuous gravitational waves. Phys. Rev. D, 70(8):082001, Oct. 2004. doi: 10.1103/PhysRevD.70.082001.

[22] I. La Rosa, P. Astone, S. D'Antonio, S. Frasca, P. Leaci, A. L. Miller, C. Palomba, O. J. Piccinni, L. Pierini, and T. Regimbau. Continuous Gravitational-Wave Data Analysis with General Purpose Computing on Graphic Processing Units. *Universe*, 7(7):218, June 2021. doi: `10.3390/universe7070218`.

[23] P. D. Lasky. Gravitational Waves from Neutron Stars: A Review. PASA, 32:e034, Sept. 2015. doi: `10.1017/pasa.2015.35`.

[24] P. Leaci, P. Astone, S. D'Antonio, S. Frasca, C. Palomba, O. Piccinni, and S. Mastrogiovanni. Novel directed search strategy to detect continuous gravitational waves from neutron stars in low- and high-eccentricity binary systems. Phys. Rev. D, 95(12):122001, June 2017. doi:`10.1103/PhysRevD.95.122001`.

[25] LIGO Scientific Collaboration and Virgo Collaboration. All-sky search for periodic gravitational waves in the O1 LIGO data. Phys. Rev. D, 96(6):062002, Sept. 2017. doi:`10.1103/PhysRevD.96.062002`.

[26] LIGO Scientific Collaboration and Virgo Collaboration. All-sky search for continuous gravitational waves from isolated neutron stars using Advanced LIGO O2 data. Phys. Rev. D, 100(2):024004, July 2019. doi:`10.1103/PhysRevD.100.024004`.

[27] Ligo Scientific Collaboration, VIRGO Collaboration, and Kagra Collaboration. All-sky search for continuous gravitational waves from isolated neutron stars in the early O3 LIGO data. Phys. Rev. D, 104(8):082004, Oct. 2021. doi:`10.1103/PhysRevD.104.082004`.

[28] L. Lindblom. Neutron star pulsations and instabilities. *arXiv preprint astro-ph/0101136*, 2001. arxiv:`astro-ph/0101136`.

[29] O. J. Piccinni. An enhanced sensitivity procedure for continuous gravitational-wave detection. *Nuovo Cimento C Geophysics Space Physics C*, 40(3):125, May 2017. doi: `10.1393/ncc/i2017-17125-3`.

[30] O. J. Piccinni, P. Astone, S. D'Antonio, S. Frasca, G. Intini, P. Leaci, S. Mastrogiovanni, A. Miller, C. Palomba, and A. Singhal. A new data analysis framework for the search of continuous gravitational wave signals. *Classical and Quantum Gravity*, 36(1):015008, Jan. 2019. doi: `10.1088/1361-6382/aaefb5`.

[31] K. Riles. Recent searches for continuous gravitational waves. *Modern Physics Letters A*, 32(39):1730035–685, Dec. 2017. doi: `10.1142/S021773231730035X`.

[32] H. Saio. R-mode oscillations in uniformly rotating stars. ApJ, 256:717–735, May 1982. doi: `10.1086/159945`.

[33] N. Sarin and P. D. Lasky. The evolution of binary neutron star post-merger remnants: a review. *General Relativity and Gravitation*, 53(6):59, June 2021. doi: `10.1007/s10714-021-02831-1`.

[34] M. Sieniawska and M. Bejger. Continuous Gravitational Waves from Neutron Stars: Current Status and Prospects. *Universe*, 5(11):217, Oct. 2019. doi: `10.3390/universe5110217`.

[35] The LIGO Scientific Collaboration, the Virgo Collaboration, and the KAGRA Collaboration. Searches for continuous gravitational waves from young supernova remnants in the early third observing run of Advanced LIGO and Virgo. *arXiv e-prints*, page arXiv:2105.11641, May 2021. `https://ui.adsabs.harvard.edu/abs/2021arXiv210511641T`.

[36] K. S. Thorne. Multipole expansions of gravitational radiation. *Rev. Mod. Phys.*, 52:299–339, Apr 1980. doi: `10.1103/RevModPhys.52.299`.

[37] G. Wang and W.-B. Han. Observing gravitational wave polarizations with the LISA-TAIJI network. Phys. Rev. D, 103(6):064021, Mar. 2021. doi: `10.1103/PhysRevD.103.064021`.

[38] J. M. Weisberg and J. H. Taylor. The Relativistic Binary Pulsar B1913+16: Thirty Years of Observations and Analysis. In F. A. Rasio and I. H. Stairs, editors, *Binary Radio Pulsars*, volume 328 of *Astronomical Society of the Pacific Conference Series*, page 25, July 2005. `https://ui.adsabs.harvard.edu/abs/2005ASPC..328...25W`.

[39] C. M. Will. *Theory and Experiment in Gravitational Physics*. Cambridge University Press, 2 edition, 2018. doi:`10.1017/9781316338612`.